AD NUMBER
AD851948
LIMITATION CHANGES
TO: **Approved for public release; distribution is unlimited.**
FROM: **Distribution authorized to U.S. Gov't. agencies and their contractors; Specific Authority; MAY 1968. Other requests shall be referred to Air Force Armament Lab., Eglin AFB, FL.**
AUTHORITY
AFATL ltr 2 Oct 1972

AFATL-TR-68-61

Theoretical Terminal Ballistic Investigation and Studies of Impact at Low and Very High Velocities

R. T. Sedgwick
Space Sciences Laboratory
General Electric Company

TECHNICAL REPORT AFATL-TR-68-61

MAY 1968

AIR FORCE ARMAMENT LABORATORY
AIR FORCE SYSTEMS COMMAND • UNITED STATES AIR FORCE
EGLIN AIR FORCE BASE, FLORIDA

THEORETICAL TERMINAL BALLISTIC INVESTIGATION AND STUDIES OF IMPACT AT LOW AND VERY HIGH VELOCITIES

R. T. Sedgwick

FOREWORD

This report was prepared by Dr. R. T. Sedgwick of the Space Sciences Laboratory of the General Electric Missile and Space Division, King of Prussia, Pennsylvania, under Air Force Contract F08635-67-C-0079, "Theoretical Terminal Ballistic Investigation and Studies of Impact at Low and Very High Velocities", and covers the period March 1, 1967 to February 29, 1968. The work was administered under the direction of the Air Force Armament Laboratory located at Eglin Air Force Base, with Dr. N. E. Chatterton, Mr. G. C. Crews, Mr. L. L. Wilson (ATBT) as Project Engineers. Experimental data for problem III (steel into steel) as reported in Appendix IV were produced at the Terminal Ballistics Facility of the Ballistic Division.

The author wishes to acknowledge the contributions of Mr. E. J. Halda for the continual improvement of the numerical techniques involved.

Information in this report is embargoed under the Department of State International Traffic in Arms Regulations. This report may be released to foreign governments by departments or agencies of the U. S. Government subject to approval of the Air Force Armament Laboratory (ATBT), Eglin AFB, Florida 32542, or higher authority within the Department of the Air Force. Private individuals or firms require a Department of State export license.

This technical report has been reviewed and is approved.

for Joseph E. Duval, Colonel, USAF
Chief, Ballistics Division

ABSTRACT

The important parameters and failure modes pertinent to ballistic impact are discussed in detail and a review of available theoretical penetration formulas is presented. A method for a complete solution to the ballistic impact problem is outlined including the material model, numerical techniques, application of failure criteria and description of both post-failure material behavior as well as the residual state. Parametric studies based on this outline should reveal the necessary insight for developing predicitive relationships between the pre-impact and post-impact parameters.

A complete solution is presented for the case of a steel cylinder impacting normally into a thin plate of like material. It is shown that predictions of stress wave propagation and reflections in the early stages of impact are in good agreement with one-dimensional theory. The shear stress, generalized plastic strain and plastic work distributions as well as the material flow pattern indicate that failure will be due to plugging, hence the employment of a maximum shear theory of failure. The final shape of both the projectile and the plate plug are given and the velocity of the plate material beneath the projectile at the predicted time of failure is in good agreement with the value of 0.382 km/sec predicted by the theory of Recht and Ipson. This gives a residual kinetic energy for the projectile plate-plug configuration of 3.1×10^9 ergs or 47.4% of the total initial energy. It is believed that much of the remaining energy is retained in the projectile and plate-plug as internal energy. It is predicted that both the projectile and plate-plug will remain intact but a region of contained failure in the projectile near the impacted surface is defined.

A second problem in which an aluminum plate was substituted was also solved. Again the mode of failure was plugging and the predicted residual state, including the plate plug configuration and residual velocity, was in good agreement with experimental results.

TABLE OF CONTENTS

TABLE OF CONTENTS (Concluded)

LIST OF FIGURES

LIST OF FIGURES (Continued)

LIST OF FIGURES (Continued)

LIST OF FIGURES (Concluded)

SECTION I

INTRODUCTION

The ultimate solution to be derived from impact studies, whether experimental or theoretical in nature, should provide a set of simple mathematical formulas which relate the influencing pre-impact parameters, both geometrical and material, with those of the post-impact state. The derived relationships must be in reasonable agreement with available experimental data as well as provide reliable predictions in the ranges of parameters for which experimental data are not available. To meet this latter requirement a thorough understanding of the material flow occurring throughout the impact process as well as the associated material failure phenomena are necessitated. Hence, mathematical solutions which describe the material behavior from the time of initial impact to the time at which residual effects can be predicted are desirable. A study based on such solutions should provide the pre-requisite insight necessary for the development of the required set of predictive relationships.

The availability of large scale computer programs such as CRAM (Continuous Response of Anelastic Material), which has been developed at the General Electric Space Sciences Laboratory, provides a feasible means for such a study of the impact process.

In this report parameters affecting penetration mechanics in the ballistic range of velocities are discussed and pertinent penetration formulas are reviewed. The details of the numerical solution techniques to be employed including the material models used are next outlined in detail. Since the total solution involves the use of failure criteria, various of these are discussed in general along with the special modes of failure pertinent to projectile-impacted plates and the resulting residual effects.

Finally, solutions are obtained for two specific impact cases. These solutions include the numerical results as well as the prediction of plate failure and residual effects.

The work on the high velocity portion of this contract was concluded at the end of the first six months and the results from that part of the study are included in the interim report of the same title dated August 1967 [1].

SECTION II

IMPORTANT PENETRATION PARAMETERS

The physical parameters which influence the flow and fracture of material subjected to impact loading in the ballistic range of velocities can be classified as either configurational or material. Configurational parameters include initial impact speed, obliquity and yaw as well as geometrical quantities defining the initial projectile and target shapes and the type of interaction, as in the case of direct versus edge impact. The residual configurational parameters of interest are those which describe the mass and velocity distribution of the primary fragments. In addition certain parameters may be of interest which describe the final configuration of the damaged target such as hole diameter or extent of petalling cracks, etc.

Material parameters are those which describe the state properties as well as the flow and fracture characteristics of the projectile and target material. These include equation of state constants, shear modulus, yield strength or Brinell hardness number, and strain rate and work hardening coefficients as well as any parameters associated with failure criteria.

Many of the important impact parameters are well defined and have a physical basis while others are either poorly defined or are simply constants appearing in an empirically fitted experimental curve. Still other parameters or combinations of parameters are yet to be defined through extensive theoretical and experimental parametric investigations. A thorough understanding of the parameters and how they affect material flow and fracture is a necessary pre-requisite to the development of any penetration theory relating pre- and post-impact parameters.

In this study emphasis is placed on material parameters; however, the importance of the configurational parameters is recognized because of their influence on stress states and hence the dynamic material behavior.

Figures 1 through 4 are included to provide some insight into the effects of varying certain important configurational and material parameters.

Figures 1 and 2 due to Recht and Ipson [2] show the typical residual versus impact velocity curves for thin plate plugging by normally and obliquely impacting projectiles respectively. In addition, the effect of varying the ratio of plate thickness to projectile length, T/L is indicated.

Figure 3, due to K. H. Abbott [3], shows the variation of normalized penetration depth versus impact velocity for the case of steel and aluminum alloys impacting 1/2 in. steel armor plates of hardness 30 RC. The curves demonstrate the effect of projectile hardness on penetration.

Figure 4, due to Curtis [4] shows plots of ballistic limit velocity versus target Brinell hardness numbers for a standard 57 MM APC M86 projectile impacting a 1-1/2 in. thick RH armor plate. The curves indicate a shift in optimum hardness toward a higher BHN as impact obliquity increases.

Figures 1 through 4 indicate certain qualitative relationships which exist between a few of the important impact parameters such as residual velocity, ratio of plate thickness to projectile length, impact obliquity, penetration depth, yield strength or Brinell hardness number and ballistic limit velocity. Insight into relationships such as these are necessary for the development of meaningful penetration formulas.

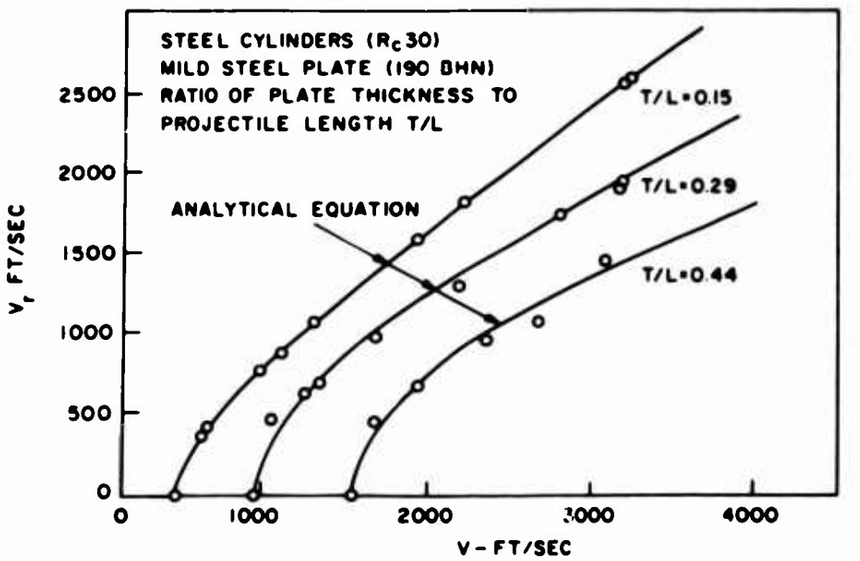

Figure 1. Residual Velocity Versus Impact Velocity Curve for Various Ratios of Plate Thickness to Projectile Length. These Curves for Normal Impact are due to Recht & Ipson [2]

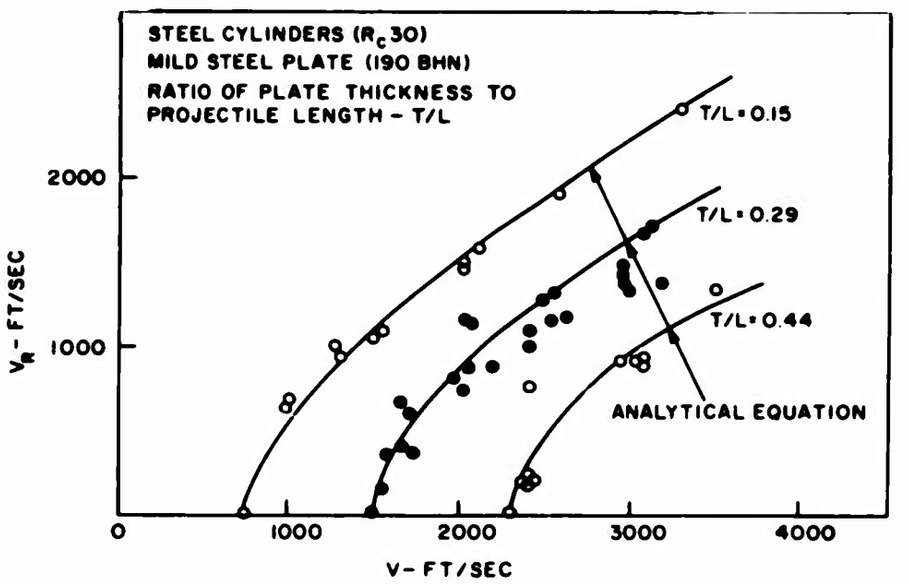

Figure 2. Residual Velocity Versus Impact Velocity Curve for Various Ratios of Plate Thickness to Projectile Length. These Curves for Oblique Impact (45^{o}) are due to Recht and Ipson [2]

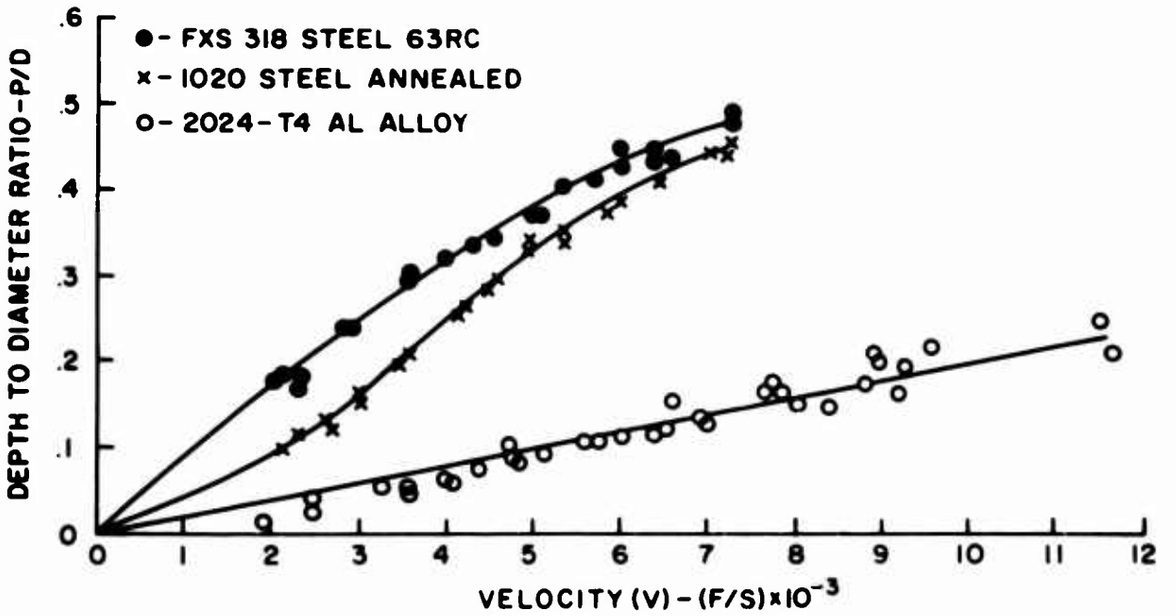

Figure 3. Normalized Penetration Depth Versus Impact Velocity for Steel and Aluminum Alloy Cylinders Impacting Steel Armor. These Curves are due to Abbott [3]

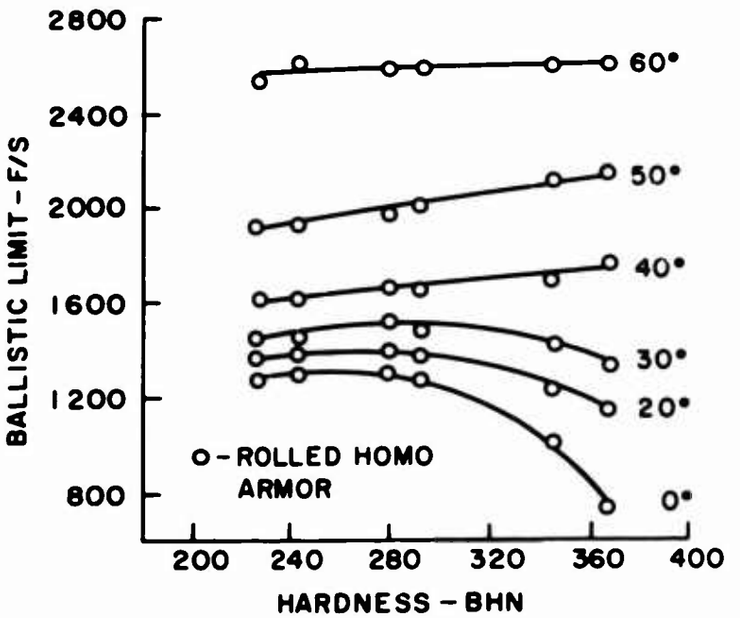

Figure 4. Ballistic Limit Velocity Versus Target Brinell Hardness Number for Various Impact Obliquities for the Case of a 57 MM APC M86 Projectile Impacting into 1 1/2 in. Thick RH Armor Plate. The Curves are due to Curtis [4]

SECTION III

FAILURE MODES

Although material behavior is quite complex when subjected to the extreme conditions of impact, several definite failure modes can be delineated which depend on various configurational and geometric parameters. The knowledge of this dependence is necessary in the formulation of specific failure criteria and in their later generalization for predicative purposes. Fugelso and Bloedow [5] have listed various types of failure modes which are observed and calculated critical velocities for which each type of failure would occur provided conditions are such that that type of failure is favored. The various failure modes will be discussed qualitatively here in order to provide a better understanding of how the various parameters involved influence the mode of failure.

3.1 Fracture Due to Initial Stress Wave

The initial stress wave which propagates through the plate after impact is compressive in nature. If the compressive dynamic yield strength is significantly less than the peak compressive stress, failure is likely to occur if the region subjected to the high stresses is not contained during the passage of the wave. For the case of projectile-plate impact this situation could occur in the vicinity of the free surface of the plate and initiate fracture. An increase in target density, hardness or compressive yield strength, or compressive ultimate strength would decrease the tendency toward this type of failure. A cross sectional schematic diagram of this type of fracture is shown in Figure 5(a).

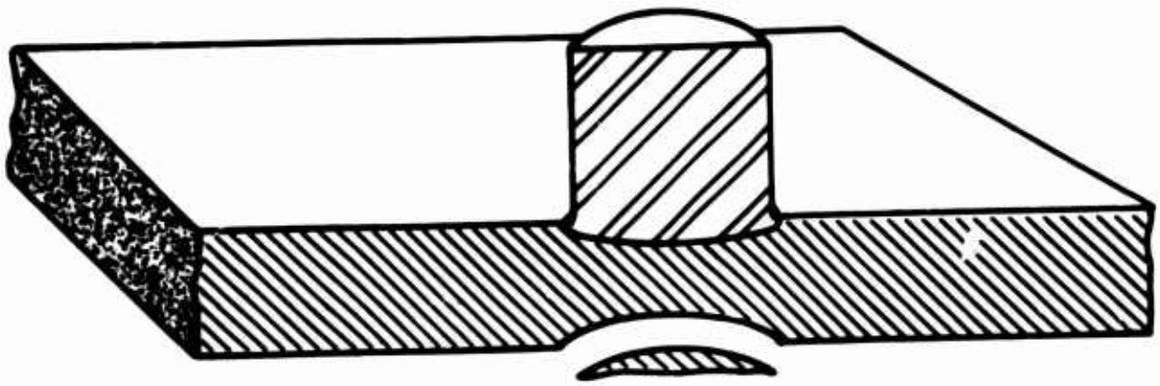

a. FRACTURE DUE TO INITIAL STRESS WAVE

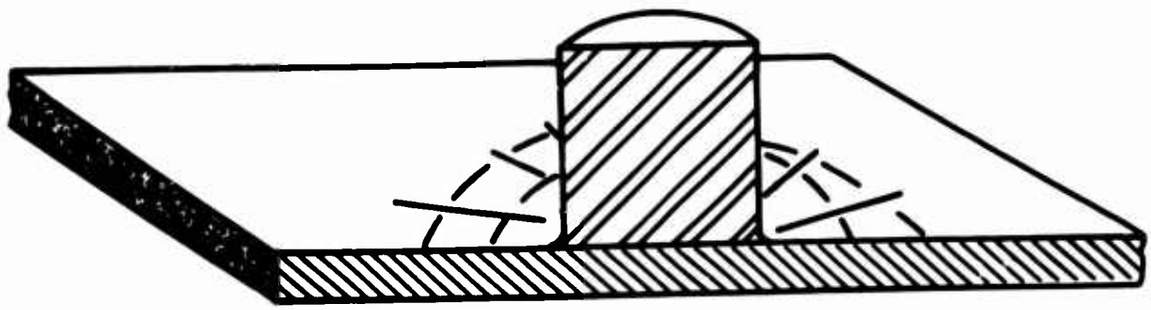

b. RADIAL FRACTURE BEHIND INITIAL WAVE FRONT IN A PLATE OF BRITTLE MATERIAL.

Figure 5. Cross-sectional Schematic Diagrams of Plate Failure Associated with the Initial Stress Wave

3.2 Radial Fracture Behind Initial Wave Front

Although the normal stress behind the initial stress wave front remains compressive until interaction with rarefaction waves, the radial stress built up is tensile in nature. If the target material behaves in a brittle manner and the tensile stresses built up are greater than the ultimate dynamic tensile strength, radial and/or circumferential cracks are likely to occur. This type of failure is shown in Figure 5(b).

3.3 Spallation

When the initial compressive stress wave reflects from the rear free surface of the plate a tensile wave develops in the region of normal incidence. If this reflected wave builds up to a tensile stress in the vicinity of the dynamic ultimate stress in tension for the material, spall fracture will occur. The parameters governing spallation are the plate thickness to projectile diameter ratio and the dynamic ultimate tensile strength of the plate material. For the case of rolled, homogeneous targets, imperfections such as inclusions flattened by the rolling process might reduce the tensile strength of the material in the transverse direction below its theoretical value and increase the tendency toward spall failure. Figure 6 is a cross-sectional schematic diagram of this type of failure.

3.4 Petalling

Petalling failure occurs when the stress condition is such that radial cracks form from the center outward and the plate material curls back to allow the projectile to proceed through. This type of failure is due to the large circumferential and radial stresses which develop

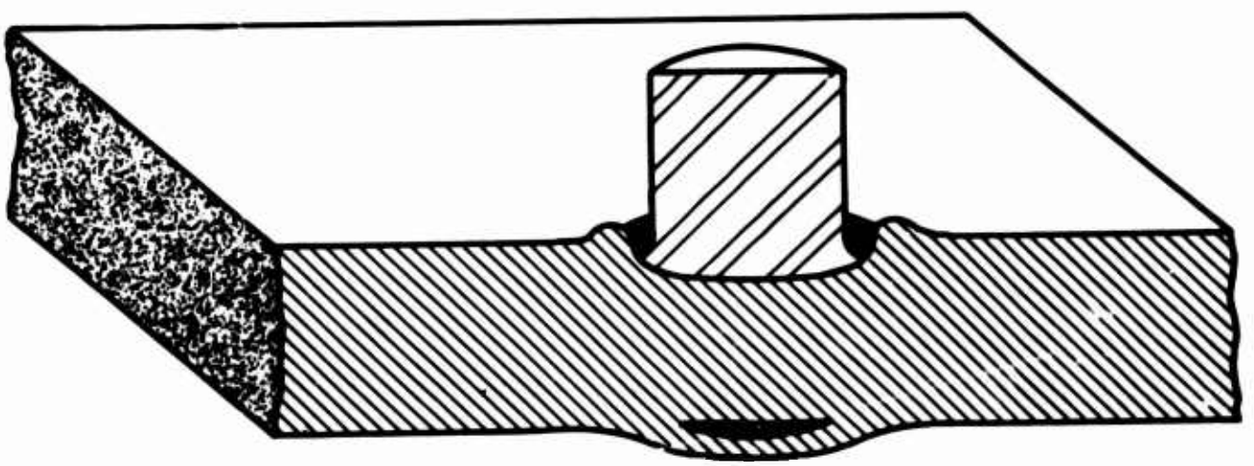

Figure 6. Cross-Sectional Schematic Diagram of Spallation Failure

behind the initial shock wave. The stress pattern is caused by either extensive radial plastic flow or by significant plate bending. For this reason plates of a relatively ductile material subjected to impact by hard conical or ogive projectiles are likely to exhibit this type of failure. Also, thin plates which bend significantly exhibit petalling due to the large bending stresses imposed near the free surface of the plate. The tendency toward this type of failure is enhanced at velocities very near the ballistic limit since at these relatively low velocities the momentum transfer is not restricted merely to the region beneath the deforming projectile.

Cross-sectional schematic diagrams for both front and rear petalling failure are shown in Figure 7.

3.5 Plugging

Plugging is defined as that type of failure which occurs when the projectile pushes a plate plug, approximately equal in radius to that of the deformed projectile, through the rear surface of the plate.

The tendency for plugging failure increases with plate hardness as measured by the yield strength or the Brinell hardness number. The reason for this is that the harder the plate, the more difficult it becomes for the plate material to be pushed radially outward. Hence a narrow shear zone builds up ahead of the projectile in the vicinity of its periphery and the dominant plastic flow is confined to this region. Other parameters influencing the conditions favoring plugging type failure are relative plate thickness and projectile nose shape. Thinner plates have a greater tendency to plug and will even allow softer plates to fail this way provided the velocity is not sufficiently close to the

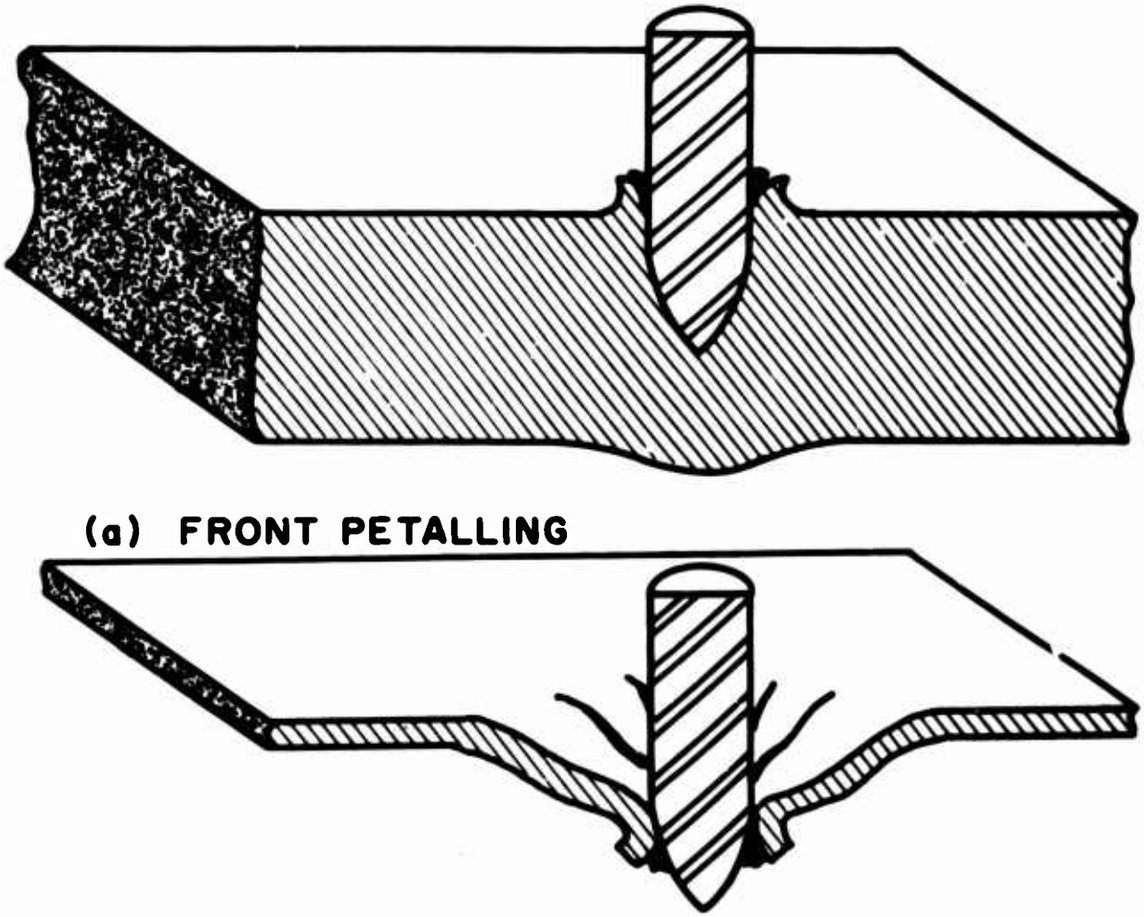

Figure 7. Cross-sectional Views of Plates Showing Both Front and Rear Petalling

ballistic limit so that radial momentum transfer causes severe plate bending. Similarly, the blunter the projectile, the more the tendency is toward plugging failure. This can be seen by noting that a cylindrical projectile would establish a much higher shear stress gradient at its well defined periphery than would a conical or ogive shaped projectile. This is not to say that plugging would not occur under the latter conditions because it has been observed for thin, relatively hard plates. For thicker, more ductile plates, however, the pointed projectile nose shape, provided it does not shatter or deform severely, helps to provide a radial component to the material flow.

The process of plug formation is clearly due to a shearing failure of the plate material. The shearing process is made more feasible, however, by an accompanying rise in temperature which lowers the material resistance to shear.

The shape of the plug depends on the orientation of the maximum shear planes. If pure shear at the projectile periphery is apparent, then the plug will be cylindrical. Small amounts of plate bending or the influence of supports, however, can cause tensile or compressive stress to be superimposed in the region of maximum shear. Thus, cases exist for which truncated cone, inverted truncated cone, barrel, inverted barrel as well as cylindrically shaped plugs have been observed.

Figure 8 is a cross-sectional schematic diagram showing typical plugging-type failure.

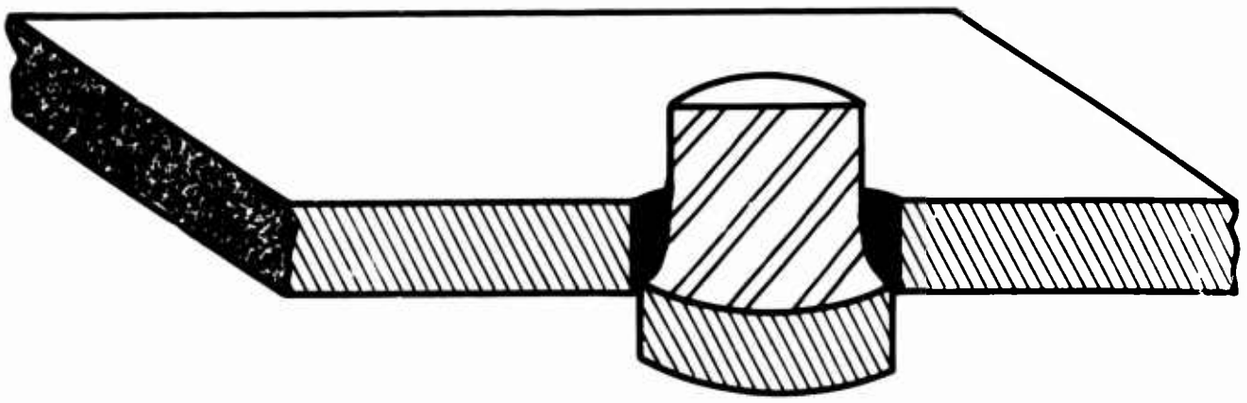

Figure 8. Cross-sectional Schematic Diagram Indicating Plugging-type Failure

SECTION IV

REVIEW OF PENETRATION FORMULAS

Numerous studies in the ballistic range of impact velocity have resulted in the formulation of various plate penetration theories. Due to the complexity of the material behavior, these theories have either been empirical in nature, thus lacking in physical insight as well as predictive capabilities, or over-idealized theoretical approximations. Both types of formulations admittedly have been restricted. to definite ranges of parameters and to the description of definite failure modes but have served the useful purpose of defining important parameters or groups of parameters as well as their relationship to each other and their influences on material behavior. In addition, these theories provide a basis for further refinements as additional insight into impact phenomena, provided by either numeridal studies or through innovations in experimental techniques, is gained. It is with this in mind that the following penetration theories are discussed in general together with the extent of their idealization. More detail is given to those theories which are pertinent to the current study, i.e. ballistic impact into targets of finite thickness.

Several review articles concerned with the problem of impact and penetration in the ballistic range of velocity are available. These include the work of Goldsmith [6] and Cristescu [7]. In addition several studies of significance appear in the literature. Bakhsiyan [8] studied the case of a rigid cylinder of infinite mass penetrating a viscoplastic plate. He assumed that only frictional shearing stresses were acting between the cylinder and plate material so that the displacement field in the plate beneath the actual impact zones was not determined. Pytel and Davids [9] studied the problem of cylindrical impact into a

plate by assuming a circular velocity distribution on the plate surface. Like Bakhsiyan [8] they assumed only frictional shearing stress to be acting but were able to consider plate displacements beneath the impact zone. Only the case of linear viscosity was assumed. The method of characteristics was employed by Kochetkov [10] to solve the simplified model of Bakhsiyan with the extension of the plate material model to provide a description of perfectly-plastic and linear strain hardening materials. Chou [11] retained the visco-plastic model but removed the assumption of infinite projectile mass. His analysis emphasized the determination of hole size after complete perforation. Both strains and strain-rate distributions were determined for the case of aluminum plates. Minich and Davids [12] studied velocity loading of a plate using a viscous fluid model. A threshold strain level below which the plate material was assumed to behave in an elastic or rigid manner was introduced and the analysis was concerned mainly with the case of trapped plugs. Kukudjanov [13] considered the added problem of projectile rotation about its axis, the projectile being considered a rigid cylinder. Taylor [14] and Bethe [15] based their theories on the assumption that the energy necessary for plate perforation is equal to the work done in expanding a hole in the plate from that of a very small diameter to the final hole size. Thomson [16] developed an energy model for the penetration of thin plates of rigid, perfectly plastic material. He considered the energy due to plastic deformation and interface heating but attributed most of the energy dissipation to the former. Both conical and ogival projectiles were considered and the assumptions that neither plugging nor spallation occurs and that projectile velocity remains constant during impact were made.

Although most of the theoretical studies of penetration were made feasible by assuming rigid projectiles, some studies were conducted

specifically for determining projectile deformation. Zener and Peterson [17] studied the effects of frictional, plastic, inertial and transverse forces on the projectile during impact. Masket [18] and Bluhm [19] also studied projectile deformation, the latter summarizing experimental studies of stress in the projectile during impact.

Finally, the theories most pertinent to the current study will be considered in detail. These are the theory of Recht and Ipson [20], in which a blunt cylinder pushes a plug through a thin plate, and the theories of Thomson [16] and Zaid and Paul [21] in which conical or ogival projectiles cause petalling failure.

4.1 The Theory of Recht and Ipson

Although Recht and Ipson [20] also consider plug formation of thick plates as well as the case of oblique impact, only the simpler case of normal penetration of thin plates by blunt cylinders will be considered here. The assumption is made that a plug will be formed in the plate and pushed out by the projectile as shown in Figure 9. Reduction in projectile velocity is attributed to the momentum transfer to the plate which accelerates the plate-plug mass as well as to the shear resistance at the plug periphery which acts to decelerate the combined projectile-plug combination. Recht and Ipson express this mathematically by first writing the conservation of momentum equation for a completely inelastic impact of a blunt projectile with a free plate plug

$$V_f = \frac{M_p}{M_p + M_{sn}} V \qquad (1)$$

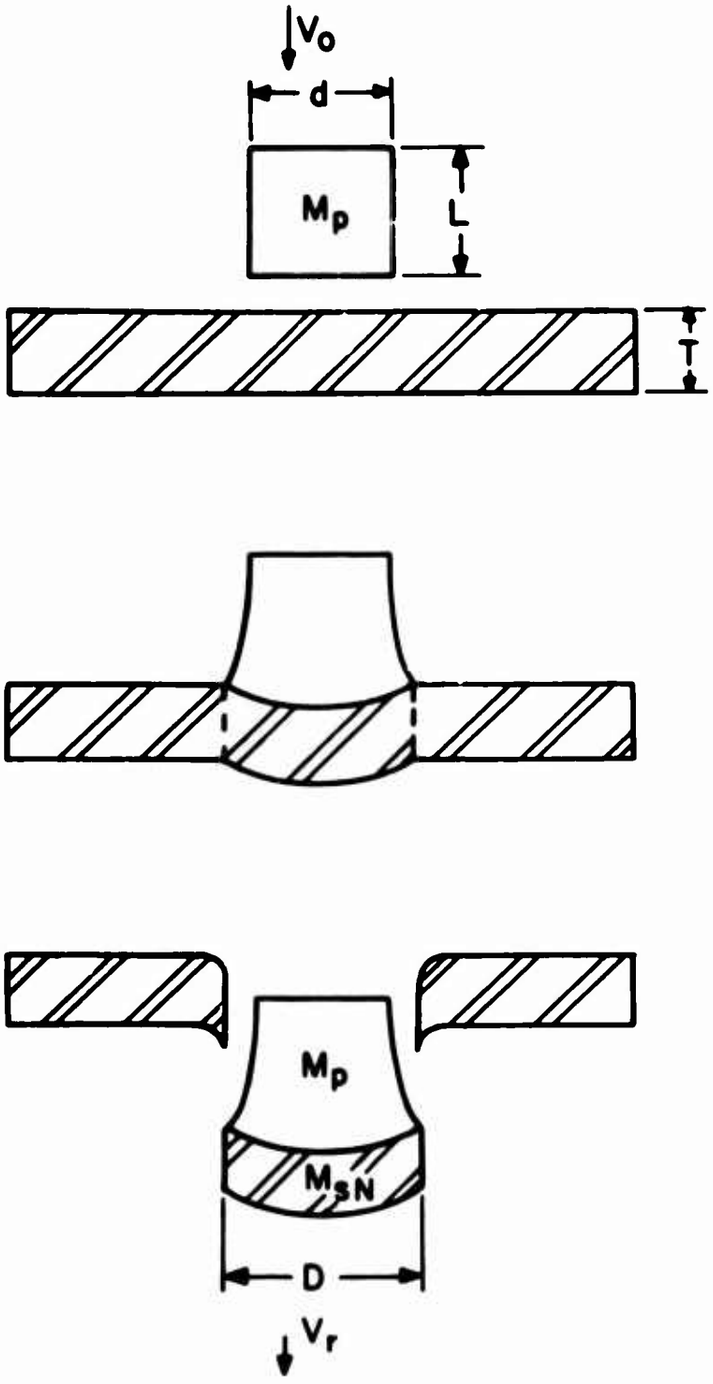

Figure 9. Diagram of Plugging Failure Used in the Theory of Recht and Ipson

and expressing the energy converted to internal energy for this case as the difference between initial and final kinetic energy

$$E_{fn} = \left[\frac{M_{sn}}{M_p + M_{sn}}\right] \frac{1}{2} M_p V^2 \tag{2}$$

where the subscripts p and s refer to the projectile and plug respectively, n stands for normal impact and f refers to the free-projectile-plug impact where the retarding shearing forces are neglected. Hence an energy balance can be written for a projectile plate impact as

$$\frac{1}{2} M_p V^2 = E_{fn} + W_n + \frac{1}{2} M_p V_r^2 + \frac{1}{2} M_{sn} V_r^2 \tag{3}$$

where W_n is the additional kinetic energy converted to internal energy by virtue of the presence of the peripherial shear zone and V_r is the residual velocity of the plate-plug combination. By incorporating a minimum perforation velocity, V_{xn}, for which $V_r = 0$, Recht and Ipson obtain the expression

$$W_{xn} = \left[\frac{M_p}{M_p + M_{sn}}\right] \frac{1}{2} M_p V_{xn}^2 \tag{4}$$

where W_{xn} is the value of W_n at $V = V_{xn}$. Next the assumption that the average dynamic shear stress remains constant allows the substitution of the expression for W_{xn} of Equation (4) in place of W_n in Equation (3). Then by using the expression for E_{fn} of Equation (2), the energy balance can be written as

$$V_r = \left[\frac{M_p}{M_p + M_{sn}}\right] \left(V^2 - V_{xn}^2\right)^{1/2} \tag{5}$$

Recht and Ipson then rewrite Equation (5) in terms of geometry as

$$V_r = \left[\frac{1}{1 + \Omega\left(\frac{D}{d}\right)^2 \frac{T}{L}}\right] \left(V^2 - V_{xn}^2\right)^{1/2} \qquad (6)$$

where Ω is the ratio of plate to projectile density, D/d is the ratio of plug diameter to projectile diameter and T/L is the ratio of plate thickness to projectile length.

Although much of the theory of Recht and Ipson is omitted here because of its inapplicability to this study, Equation (6) is representative of the type of end results desired from an impact study as well as an indication of the current state of the art represented by the various impact theories previously mentioned. For example, Equation (6) is simple and is in agreement with experimental evidence for the case of single plate impact and plugging-type failure. In addition it relates pre-impact parameters with those of the post-impact state. The shortcomings, which should not be emphasized since they represent a compromise between the assumptions and the degree of complexity, lie in the implicit nature of the parameters inherently involved in the minimum perforation velocity. It should be mentioned, however, that a partially successful analytical expression for V_{xn} has been developed [20] and forms the basis for a possible modified version having wider ranges of application. In addition, an assumption must be made as to the value of the plug diameter, D, which somewhat prejudices the calculated residual effects. With the use of an experimentally obtained minimum perforation velocity, the theory of Recht and Ipson [20] is extremely useful in its current state and can be improved only by the incorporation of more explicit material parameters, possibly through insight gained from more complete numerical studies.

4.2 Thompson's Model

Thompson [16] calculated the work due to plastic deformation and inertial effects in expanding a hole in a thin plate to a size necessary for complete penetration by conical or ogival projectiles.

He assumed a rigid projectile and a rigid, perfectly plastic plate. In addition he assumed that the radial and axial stresses were insignificant compared to the circumferential stresses. Finally, it was assumed that plastic deformation takes place without a change of volume.

Figure 10(a) shows the deformed plate configuration used by Thompson for the general case. The work required per unit volume for deformation from s to b is given as

$$Y \quad d\epsilon_o = Y \int_s^b \frac{dS}{s} = Y \ell n \frac{b}{s} \tag{7}$$

so that the work done on the differential ring element is

$$d W_p = 2 \pi h_o S \, dS \, \ell n \left(\frac{b}{s}\right) \tag{8}$$

The expression for total work then becomes

$$W_p = 2 \pi h_o Y \int_o^b s \ell n \frac{b}{s} \, dS = \frac{1}{2} \pi b^2 h_o Y \tag{9}$$

Next the dynamical work is written as

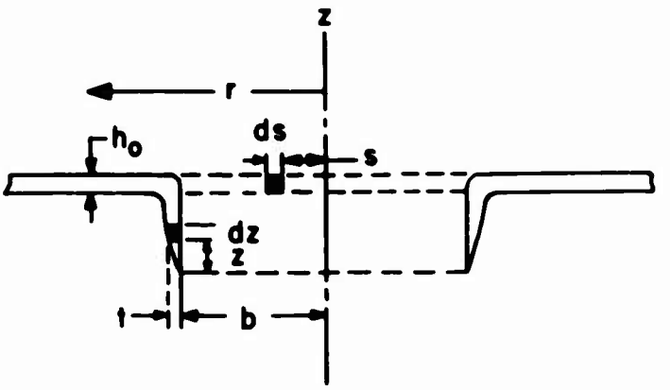

(a) FAILED CONFIGURATION OF PLATE USED IN THOMPSON'S MODEL.

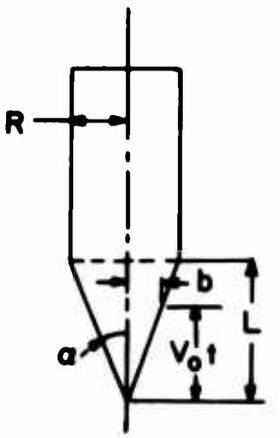

(b) CONICAL HEAD PROJECTILE

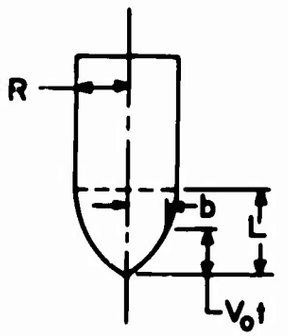

(c) OGIVAL HEAD PROJECTILE

Figure 10. Failed Plate Configuration and Projectiles Used in Thompson's Model of Failure [16]

$$W_d = \int M \frac{d^2 b}{dt^2} \, db + \frac{dM}{dt} \frac{db}{dt} \, db \qquad (10)$$

where

$$M = \pi \rho h_o b^2$$

and

$$\frac{dM}{dt} = 2 \pi \rho h_o b \frac{db}{dt}$$

Hence Equation (10) becomes

$$W_d = \pi \rho h_o \int_o^{t_o} b^2 \frac{d^2 b}{dt^2} \, db + 2 \pi \rho h_o \int_o^{t_o} b \left(\frac{db}{dt}\right)^2 db \qquad (11)$$

For the conical head projectile of Figure 10(b)

$$b = \frac{RVt}{L}$$

and

$$\frac{db}{dt} = \frac{RV}{L}$$

so the total work done during the penetration process by a conical head projectile becomes

$$W = \pi R^2 h_o \left[\frac{1}{2} Y + \rho \left(\frac{VR}{L}\right)^2\right] \qquad (12)$$

Figure 10(c) shows an ogival head projectile which can be described by

$$b = R \sin \frac{\pi}{2} \left(\frac{Vt}{L}\right)$$

$$\frac{db}{dt} = \frac{\pi}{2} \left(\frac{RV}{L}\right) \cos \frac{\pi}{2} \left(\frac{Vt}{L}\right) \tag{13}$$

and

$$\frac{d^2b}{dt^2} = -R \left(\frac{\pi V}{2L}\right)^2 \sin \frac{\pi Vt}{2L}$$

By substituting these expressions into Equation (11) and integrating from zero to L/R and finally adding the result to the plastic work, the expression for the total work required for penetration by an ogival head projectile can be written as

$$W = \pi R^2 h_o \left[\frac{1}{2} Y + 1.86 \rho \left(\frac{VR}{L}\right)^2 \right] \tag{14}$$

From the expressions for total work expended the residual velocities can easily be calculated as

$$V_r = \left[V_o^2 - \frac{2W}{M_p} \right]^{1/2} \tag{15}$$

4.3 The Theory of Zaid and Paul

Zaid and Paul [21] consider the case of thin target petalling due to impact of a rigid ogive or conical tipped projectile. Conservation of momentum is applied to the projectile-plate zone of action as shown in Figure 11(a). The zone of action is defined by a radius sufficiently large to include a portion of the plate that is unaffected by the perforation process. Conservation of axial momentum is written as

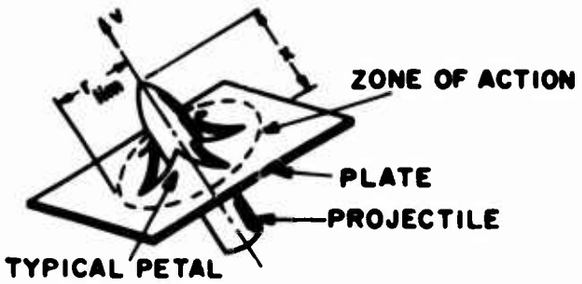

(a) PETALLING FAILURE OF A THIN PLATE.

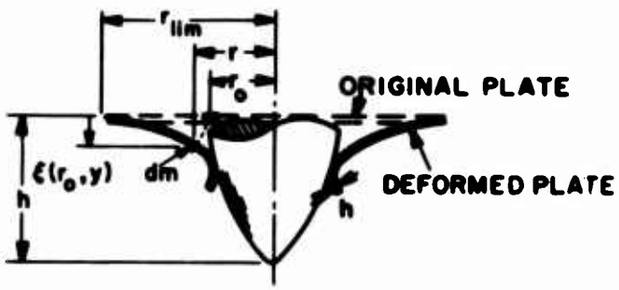

(b) GENERAL CONFIGURATION USED IN THE THEORY OF ZAID AND PAUL

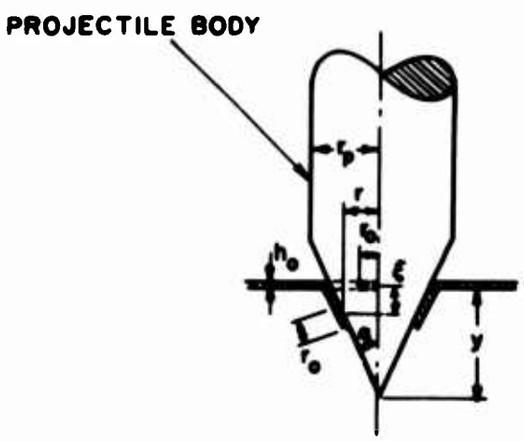

(c) PETALLING FAILURE OF A THIN PLATE IMPACTED BY A PROJECTILE HAVING A CONICAL NOSE.

Figure 11. Petalling Failure Diagrams. These Diagrams are due to Zaid and Paul [21]

$$M_p V_o = M_p V + M_t(y) \tag{16}$$

where M_p is the projectile mass, V is the instantaneous projectile velocity and $M_t(y)$ is the axial component of plate momentum. The momentum of the increment of mass dm of Figure 11(b) can be written as

$$dM_t = 2\pi \rho h_o r_o \dot{\xi}\, dr \quad . \tag{17}$$

The velocity can be expressed in terms of the independent variable y as

$$\dot{\xi} = \frac{\partial \xi}{\partial y} \frac{dy}{dt} = V \frac{\partial \xi}{\partial y} \tag{18}$$

and Equation (17) when integrated gives

$$M_t = 2\pi \rho h_o \int_{r_{o\,min}}^{r_{lim}} V r_o \frac{\partial \xi (r_o, y)}{\partial y} dr_o . \tag{19}$$

The effective target mass is then defined by Zaid and Paul as the momentum M_t divided by the instantaneous velocity

$$M(y) = \frac{M_t}{V} = 2\pi \rho h_o \int_{r_{o\,min}}^{r_{lim}} r_o \frac{\partial \xi (r_o, y)}{\partial y} dr_o . \tag{20}$$

Hence by combining Equations (16) and (19) the equation for change in velocity is obtained:

$$\Delta V = V_o - V = \frac{M(x)}{M_p} V \tag{21}$$

Zaid and Paul [21] apply the theory to the case of the conical tipped projectile shown in Figure 11(c). It is seen that ξ can be expressed as

$$\xi = \left(x \tan \alpha - r_o\right) \cos \alpha \tag{22}$$

so that Equation (20) becomes

$$M(x) = 2 \pi \rho h_o \left[\int_o^{y \tan \alpha} r_o \, dr_o\right] \tan \alpha \cos \alpha$$

or

$$M(x) = \pi \rho h_o (y \tan \alpha)^2 \sin \alpha \tag{23}$$

Hence Equation (21) becomes

$$\Delta V = \frac{\pi \rho h_o (y \tan \alpha)^2 V \sin \alpha}{M_p} \tag{24}$$

If it is then assumed as is done by Zaid and Paul that the total drop in velocity is attained when the projectile body intersects the target plane, i.e. when $y \tan \alpha$ becomes equal to r_p, the projectile body radius

$$\Delta V_{TOTAL} \approx \frac{\pi \rho h_o r_p^2}{M_p} V_o \sin \alpha \tag{25}$$

where the instantaneous velocity is approximated by the initial impact velocity.

One can not extend the conical case solved by Zaid and Paul directly to the case of cylindrical impact by assuming $\alpha = 90^{o}$ because the flow is kinematically specified. However, for very large cone angles (α approaching 90^{o}) the upper limit on the total velocity drop is

$$\left(\Delta V_{TOTAL}\right)_{U.L.} \approx \frac{\pi \rho h_o r_p^2}{M_p} V_o \qquad (26)$$

and the actual value is probably quite close to that value since $\sin \alpha \approx 1$. Equation (26) could then be expressed as

$$\left(\Delta V_{TOTAL}\right)_{U.L.} \approx \left(\frac{\rho_T}{\rho_P}\right)\left(\frac{h_o}{L}\right) V_o \qquad (27)$$

It should be noted, however, that strength effects do not appear in this formulation and for a given velocity this omission would cause a greater error for large values of α. For the case of a cylinder impacting a plate which fails by petalling, it might be possible to incorporate strength effects implicitly through use of a reduced velocity in Equation (27). The value to be used would be the velocity at which petalling failure begins assuming a reduction in velocity caused by kinetic energy lost in initial bending of the plate. Another possibility, however, is to develop the theory for cylindrical impacts along lines parallel to the theory of Zaid and Paul assuming a different form for the kinematic flow constraints. This is done in the following Section.

4.4 Petalling Failure Caused by Cylindrical Impact

Petalling type failure usually occurs when the plate material is pushed axially and radially outward as in the case of thick plates or impact by conical or ogive projectiles. For thin plates subjected to impact by a blunt cylinder, petalling failure can occur provided the material does not behave in a brittle manner and significant plate bending occurs to provide the necessary stress pattern. These conditions are met in thin ductile plates when the impact velocity is very near the ballistic limit. The model used in this section assumes that a rigid projectile impacting into a thin aluminum plate causes the necessary amount of bending to initiate petalling failure. Figure 12 indicates the stages of this type of penetration. The projectile velocity is decreased from its initial impact velocity V_o, to the value V_1 shown in Figure 12(b) at which time the plate has bent sufficiently for radial fracture to occur. This velocity will be used as the initial velocity in a modified Zaid and Paul theory.

In order to apply the theory a feasible kinematic flow pattern for petalling must be assumed. One such possibility is shown in Figure 13. It is assumed that

$$\sin\theta = \frac{1}{r_p} y \tag{28}$$

so that

$$\dot{\theta}\cos\theta = \frac{1}{r_p} V . \tag{29}$$

Hence the expression for ξ is

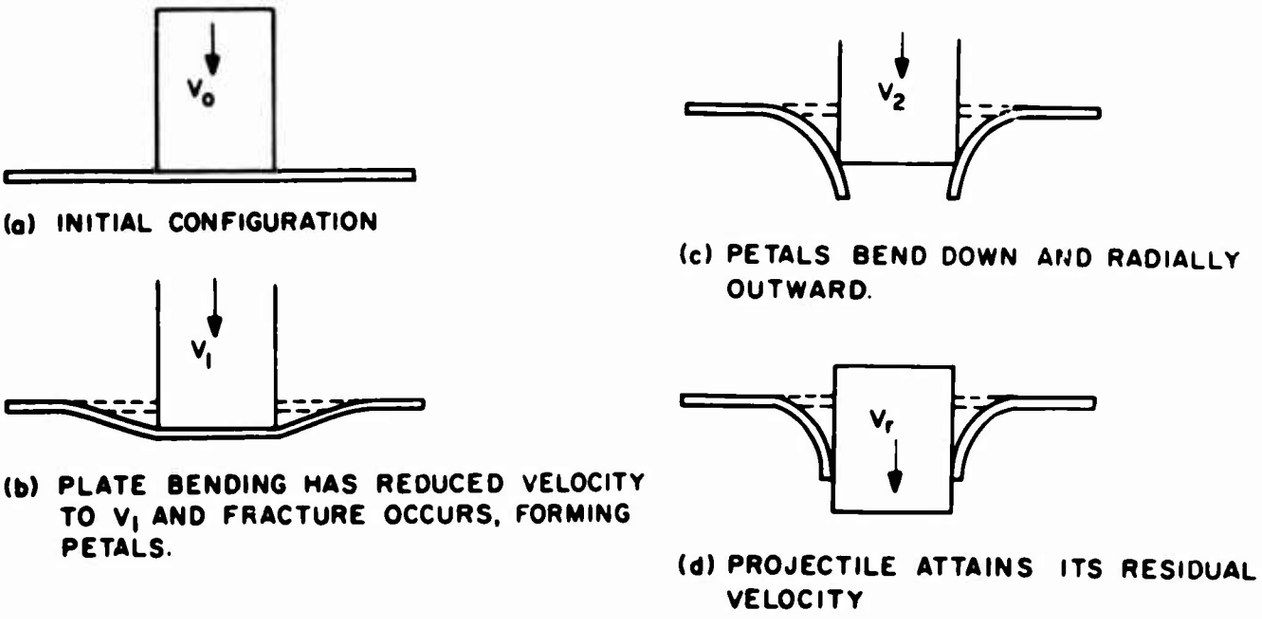

Figure 12. Stages of Petalling Failure due to Cylindrical Impact. Velocity Must be Near the Ballistic Limit Velocity for this Type of Failure

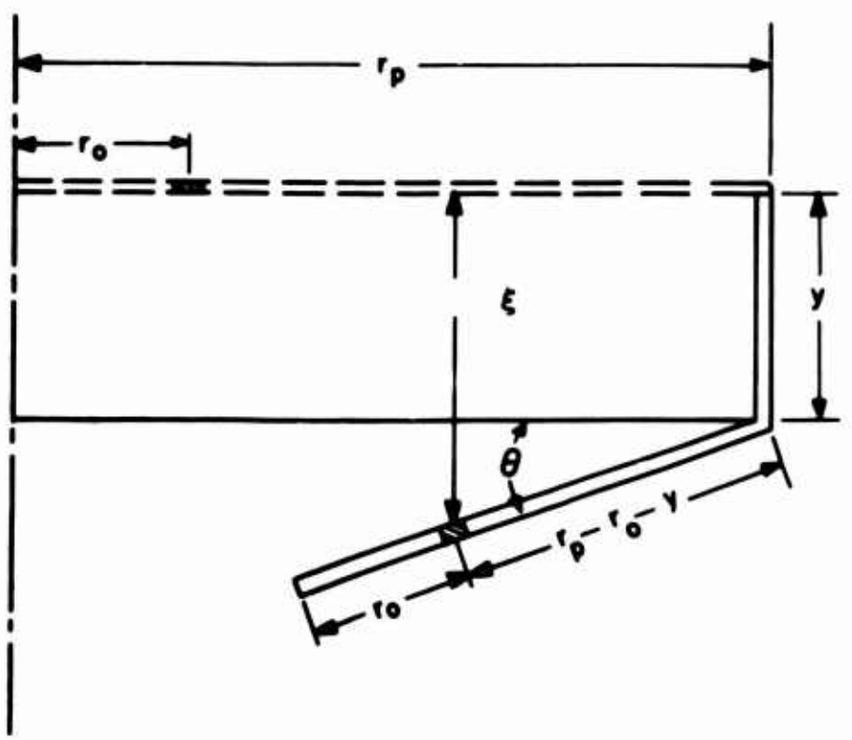

Figure 13. Diagram Indicating an Assumed Kinematic Flow Pattern for Petalling Failure due to Cylindrical Impact at Velocities near the Ballistic Limit

$$\xi = y + \left(r_p - r_o - y\right) \sin\theta$$

or

$$\xi = 2y - \frac{r_o}{r_p} y - \frac{1}{r_p} y^2 \tag{30}$$

and

$$\frac{\partial \xi}{\partial y} = 2 - \frac{2}{r_p} y - \frac{r_o}{r_p} \tag{31}$$

Substituting this expression into Equation (20) and integrating over the interval $r_o = 0$ to $r_o = r_p - y$ gives

$$M(y) = 2\pi\rho h_o \left[\left(1 - \frac{y}{r_p}\right)\left(r_p - y\right)^2 - \frac{1}{3r_p}\left(r_p - y\right)^3 \right] \tag{32}$$

and from Equation (21)

$$\Delta V = \frac{2\pi\rho h_o V}{M_p} \left[\left(1 - \frac{y}{r_p}\right)\left(r_p - y\right)^2 - \frac{1}{3r_p}\left(r_p - y\right)^3 \right] \tag{33}$$

To get the total velocity change the value of y = o is used in the above expressions which amounts to calculating the equivalent momentum change for the reverse process. The value obtained is

$$\Delta V_1 = \left(\frac{4}{3}\right)\left(\frac{\rho_T}{\rho_P}\right)\left(\frac{h_o}{L}\right) V_1 \tag{34}$$

This velocity change is of the same order of magnitude as that obtained by taking the limit of the cone as its half angle approaches $\pi/2$. This however, is not the total velocity change since it was assumed that plate bending sufficient for petalling has occurred previous to the applications of the modified Zaid and Paul theory. Hence the total velocity change is given as

$$\Delta V_{TOTAL} = \Delta V_o + \Delta V_1 \tag{35}$$

where $\Delta V_o = V_o - V_1$, and is the initial loss in projectile velocity up to the point of fracture. The value to be used for V_1 must be obtained from either an approximate solution of a plate impulse loading problem or from the interface velocity calculated numerically as in CRAM at the time of predicted fracture. It should be noted that this theory applies only for thin ductile plates at velocities near the ballistic limit.

SECTION V

NUMERICAL SOLUTION OF IMPACT PROBLEMS

As was mentioned earlier, numerical studies of the impact process form an important and necessary link in the development of simple, meaningful penetration formulas which relate pre- and post-impact parameters. In addition numerical solutions provide detailed answers to questions relating either to parameters which are implicitly handled by the penetration formulas or to specific impact cases for which satisfactory penetration formulas are non-existent.

It is important then to understand the numerical model completely, including the constitutive relations used as well as the numerical techniques employed.

5.1 Mathematical Models

The mathematical model used in the numerical solution of the ballistic impact problem involves the necessary equations for expressing the dynamic material behavior. Of these equations, the equation of state, which, in general, relates pressure to internal energy and volume change and the constitutive relation involving the deviatoric stresses and strains are of utmost importance.

The equations governing the ballistic impact process are given in Appendix I. These include the equations of motion, continuity and energy conservation together with expressions for the strain rates and artificial viscosity. To complete the mathematical model, a constitutive relation including an equation of state must be chosen. The equation of state to be used here is of the form

$$p = \left(a_o + a_1\mu + a_2\mu^2 + a_3\mu^3\right)\left(1 - a_4\mu\right) + \left(b_o + b_1\mu + b_2\mu^2 + b_3\mu^3\right) E \qquad (36)$$

where p is pressure, μ is the reciprical of relative volume minus one or current density divided by initial density minus one, the a_i and b_i, $i = 0, 1, 2, 3$ are constants for a given material, and E is total internal energy per unit volume. Figure 14 is a one-dimensional schematic showing the typical behavior of one form of Equation (36). It is assumed that the material is able to withstand very high hydrostatic compressive stresses but that it will fail in hydrostatic tension at a value of stress equal to 1/3 of the dynamic yield stress unless values for minimum allowable pressure are known for specific materials.

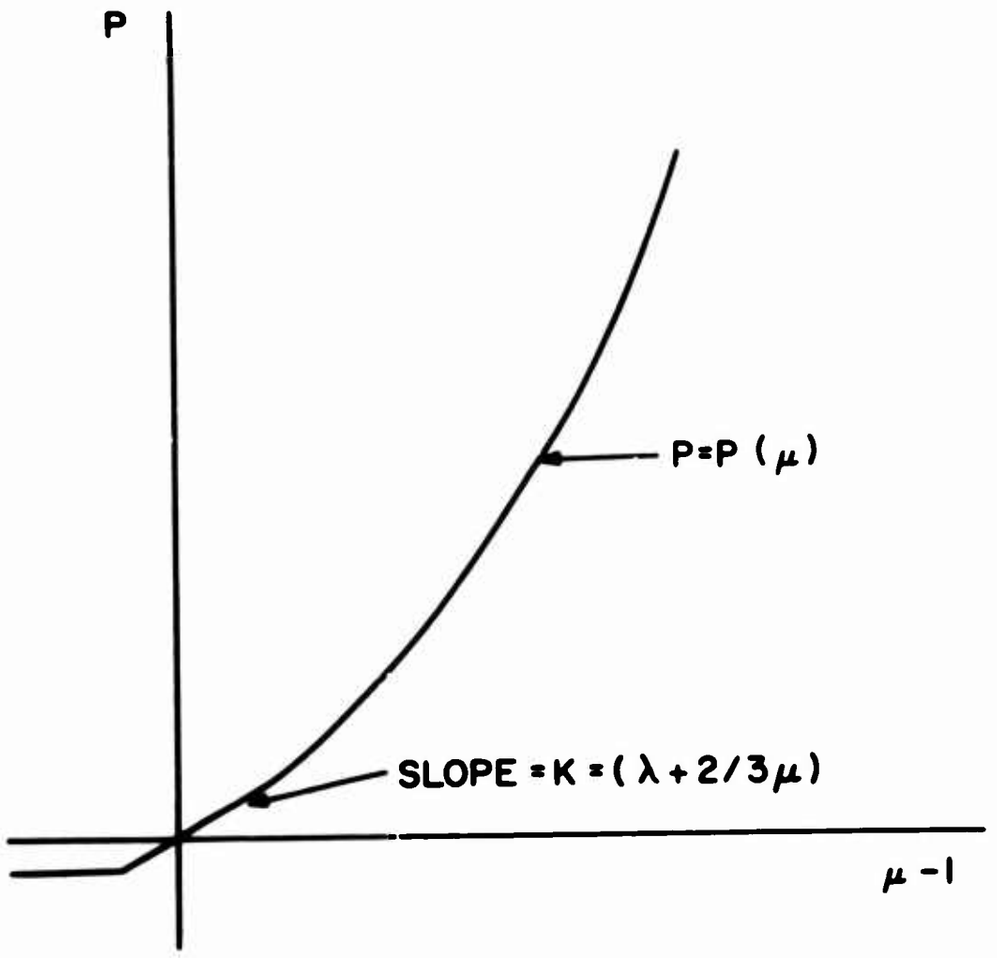

Figure 14. Schematic Representation of Hugoniot Equation of State

The strength dependent portion of the constitutive relation is given in terms of the deviatoric stresses and strains. The equations for this description are:

$$\begin{aligned}
\dot{s}_{xx} &= 2\mu\left(\dot{\epsilon}_{xx} - \frac{1}{3}\,\dot{V}/V\right) \\
\dot{s}_{yy} &= 2\mu\left(\dot{\epsilon}_{yy} - \frac{1}{3}\,\dot{V}/V\right) \\
\dot{s}_{\theta\theta} &= 2\mu\left(\dot{\epsilon}_{\theta\theta} - \frac{1}{3}\,\dot{V}/V\right) \\
\dot{T}_{xy} &= \mu\left(\dot{\epsilon}_{xy}\right)
\end{aligned} \tag{37}$$

where the terms on the left of the equations represent time rates of change of the deviatoric stress tensor, μ is the shear modulus and the terms in parentheses represent the time rates of change of deviatoric strain, i.e. total components minus the symmetric terms. Equations (37) represent elastic behavior. To complete the model, a yield criterion must be chosen. It will be assumed that the material is elastic-perfectly plastic and that the Von Mises yield criterion is applicable. This can be expressed as

$$\left(s_1^2 + s_2^2 + s_3^2\right) - \frac{2}{3}\,Y_0^2 \leq 0 \tag{38}$$

where Y_0 is the yield strength of the material and the s_i, $i = 1, 2, 3$, are the principal stress deviators. To handle the problem of the non-uniqueness of stress which arises in plasticity due to the fact that material unloads elastically, the stresses are first calculated using the elasticity equations, tested against the yield condition and finally the components are adjusted normally to the yield surface, if necessary.

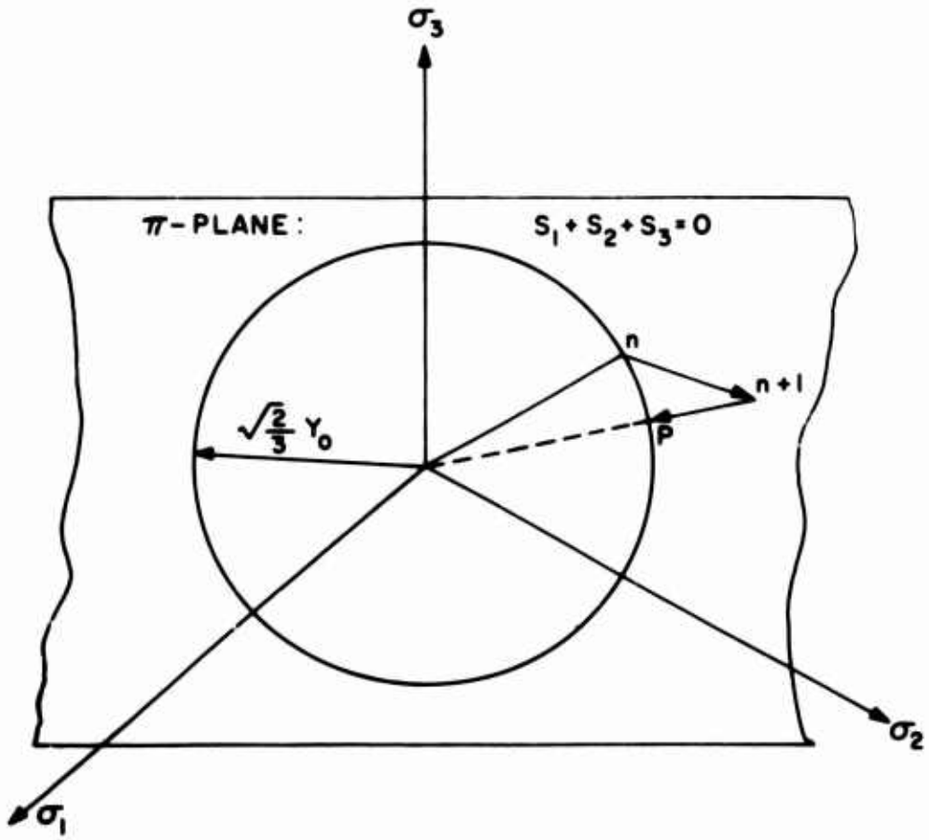

Figure 15. Projection of Von Mises Yield Surface on the π-Plane

This procedure is demonstrated in Figure 15. The orthogonal principal stress axes are shown. The π-Plane is situated perpendicular to a line which makes equal angles with the axes. This line is also the axis of a right circular cylinder in stress space, i.e. the yield surface, and its projection on the π-Plane is shown in Figure 15. When the material is loaded elasticly the loading path lies within the circle. If, however, the stress components calculated from Equations (37) violate the yield condition, they must be adjusted normally to the yield surface. This is shown in Figure 15 where the material was loaded from n to n + 1. Since the stress state at n + 1 is not possible for this model, each component must be adjusted so that the state of stress is at point P on the yield surface. This is accomplished by multiplying each stress component by the fraction

$$\frac{\sqrt{\frac{2}{3}}\, Y_0}{\sqrt{2\ J}} \tag{39}$$

where

$$2J = \left[s_1^2 + s_2^2 + s_3^2 \right] = s_{xx}^2 + s_{yy}^2 + s_{\theta\theta}^2 + 2\, T_{xy}^2 \tag{40}$$

and J is the second invariant of the stress deviators.

The total stresses, which are used in the equation of motion are given by the equations

$$\begin{aligned} \Sigma_{xx} &= s_{xx} - [p + q] \\ \Sigma_{yy} &= s_{yy} - [p + q] \\ \Sigma_{\theta\theta} &= s_{\theta\theta} - [p + q] \\ T_{xy} &= T_{xy} \end{aligned} \tag{41}$$

where p is the pressure given by the equation of state and q is the artificial viscosity term (see Appendix I). The artificial viscosity is necessary only for stabilization of the numerical techniques employed in the solution of these equations. It has the effect of spreading out the shock front to avoid discontinuities in the stresses.

Figure 16 is a one-dimensional schematic which indicates the material behavior when the total stresses are considered. When the material is loaded, path O A B C of Figure 16 is followed. Line A B C is parallel to the hydrostatic curve and is separated from it by a value

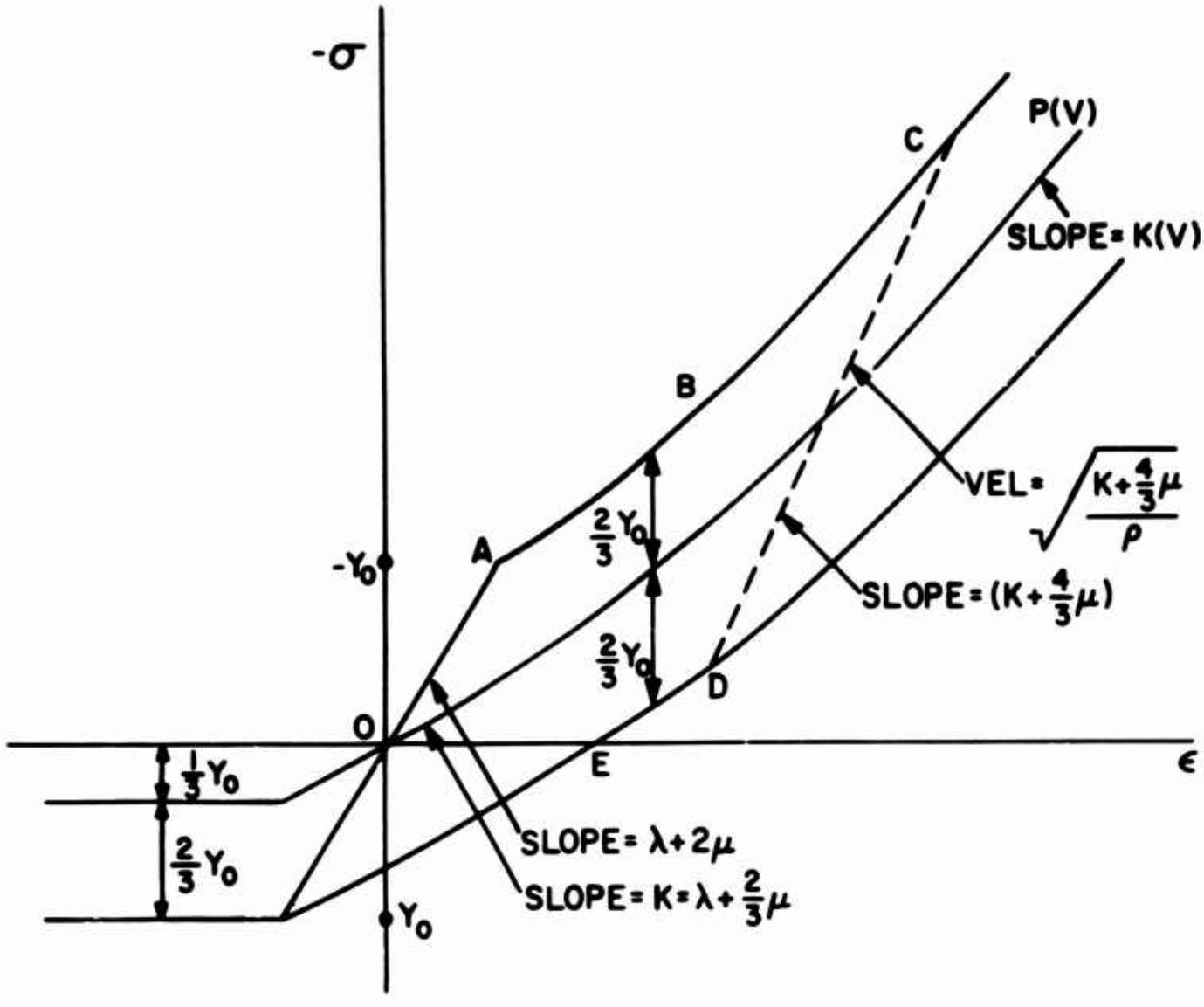

Figure 16. One-dimensional Schematic Showing the Loading and Unloading Paths for an Elastic-Plastic Hydrodynamic Material

of 2/3 Y_o. When the stresses are released, the path C D E is followed. It can be seen from Figure 16 that the amplitude of an elastic release wave can be much greater than the yield strength of the material. This is because its amplitude depends on the relative slopes of line C D and the hydrostat. Since the slope of C D is $K + \frac{4}{3}\mu$ and the slope of the hydrostat is K, the relative slope, and hence the elastic release amplitude, depends on the shear modulus of the material. The velocity of the elastic release wave is given by

$$c_E = \sqrt{\left(K + \frac{4}{3}\mu\right)/\rho} \qquad (42)$$

so it is seen that an increase in the shear modulus has the effect of reducing the amplitude of the release wave while increasing its velocity. Since wave velocities are dependent upon the slopes of the stress-strain paths, it can be seen from Figure 16 that an elastic release wave will overtake the loading wave as long as the slope of the hydrostat at the stress level to which the material was loaded is less than the slope of the elastic unloading path. This process attenuates the shock amplitude.

In order to effectively apply the mathematical model described above to the solution of impact problems, it must be incorporated into the numerical framework of a computer program. The numerical techniques and procedures used here are discussed in the following section.

5.2 Numerical Techniques

A wide variety of numerical codes which can be applied to the solution of impact problems have been developed at the General Electric Space Sciences Laboratory. These include PICWICK III (Eulerian [22]). VISTA (Particle-in-cell [23]) and CRAM (Lagrangian). In addition, a structure code, DEPROSS [24, 25] is available. The choice of numerical

code to be used in any particular solution of a problem depends on the range of values of the parameters of interest as well as restrictions imposed by the desired results. In the present ballistic velocity impact study the Lagrangian code, CRAM, will be employed, since it is best suited for including realistic strength effects, defining boundaries and handling more than one material.

5.3. CRAM Description

CRAM, an acronym for Continuous Response of Anelastic Materials, is a two-dimensional Lagrangian code which was developed at the General Electric Space Sciences Laboratory for studying the response of materials to dynamic loading in both the hydrodynamic and elastic-plastic regimes. The code is similar to HEMP developed by M. Wilkins [26] at Lawrence Radiation Laboratory and is designed to be run on the IBM 7094 computer. The basic equations for the Lagrangian description are given in Appendix I. The finite difference equations employed in CRAM are in Appendix II.

In the application of CRAM to any specific problem, several factors must be considered. These include the generation of the Lagrangian mesh, the proper choice of constitutive relations and material constants, and loading conditions. For the case of axisymmetric impact the Lagrangian grid can be generated using radial (x) and axial (y) lines as indicated in Figure 17. Here a generic mesh point (j, k) is shown. The mass associated with point (j, k) is contained within the dashed lines. The integral definitions of partial derivatives (see Appendix I) are employed in the equations of motion, the path of integration being the closed curve, I, II, III, IV. This allows mesh distortion without invalidation of the numerical scheme. The necessary loading conditions are applied at the mesh periphery and loading is accomplished by giving a velocity to all projectile mesh points.

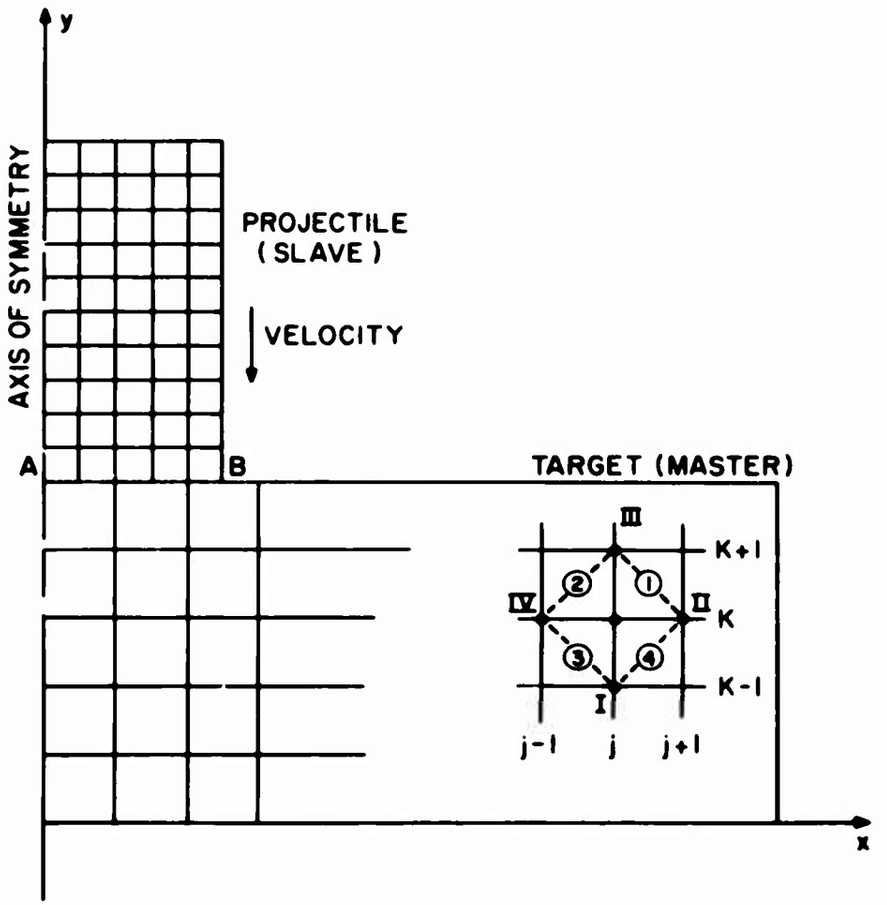

Figure 17. Lagrangian Grid at Time Zero for the Case of Axisymmetrix Impact

The first computation in the CRAM code is that of velocity, using the equations of motion. From these and the time step, new positions are determined. The velocities and positions calculated are associated with the actual mesh points. All other calculated quantities are cell-centered. After velocities and positions, the relative volume of each cell and its artificial viscosity are calculated. The strain increments are computed next and from these, in conjunction with the constitutive relation, the deviatoric stress components are determined. After the pressure is found for each cell from the equation of state, the total

stresses can be formed. From these components the principal stresses and directions are determined and finally total internal energy is computed. When these calculations are completed for each mesh point or cell, a new time step is computed and the cycle repeated.

For impact studies a special subroutine, called Slide, is necessary to allow a decoupling of the grid points at the projectile-target interface (A B in Figure 17). This routine is carried out in three basic steps:

1. The slave points (projectile mesh points on line A B, Figure 17) are allowed to move along the slide line (A B) as though it were a rigid boundary.

2. The grid points in the master side (target points along A B, Figure 17) are then allowed to move. Only mass on the target side is associated with this movement, but forces are allowed to act across the slide line.

3. The slave points are now forced to lie on the new position of the slide line so that voids will not be created. A correction term is applied to compensate for the motion perpendicular to the slide line.

Since the numerical scheme is based on continuum mechanics, special consideration must be given to post fracture phenomena. That is, the incorporation of failure criteria into the numerical scheme is insufficient for a complete solution of the impact problem since the governing equations used before failure no longer apply, at least in the affected vicinity of the failed portion of the material. Since this problem presents a major obstacle to the total solution of the impact problem, and since there are several methods of handling it, material failure criteria and their application in conjunction with special types of observed failure phenomena as well as possible methods of post-failure treatment are discussed in the following section.

SECTION VI

FAILURE PHENOMENA

The study of failure phenomena includes the formulation and application of failure criteria, a description of the failure process, and the development of methods for predicting and describing post-failure effects. Difficulties arise because of the complexity of material behavior when subjected to impact loading which manifests itself in the numerous material and configurational parameters associated with a specific failure mode. In addition, the use of a continuous numerical mesh for describing the discontinuous phenomena of failure requires that special consideration be given to the failed regions or an alteration of the numerical scheme be developed to allow the opening of voids in the computational mesh. Finally, relatively little is known about the physical nature of material failure; hence, the incorporation of a microscopic theory of failure into the numerical scheme would require further study, both theoretical and experimental. Following is a discussion of the various aspects of the mathematical treatment of failure phenomena.

6.1 Generalized Material Failure Criteria

From the standpoint of a continuum approach to material failure, the ideal generalized failure criteria would be in the form of a surface in stress space which, when intersected by the loading curve, would predict failure. Such a failure surface would not be rigid but would vary as a function of the material stress-strain history. Two observations can be made concerning a generalized failure surface for homogeneous, isotropic material. First, the surface must be axially symmetric with respect to the line in stress space having equal direction cosines with the principal stress axes. Furthermore, since the surface should be independent of the spatial axes, it can be written as a function of the stress

invariants. At present there is no suitable relationship for such a generalized theory to be incorporated into the material model for the case of impact. Until such relationships are developed, a more specific approach to material failure must be taken.

6.2 Specific Failure Criteria

The failure modes associated with projectile-plate impact were previously listed as fracture due to the initial stress wave, radial fracture behind the initial wave front, spallation, petalling and plugging. In addition to these, projectile shattering could occur for certain projectile materials impacting at higher velocities. These failure modes are well defined and their failure mechanisms are well enough understood so that failure criteria based on the current state of stress can be employed. For example, a maximum shear theory can be used for the case of plugging and maximum tensile stress for the case of spallation. The more difficult task which requires further study is to determine the exact value of fracture stress to be used since it is a function of the material loading history.

The criterion for fracture due to the initial stress wave is one of maximum compressive stress. The value of the stress to be used in this case does not depend on the loading history during the impact process since the plate fails when the initial stress wave passes through.

The criterion for radial fracture behind the initial wave front is one of maximum tensile stress. When the circumferential stress attains a critical value, radial fracture will occur. The value of the tensile stress to be used for this case is a function of the loading history since the initial stress wave has passed through the fracture region.

The criterion for spallation failure is also a maximum value of tensile stress. Fracture occurs when the axial normal stress in tension

is greater than a maximum value. In impact this situation may occur when a compression wave is reflected at a free surface. Again the value of maximum stress to be used depends on the loading history.

A maximum tensile stress failure criterion also seems best suited for predicting petalling type failure. Material that is pushed radially outward develops large circumferential tensile stresses which can cause either front or back petalling. In addition bending stresses can add significantly to the tensile stress at the back surface of a thin plate such that the tendency toward petalling failure is enhanced. Again the criterion is one of maximum tensile stress, the value of which is history dependent.

The criterion for plugging failure is one of maximum shear stress and the exact value to use is again a function of previous loading.

Finally, the criterion for the shattering of hard projectiles would be one of maximum absolute value of pressure.

The failure criteria are given here without the exact critical stress value since this varies not only for different materials but also according to the loading history. For this reason, some measure of loading history, such as plastic work, should be monitored. By studying both the stress patterns and material loading history throughout the impact process, definite fracture stress values should be obtainable for the specific failure modes and eventually combined to form a general failure criterion.

6.3 Numerical Applications of Failure Criteria

The development of failure criteria and their incorporation into the numerical scheme is but a first step in the study of fracture phenomena. The important and more difficult task is that of describing the

material behavior numerically after fracture has been predicted. There are at least three feasible ways to do this and the methods vary in degrees of difficulty.

In the simplest method, which is used here, the special failure criteria are chosen and the numerical solution is carried out in time to a point where gross failure is predicted. This ends the numerical portion of the problem and the residual effects are deduced from the dynamic state at the time of fracture. This method has the advantage that no special considerations for handling the fractured material need be incorporated into the numerical scheme. The only disadvantage is that further analysis is necessary after the completion of the numerical portion of the problem in order to predict residual effects.

An alternate method is to continue the numerical solution after failure is predicted but make the necessary adjustments to the stress and strain field in the vicinity of the fracture. For example, in the case of spallation, the normal stress perpendicular to the plane of failure can be zeroed out and an increment of strain applied to account for the initial separation. In the case of plugging, the shear stress can be zeroed out on the failure surface. This method of handling fracture is relatively simple but requires alteration of the numerical scheme for times after predicted failure.

Probably the most difficult method of handling fracture is to make numerical provisions for actual opening of the computational mesh along the fracture surface. For certain cases, as in plugging, the operation can be simplified by assuming fracture to occur instantaneously across the plate thickness and subsequently treat the plug as having a free surface. It is the general opening of voids, such as in the case of spallation where only an interior free surface is created, that requires significant alteration of the present numerical scheme.

Finally, it is possible to treat a region of severe fracture, such as a hard projectile subjected to impact at high velocities and which shatters by altering the equation of state in that region, to a form more descriptive of a particulate form of matter.

6.4. The Residual State

The residual state is defined as the dynamic state of the material and its configuration resulting from the impact and penetration process. In addition to the usual mass and velocity distribution of residual particles, it is important to know their shape as well as the internal state of the material. The observed effects of plate spacing on secondary penetration capabilities indicate that residual kinetic energy alone is insufficient for predicting the damage of subsequent plates in spaced armor configurations. Whether or not the residual fragments will break up further after impact is an important question.

Hence the development of any predictive penetration formula should include some realistic measure of the residual state.

SECTION VII

CRAM APPLICATIONS AND RESULTS

Two axisymmetric impact problems were solved using the CRAM computer code. These consisted of a steel cylinder with length to diameter ratio of one impacting a thin steel plate (problem III) and a thin aluminum plate (Problem III-A) respectively. The impact velocity was 0.61 km/sec for both cases as was the geometrical configuration shown in Figure 18. The material constants used are listed in Table I. The numerical results for the two problems will be discussed separately.

7.1 Problem III (Steel into Steel)

A Lagrangian grid similar to that of Figure 17 was generated using the exterior dimensions given in Figure 18. The impact velocity was 0.61 km/sec and the material parameters used in Equations (36), (37) and (38) are shown in Table I. The grid points were moved according to the equations of motion of Appendices I and II.

The actual computational grid used in the solution as plotted by the SC 4020 plotter is shown for various times throughout the solution in Appendix III. The letters superimposed on the grid cells in Figures III-1 through III-14 indicate compressive stress waves traveling through the material. The steeper gradients are indicated by letters nearer the end of the alphabet. The lettering allows the initial stress waves to be traced through both the projectile and target. After several reflections and wave interactions, however, stress-plots taken from the computer output are more informative.

Figures 19 through 22 are plots of the computed axial normal stress, Σ_{yy}, versus axial distance, y, along the axis of symmetry for problem III. The dashed vertical line is the initial projectile-target interface and y = 0 is the initial position of the free surface of the plate.

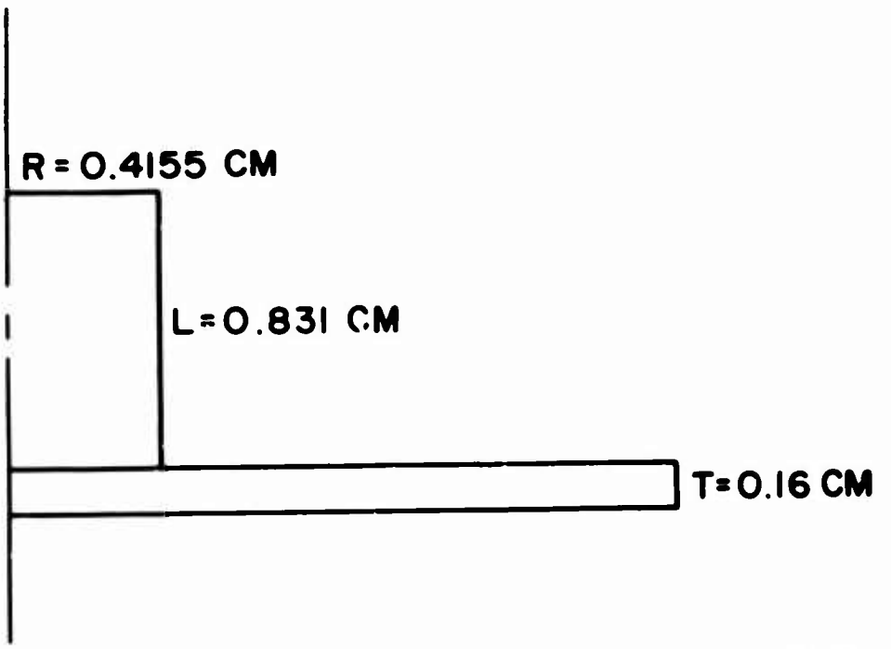

Figure 18. Geometrical Configuration for Problems III and III-A

TABLE I. MATERIAL CONSTANTS USED IN PROBLEMS III AND III-A

Material Constants	Projectile (III and III-A)	Target (III)	Target (III-A)
a_o	0	0	0
a_1	1236 kbars	1236 kbars	765 kbars
a_2	2452 kbars	2452 kbars	1659 kbars
a_3	5138 kbars	5138 kbars	428 kbars
a_4	0	0	0
b_o	2.2	2.2	2.13
b_1	2.2	2.2	2.13
b_2	0	0	0
b_3	0	0	0
μ	1930 kbars	1930 kbars	274 kbars
Y_o	5.44 kbars	5.44 kbars	2.80 kbars
P_{min}	-60 kbars	-60 kbars	-30 kbars
ρ_o	7.8 gm/cm^3	7.8 gm/cm^3	2.79 gm/cm^3

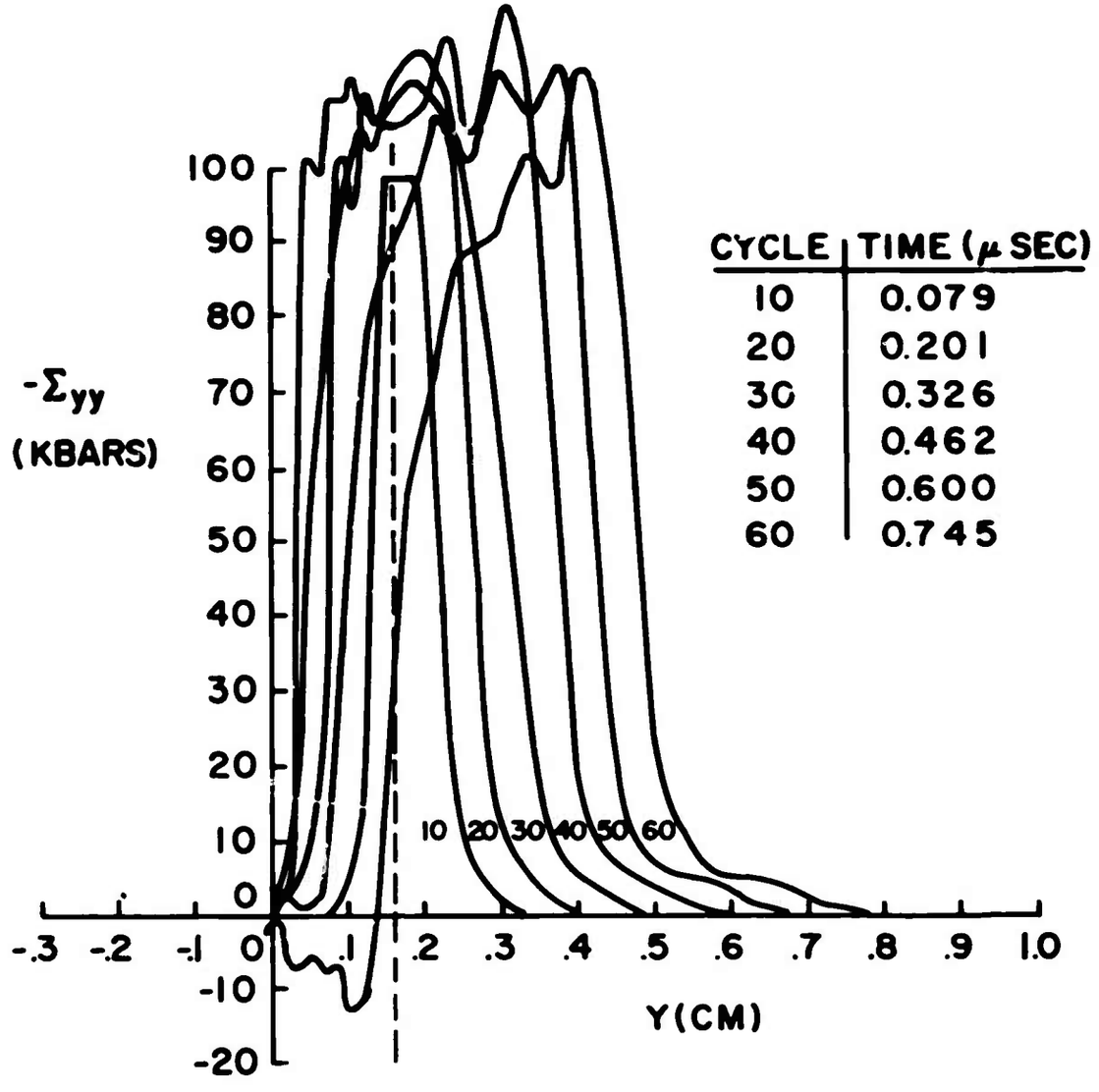

Figure 19. A Plot of Axial Stress Versus Axial Distance at Various Times for Problem III

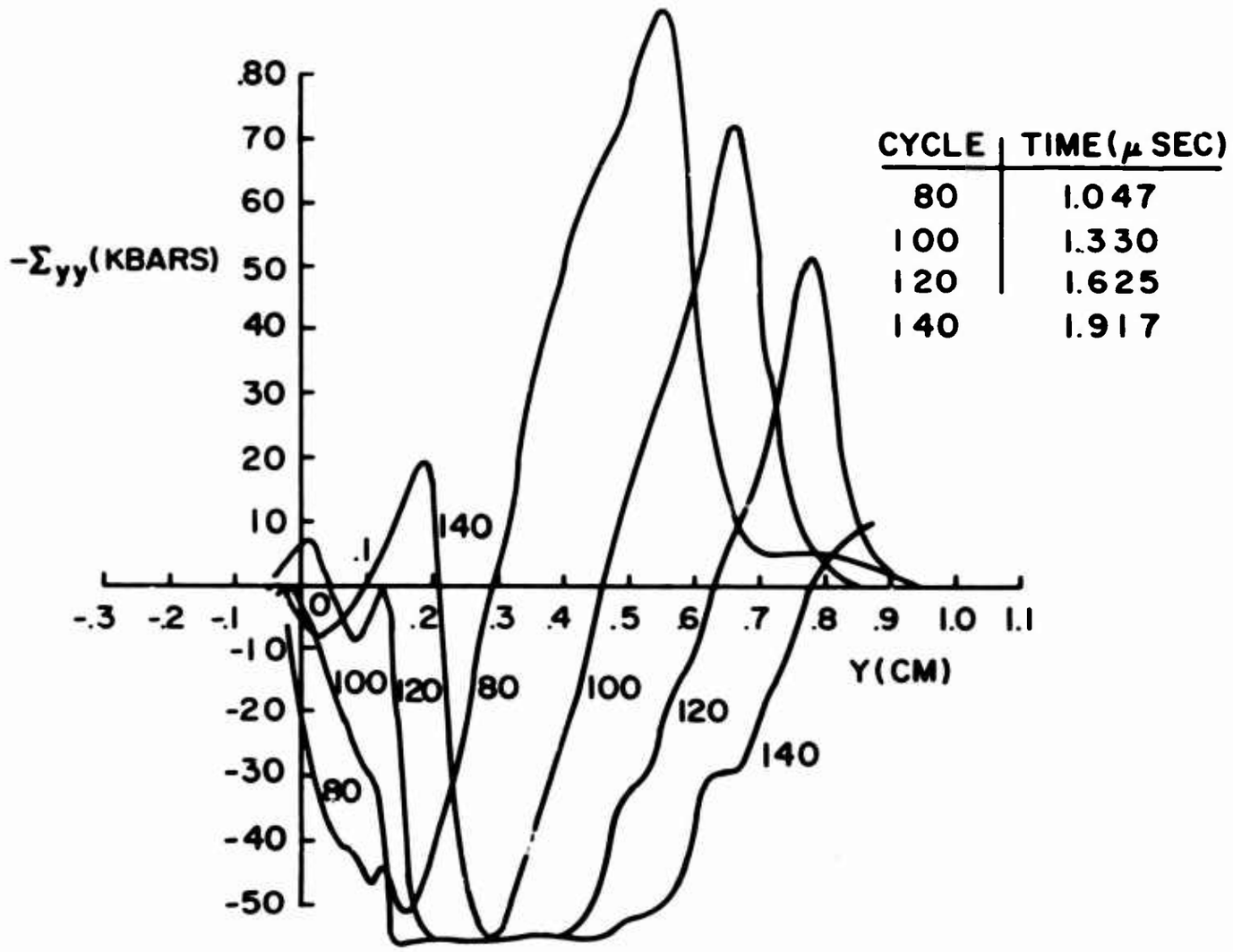

Figure 20. A Plot of Axial Stress Versus Axial Distance at Various Times for Problem III

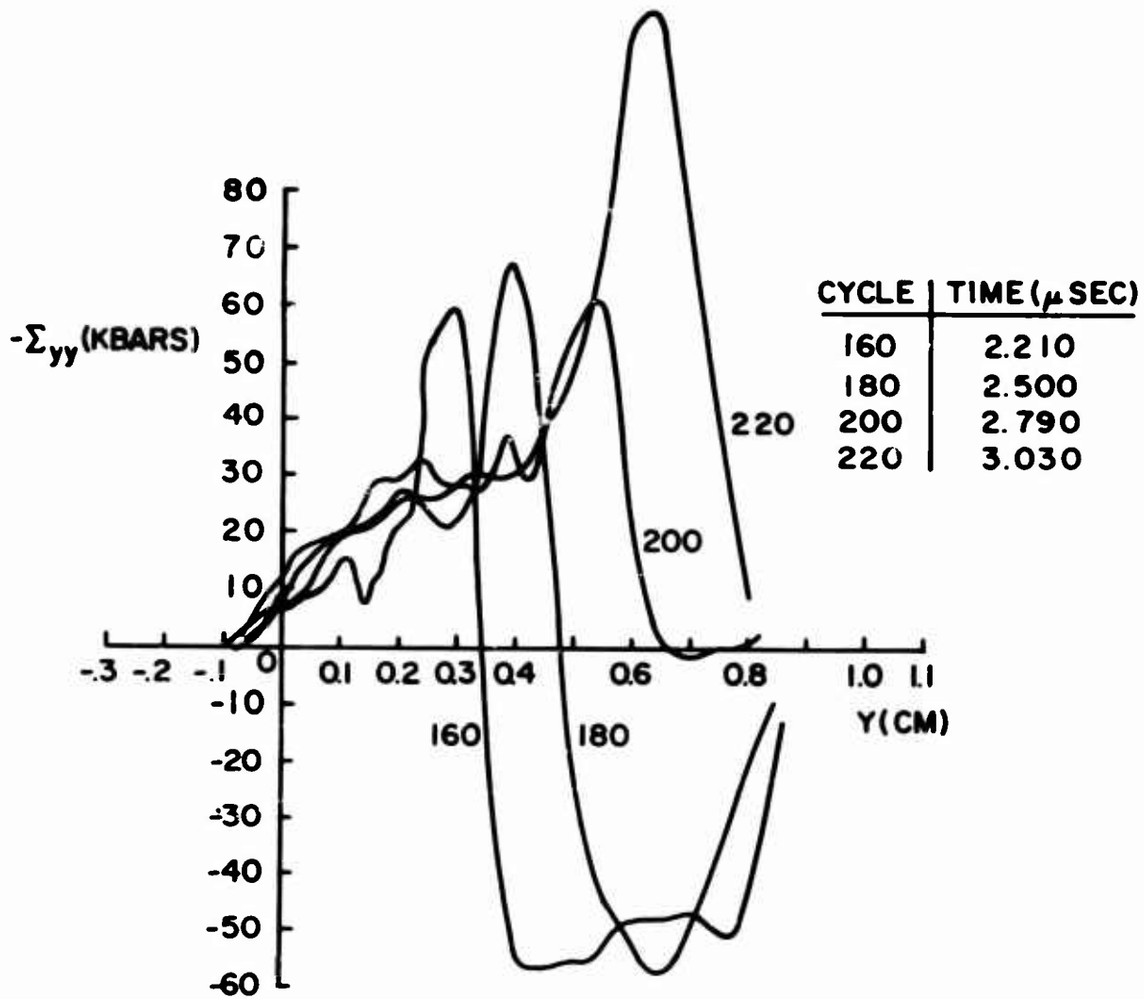

Figure 21. A Plot of Axial Stress Versus Axial Distance at Various Times for Problem III

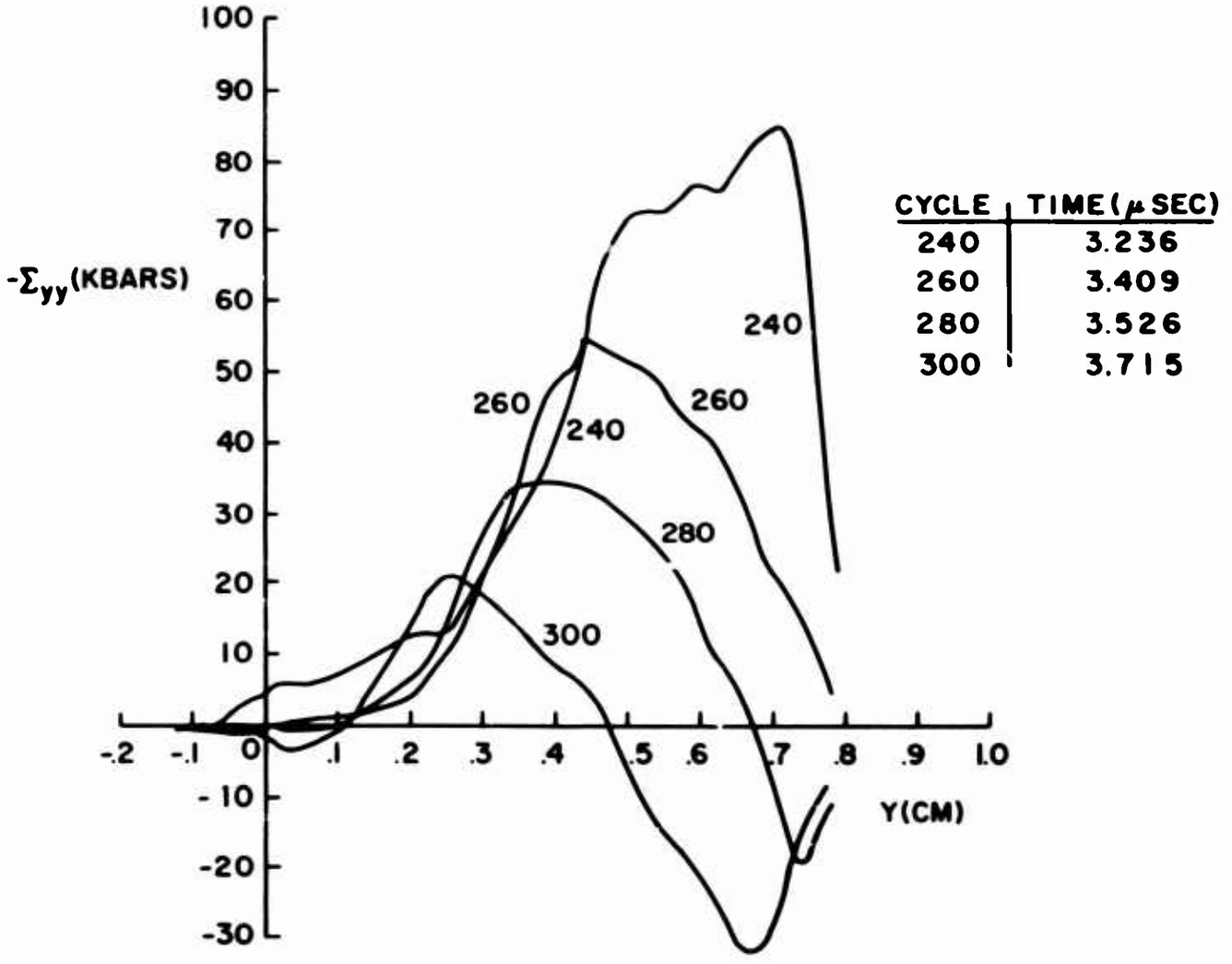

Figure 22. A Plot of Axial Stress Versus Distance at Various Times for Problem III

The various curves in each figure are for various times and are labeled cyclewise for convenience. The corresponding real times are given in μ-sec on each graph.

Several qualitative aspects of the impact process are evident in Figures 19 - 22. In Figure 19, the development of the initial stress pulse and its propagation into the target and projectile is clearly seen. The compressive wave reflects from the free surface of the target at a time of t = 0.394 μ sec. The resulting tensile wave propagates back into the target and attenuates the pressure even up into the projectile. The elastic precursor can also be seen in Figure 19 as the compressive wave travels up into the projectile.

In Figure 20 the attenuated compressive wave front is seen approaching the rear surface of the projectile. It too is reflected as a tensile wave. Also in Figure 20 an additional compressive wave pulse is seen building up in the vicinity of the projectile-target interface. The following reasons are given for the appearance of this wave. A rarefaction wave emanates from the free target surface at the projectile periphery and propagates behind the original compressive stress wave and is directed toward the axis. For thin plates, as in this case, this rarefaction wave reaches the rear free surface of the target before it reaches the axis of symmetry and is reflected as a compression wave. The direction of this compression wave has a component toward the axis and therefore is convergent in nature. Such a convergent wave builds in magnitude as it approaches the axis of symmetry and therefore gives rise to the observed compressive wave seen originating in Figure 20. It is also noticed in Figure 20 that a region of the projectile material has been subjected to the maximum allowable negative pressure.

In Figure 21, the compressive stress wave continues to build while the rarefactive wave from the free surface of the target is seen

arriving at the rear of the projectile. The reflection of this wave as a compression wave and its superposition on the already present compressive wave creates the large compressive spike observed in Figure 21.

In Figure 22 the two compressive waves have crossed causing a wider pressure pulse of lower magnitude. The wave moving toward the rear of the projectile is also seen to reflect as a tensile wave in Figure 22.

Before other results are presented, it is of interest to obtain a quantitative comparison of the results in the early stages of the impact process, i.e. before significant wave interaction occurs, with one-dimensional predictions.

Figure 23 shows the configuration of Problems III and III-A superimposed on a semi-infinite target. Comparisons can be made with predictions from one-dimensional wave dynamics in the early stages of impact before significant wave interactions and reflections occur. Several distances and times are of significance. These include the distances R_1 and R_2 measured along the axis from the impact interface to the points in the target and projectile respectively where the rarefaction wave eminating from the projectile periphery meets the axis. It is seen in Figure 23 that for the geometry shown, R_1 falls outside the plate. The distance x thus becomes significant which is the radial distance to the point where the rarefaction wave reflects from the free surface of the plate. The times at which the rarefaction wave reaches these points can also be calculated from one-dimensional theory and serve as a good check for the numerical solution. The times at which the original compression waves reflect from the rear surfaces of the target and projectile, t_T and t_L respectively are also important.

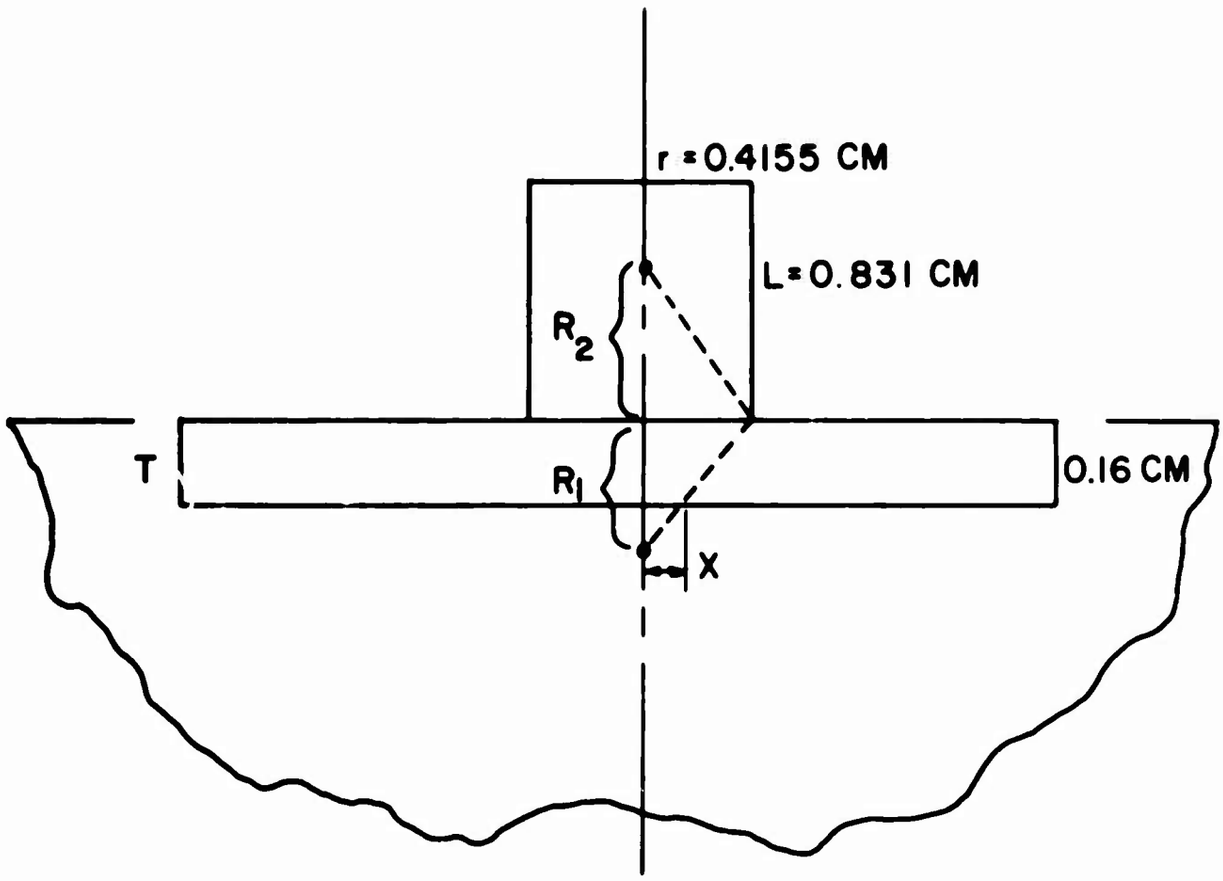

Figure 23. Diagrams for Showing One-Dimensional Theoretical Agreement in the Early Stages of Impact

From Hugoniot relationships it is shown that a good approximation of the shock speed is

$$U = A + Bu \tag{43}$$

where U is the shock speed, u is the particle speed and A and B are constants. In addition the pressure at the impact interface can be written as

$$p = \rho_o U u \tag{44}$$

where ρ_o is the normal density of the material.

By noting that the pressure at the instant of impact should give the same result at the interface for either the target or projectile, one can write

$$p_T = \rho_{oT} U_T u_T = \rho_{oP} \bar{U}_P u_P = p_P \tag{45}$$

where the subscripts T and P stand for target and projectile respectively and the bar indicates that Equation (43) must be altered to account for the projectile motion.

Hence

$$U_P = A_P + B_P \left(V_o - u_T\right) \tag{46}$$

where V_o is the impact velocity. At the interface

$$V_o - u_P = u_T \tag{47}$$

Substitution of Equations (46) and (47) into Equation (45) yields

$$\rho_{oT} \left(A_T + B_T u_T\right) u_T = \rho_{oP} \left[A_P + B_P \left(V_o - u_T\right)\right] \left(V_o - u_T\right) \tag{48}$$

or

$$u_T^2 + K_1 u_T - K_2 = 0 \tag{49}$$

where

$$K_1 = \frac{\left[\rho_{oT} A_T + \rho_{oP} A_P + 2 \rho_{oP} B_P V_o\right]}{\left[\rho_{oT} B_T - \rho_{oP} B_P\right]} \tag{50}$$

and

$$K_2 = \frac{\rho_{oP} V_o \left[A_P + B_P V_o\right]}{\left[\rho_{oT} B_T - \rho_{oP} B_P\right]} \tag{51}$$

For like materials as in Problem III, it is seen that Equation (48) yields a solution

$$u_T = \frac{V_o}{2} \tag{52}$$

Hence, from one-dimensional shock dynamics [27] the values of R_1 and R_2 in Figure 23 can be written as

$$R_1 = \frac{r \dot{R}_H}{\left[C_H^2 - \left(\dot{R}_H - u_T\right)^2\right]^{1/2}} \tag{53}$$

and

$$R_2 = \frac{r \left(\dot{R}_H - V_o\right)}{\left[C_H^2 - \left(\dot{R}_H - u_P\right)^2\right]^{1/2}} \tag{54}$$

where $u_P = V_o - u_T$, $\dot{R}_H$ is the shock speed in the undeformed material and C_H is the sound speed in the compressed material. For Problem III, $R_H = 4.06$ km/sec and $C_H = 4.42$ km/sec.

This gives a value of

$$R_1 = 0.728 \text{ cm}$$

and

$$R_2 = 0.62 \text{ cm}$$

It can be seen in Figure 23 that this value for R_1 would fall off the plate but the distance x can be calculated from the geometry to be 0.324 cm.

Now the times for the original stress wave to reach the rear surfaces of the plate and projectile and the initial rarefaction wave to reach the axis in the projectile and the rear surface of the plate a distance x from the axis can be written as

$$t_T = 0.394 \mu \text{ sec}$$

$$t_L = 2.05 \mu \text{ sec}$$

$$t_2 = 1.53 \mu \text{ sec}$$

$$t_x = 0.394 \mu \text{ sec}$$

It can be seen from Figure 19 that the initial stress wave reaches the free surface of the plate at approximately cycle 35 which agrees quite well with the value $t_T = 0.394 \mu$ sec. In Figure 20 it is seen that the initial stress wave reaches the rear of the projectile at approximately cycle 146 which also agrees very well with the value $t_L = 2.05 \mu$ sec. In Figure 20 the initial compressive wave moving toward the rear of the projectile is being degraded by the rarefaction wave emanating from

the projectile periphery which reaches the axis at t = 1.53 μ sec, in good agreement. Because of stress wave interactions at later times, the simplified one-dimensional theory can not be used beyond these early times; however agreement in the initial stages of impact is extremely good.

The deformed grid for Problem III shown at various times in Appendix III indicates that very little material distortion occurs in the target beneath the projectile while severe distortions occurs beneath the projectile periphery. This region is a region of predominantly shearing stress as seen from the graph in Figures 24 through 27 plotted by the SC 4020 plotter. In Figure 24 it is seen that the maximum shear stress near the impacted surface of the target in the early stages of impact attains a value of approximately 3 kbars. This seems to be the maximum value attained throughout the target for all times. Figure 27 indicates that the shear stress near the free surface of the target at t = 3.032 μ sec is also quite close to that value. According to a maximum shear theory of failure, failure will occur along the planes of maximur shear which in this case is a cylindrical surface of radius approximately equal to the projectile radius. These results indicate that plugging failure will occur at a time of approximately 3.123 μ sec (cycle 230), i.e. when the shear stress attains its maximum value throughout the plate thickness.

Other data such as the generalized plastic strain obtained by summing the incremental relationship

$$\overline{d\epsilon}_P = \left[\frac{2}{3}\, d\epsilon_{ij}\, d\epsilon_{ij}\right]_P^{1/2} \tag{55}$$

indicate the localized nature of the plastic deformation. The generalized plastic strain for t = 3.123 μ sec in Problem III is plotted versus

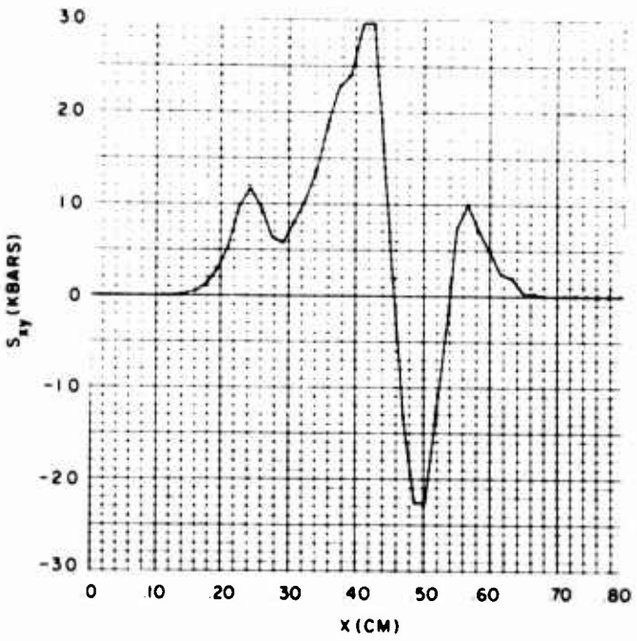

Figure 24. Shear Stress Versus Radial Distance Near the Impacted Surface of the Target at 0.3263 μsec for Problem III

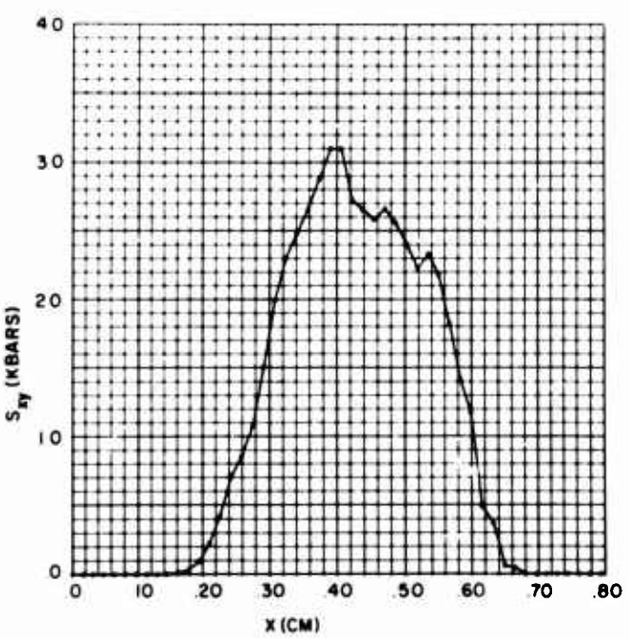

Figure 25. Shear Stress Versus Radial Distance at the Center of the Target at 0.3263 μsec for Problem III

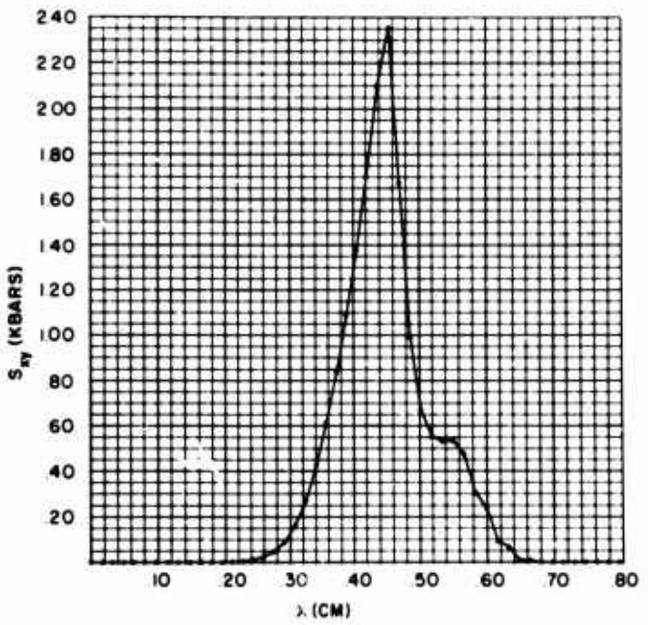

Figure 26. Shear Stress Versus Radial Distance Near the Free Surface of the Target at 0.3263 μsec for Problem III

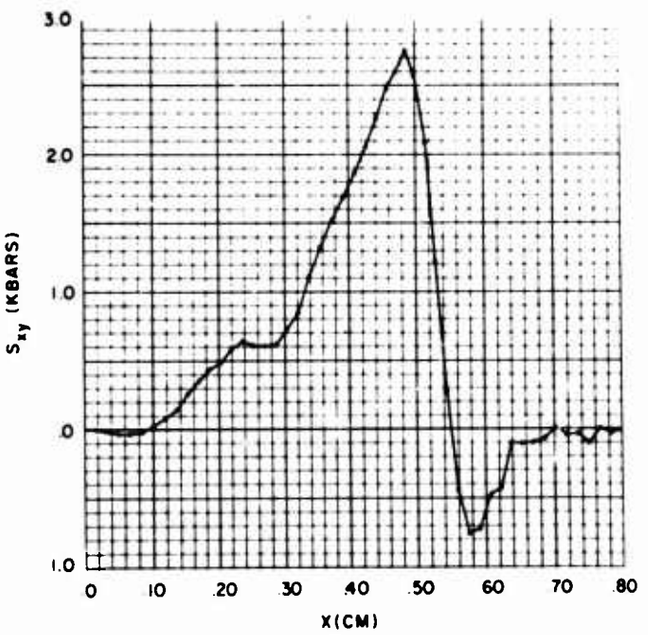

Figure 27. Shear Stress Versus Radial Distance Near the Free Surface of the Target at 3.032 μsec for Problem III

radial distance in Figure 28. The k-values of 2, 6, and 10 refer respectively to the free surface, the center plane and the impact surface of the plate. Figure 29 shows the plastic work defined as the sum of the increments

$$d W_p = \Sigma_{ij} \left[d \epsilon'_{ij} \right]_P \tag{56}$$

plotted versus radial distance at t = 3.123 μ sec for the same set of planes. Again the region to which severe plastic distortion is restricted is evident and supports plugging failure.

Figure 30 is a plot of internal energy versus radial distance at a time of 3.12 μ sec for the same set of planes in Problem III. The curve indicates that the plate material is heated in the narrow band where severe deformation takes place beneath the projectile periphery. This, of course, would be expected and indeed actual plugs have been inspected and markings attributed to high temperatures at the plug periphery have been observed.

Since the analysis of the results of Problem III indicate that plugging failure will occur, the estimated residual velocity should be compared with the results of the plugging theory of Recht and Ipson [20]. Since plugging failure was predicted to occur at t = 3.123 μ sec, the axial velocity versus radial distance at that time is plotted for the free surface, center plane and impact surface of the plate in Figure 31. It is seen from this figure that most of the plate material beneath the impacting cylinder is moving at a relatively steady rate but drops off to zero rapidly for radial values greater than the original projectile radius. From Figure 31 an estimated residual velocity for the plug and projectile combination might be 0.4 km/sec. Now by using the necessary parameters of Problem III which are given in Figure 18 and Table 1 together

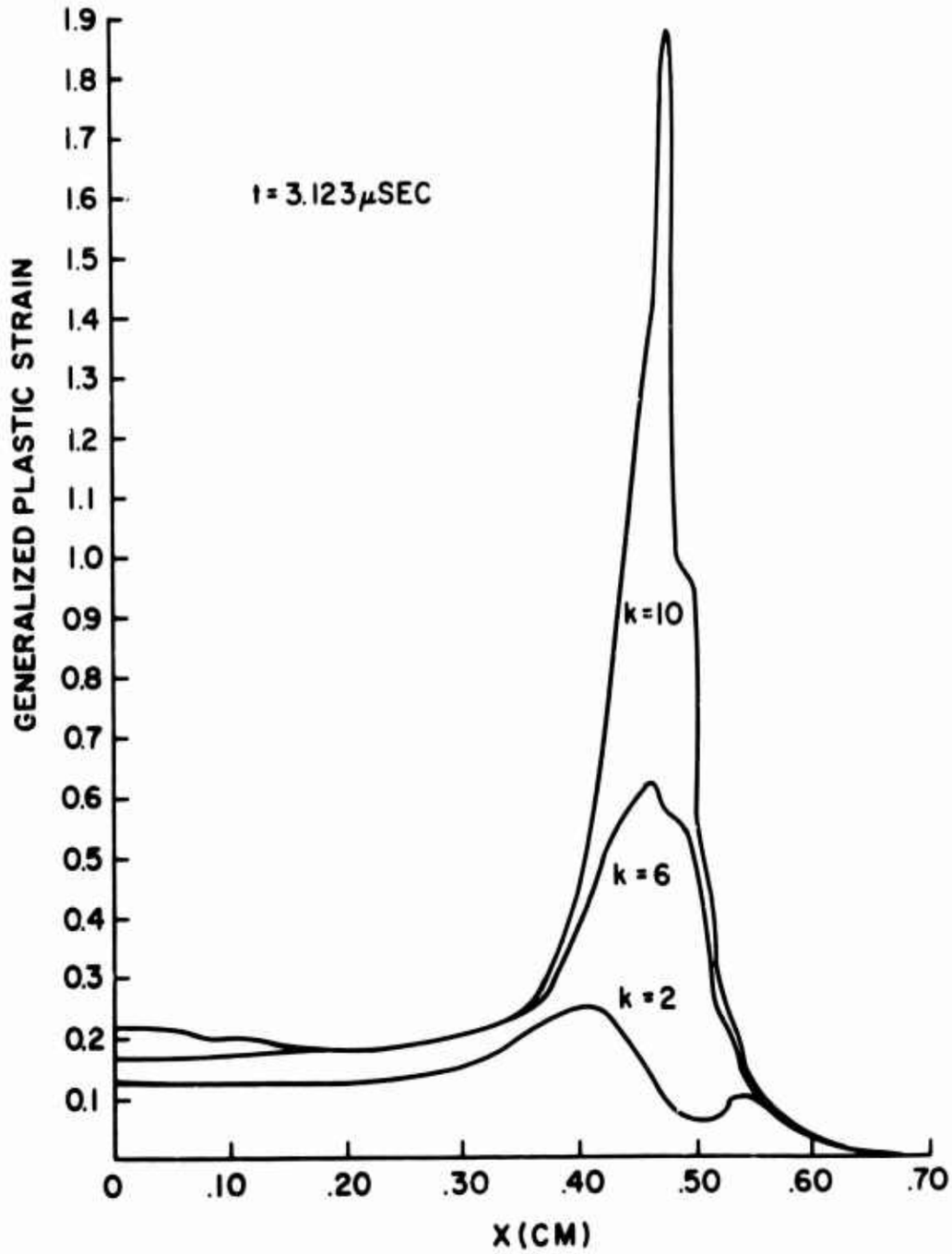

Figure 28. A Plot of Generalized Plastic Strain Versus Radial Distance for Problem III. The Time is t = 3.123 μsec and the k-values of 2, 6, and 10 Refer Respectively to the Free Surface, the Center Plane and the Impact Surface of the Plate.

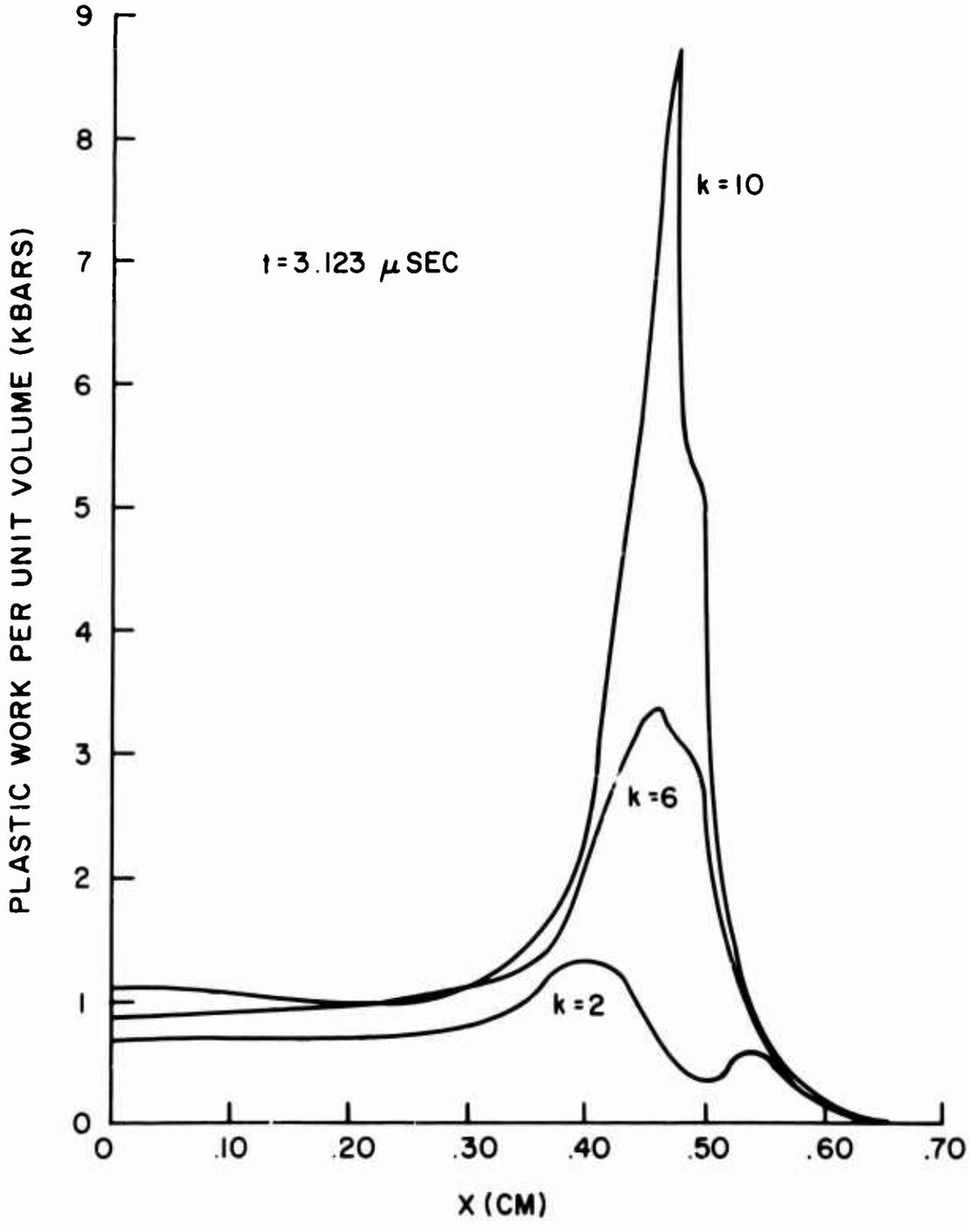

Figure 29. Plots of Plastic Work Versus Radial Distance for Problem III. The Time is t = 3.123 μsec and the k-values of 2, 6, and 10 Refer Respectively to the Free Surface, the Center Plane and the Impact Surface of the Plate

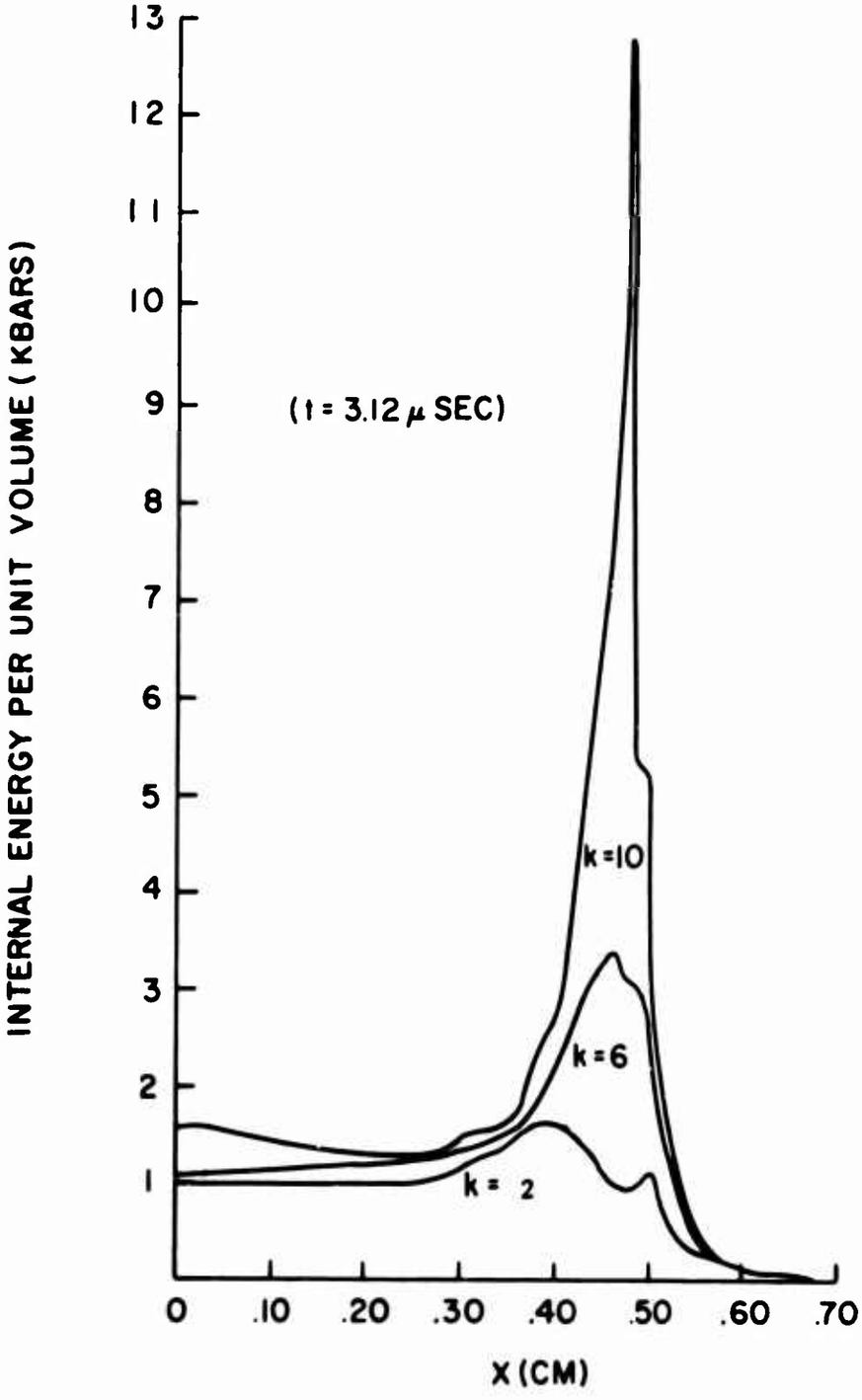

Figure 30. Plots of Internal Energy Versus Radial Distance for Problem III. The Time is 3.123 μsec and the k-values of 2, 6, and 10 Refer Respectively to the Free Surface, the Center Plane and the Impact Surface of the Plate

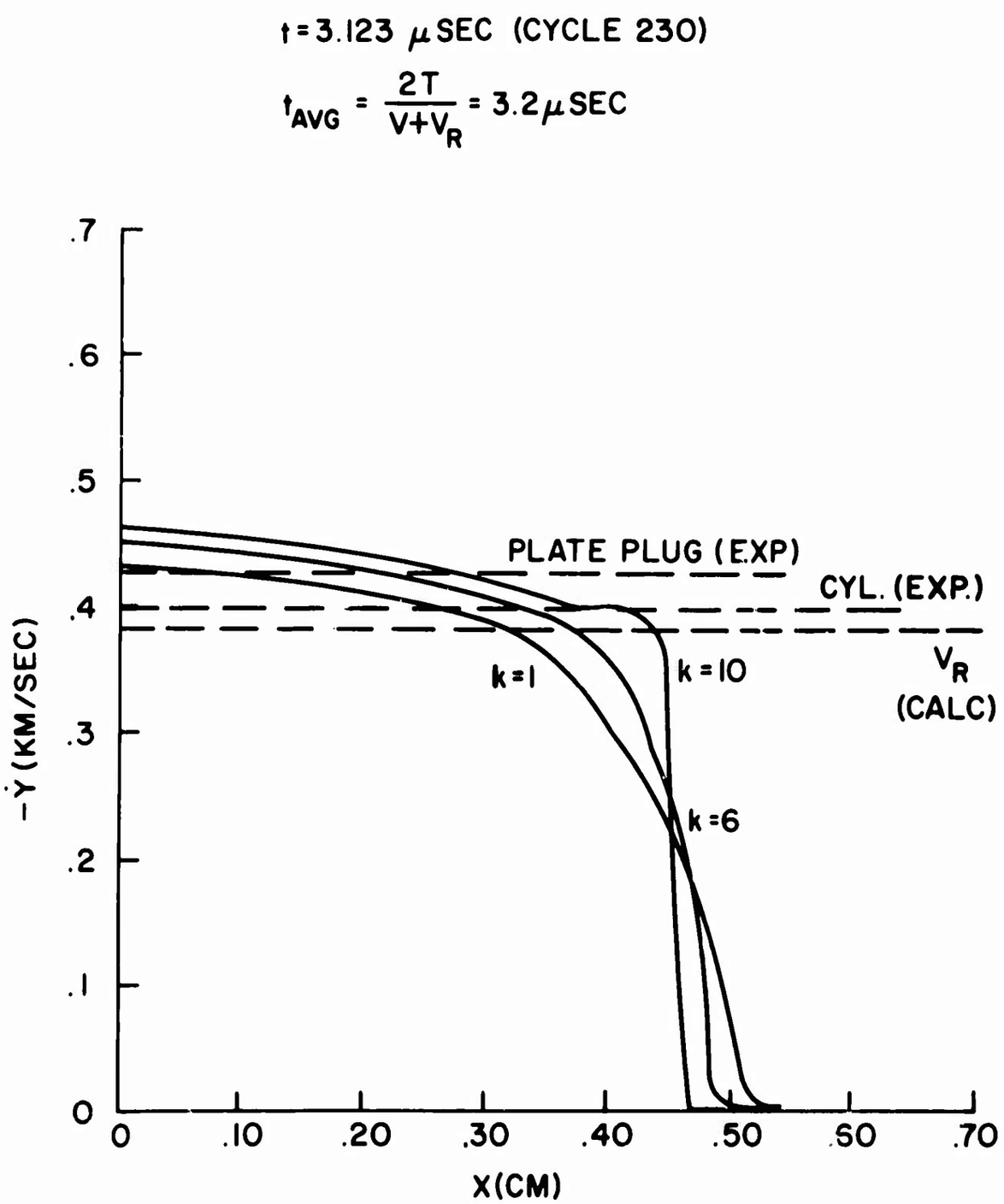

Figure 31. A Plot of Axial Velocity Versus Radial Distance for the Plate of Problem III. The Time is 3.123 μsec and the k-values of 1, 6, and 10 Refer Respectively to the Free Surface, the Center Plane and the Impact Surface

with the experimentally obtained value for the ballistic limit velocity of 0.406 km/sec [28] and a plug projectile diameter ratio of 1, Equation (6) can be used to obtain the theoretical value for residual velocity. This is found to be

$$V_r = 0.382 \text{ km/sec} \quad .$$

This value of residual velocity is shown by a dashed line on Figure 31. The agreement with the estimated value is extremely good. In addition an average time-to-failure can be approximated by

$$t_{AVG} = \frac{2\,T}{V_o + V_r} = 3.2\,\mu\text{ sec}$$

this value is also close to the predicted time of failure of $t = 3.123\,\mu$ sec determined from the analysis of the numerical results.

Next in order to obtain the exact shape of the plug the region of the target subjected to maximum shear stresses must be examined. Figure 32 shows the region of plate material subjected to shear stresses greater than 2 kbars. The crosses indicate the maximum values of shear for that given plane. It is assumed that fracture will occur along a line connecting the crosses. The vertical dashed line indicates the original projectile radius so it is seen that the plug will have a slightly greater radius than that of the original projectile. This is due to the fact that the projectile deforms radially after impact. The final predicted projectile-plug configuration is shown in Figure 33. From this figure the residual mass and kinetic energy can be calculated. Analysis shows that the plug material is only slightly compressed, mainly in the axial direction, and that the degree of compression increases with radial distance. The projectile, however, is compressed axially but expanded radially such that its overall state is one of expansion. The residual energies of the plug

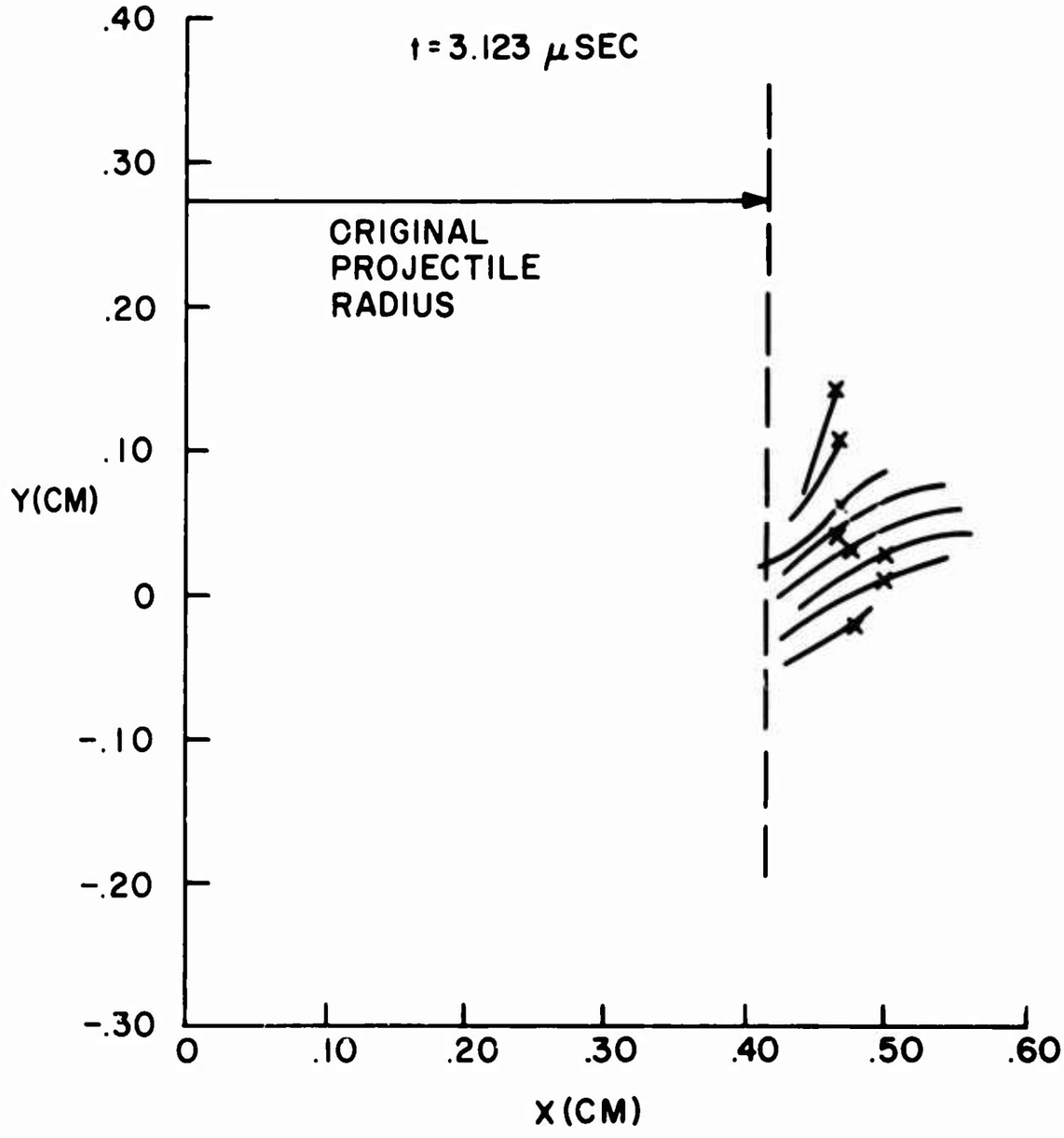

Figure 32. Shear Stresses Above 2 kbars are shown on a Section of the Plate Material at t = 3.123 for Problem III. The Crosses Indicate Maximum Stresses Acting on a Particular Plane. The Vertical Dashed Line Represents The Initial Projectile Radius

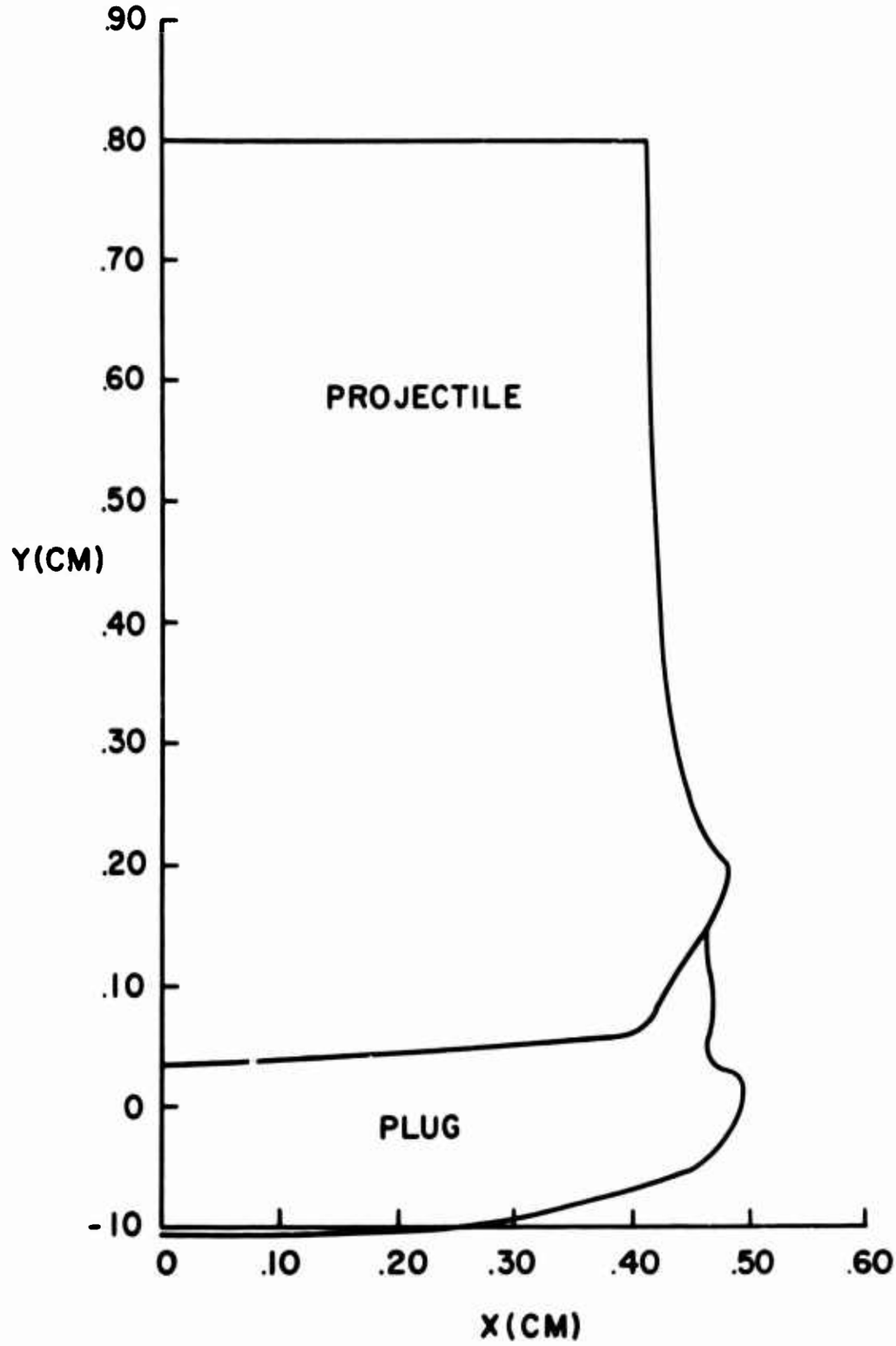

Figure 33. The Final Predicted Projectile-Plug Configuration

and projectile are 5.44×10^8 ergs and 2.56×10^9 ergs respectively and their combined kinetic energy is approximately 3.1×10^9 ergs. When this residual kinetic energy is compared with the initial value of 6.55×10^9 ergs at the instant of impact, it is noted that approximately 52.6% of the energy is either left behind in the target, dissipated or transferred to internal energy. Just how this energy is partitioned is not known and remains the subject of further study. It is believed, however, that for the case of plugging a high percentage of this energy remains in the plug-projectile combination as internal energy.

It is of interest to know whether or not the projectile or plug will fracture during or after the impact process. Complete fracture or shattering has been observed at the higher ranges of ballistic velocity, the severity decreasing with decreasing impact velocity through stages of partial fracture, contained spall and finally no failure at all. Figure 20 shows that axial stresses do attain the largest allowable tensile stress during the impact process so that fracture is predicted. Figures 34 and 35 are traces of the projectile at times of $t = 1.33\ \mu$ sec and $t = 1.92\ \mu$ sec respectively. The cross-hatched areas represent regions subjected to tensile stresses high enough to initiate fracture. Although the stress distribution is complex, the tensile stresses in these regions are mainly due to the rarefaction wave from the free surface of the plate and radial material flow in the projectile. Thus the numerical results predict contained failure in the projectile in the form of spall or radial crack initiation. The exact shape of the fractured region or its effect on the unfractured projectile material can not be predicted at this stage since no alteration in the numerical scheme other than limiting the tensile stresses to their maximum value has been carried out.

The steel-steel impact problem discussed here has been reproduced experimentally at the Air Force Armament Laboratory, Eglin Air Force Base, Florida.

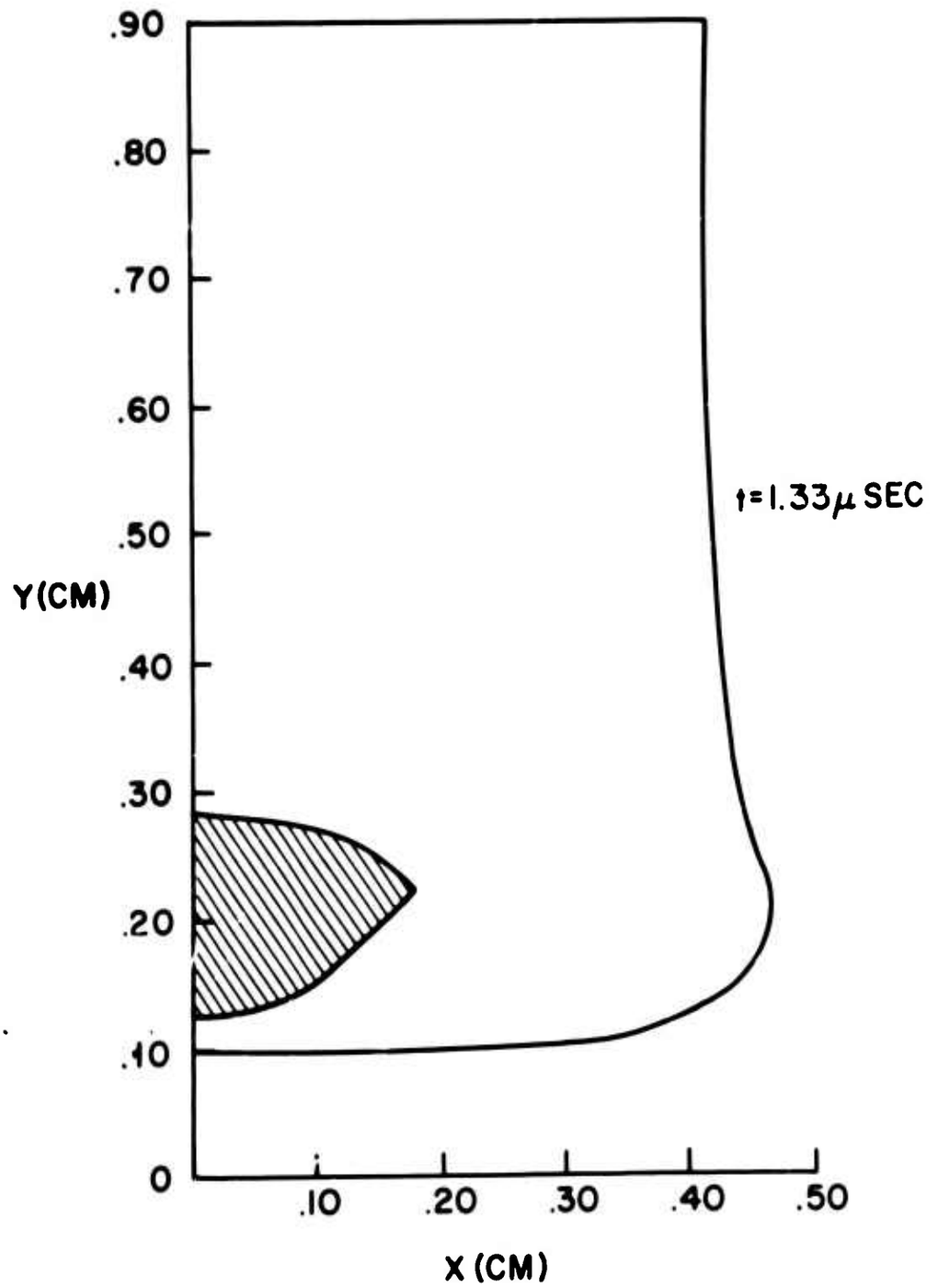

Figure 34. A Plot of the Projectile Shape for Problem III at t = 1.33μ sec. The Cross-Hatched Region Indicates that the Material has been Subjected to the Maximum Allowable Tensile Stresses

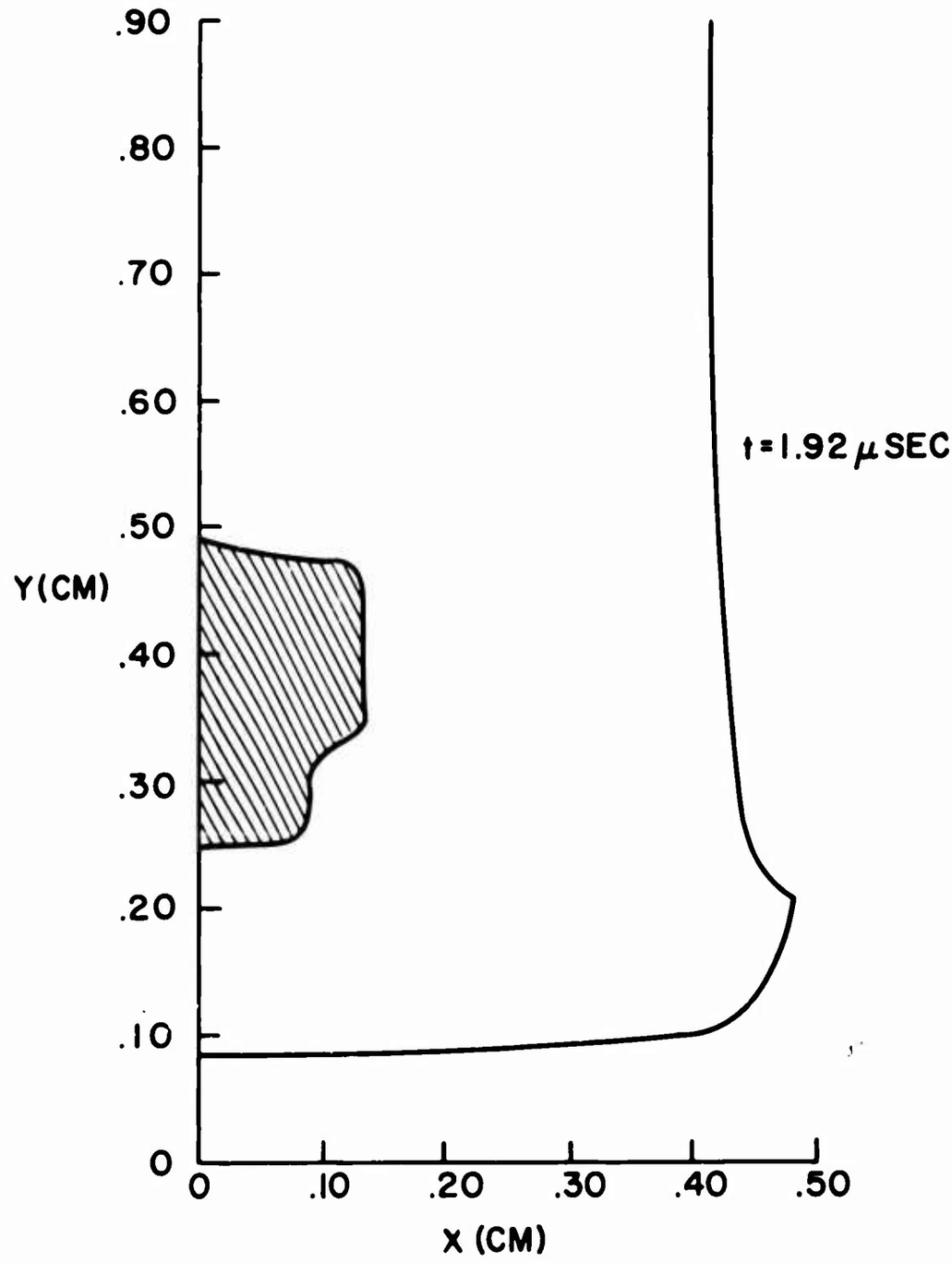

Figure 35. A Plot of the Projectile Shape for Problem III at t = 1.92 μsec. The Cross-Hatched Region Indicates that the Material has been Subjected to the Maximum Allowable Tensile Stresses

The raw data for eight shots are given in Table IV-1 of Appendix IV. Also in Appendix IV, Figures IV-1 and IV-2 are sample prints of the x-ray negatives showing projectile-target configurations before and after impact. Figure IV-2 indicates that the particular projectile shown has experienced some degree of yaw before impact.

The averages over seven shots (nos. 2 through 8 of Table IV-1) of the plate plug and cylinder residual velocity are shown in Figure 31. Agreement is quite good with both the numerically predicted residual velocity and the value obtained from the plugging theory of Recht and Ipson [20]; although the calculated value is somewhat lower.

Since fracture initiation in the projectile is predicted for the steel-steel impact problem as seen in Figures 34 and 35, it is of interest to obtain an experimental verification. Figures IV-3 through IV-6 of Appendix IV are post-impact photographs of cross-sections of the projectile. Figure IV-3 is a cross-section of the projectile shown in Figure IV-1 while Figure IV-4 is an enlargement of the region of predicted fracture initiation. Similarly, Figures IV-5 and IV-6 are the cross section and enlargement of the region of predicted fracture initiation for the projectile shown in Figure IV-2.

Fracture markings are clearly in evidence as predicted numerically. The arrow shown on Figures IV-4 and IV-6 indicate the direction of projectile travel. It should be noted that the fracture markings shown in Figure IV-5 are off center due to the pre-impact yaw experienced by that projectile as seen in Figure IV-2.

7.2 Problem III-A (Steel into Aluminum)

The dimensions for problem III-A are identical to those for Problem III and are given in Figure 18. The impact velocity of 0.61 km/sec is also the same. The only difference is that an aluminum target is substituted for the steel target of Problem III. The material constants used are given in Table I. The deformed grid plots for Problem III-A are given in Appendix V.

Figures 36 through 38 are plots of axial stress versus axial distance for various times for Problem III-A. The development of the initial pressure pulse, its propagation through the target and projectile and reflections from the free target surface can be traced.

The calculated times at which the initial stress wave reaches the free surfaces of the plate and projectile respectively are

$$t_T = .27\,\mu \text{ sec}$$

$$t_L = 2.04\,\mu \text{ sec}$$

Also by using values of $R_H = 5.92$ km/sec and $C_H = 6.085$ km/sec for the aluminum target and $C_H = 4.096$ km/sec for the projectile, it is found that

$$R_2 = 1.3 \text{ cm}$$

and

$$x = 0.35 \text{ cm}$$

Hence the times for the rarefaction wave which emanates from the impacted surface at the projectile periphery to reach the projectile axis and the rear surface of the plate respectively are

$$t_2 = 2.2\,\mu \text{ sec}$$

$$t_x = 0.27\,\mu \text{ sec}$$

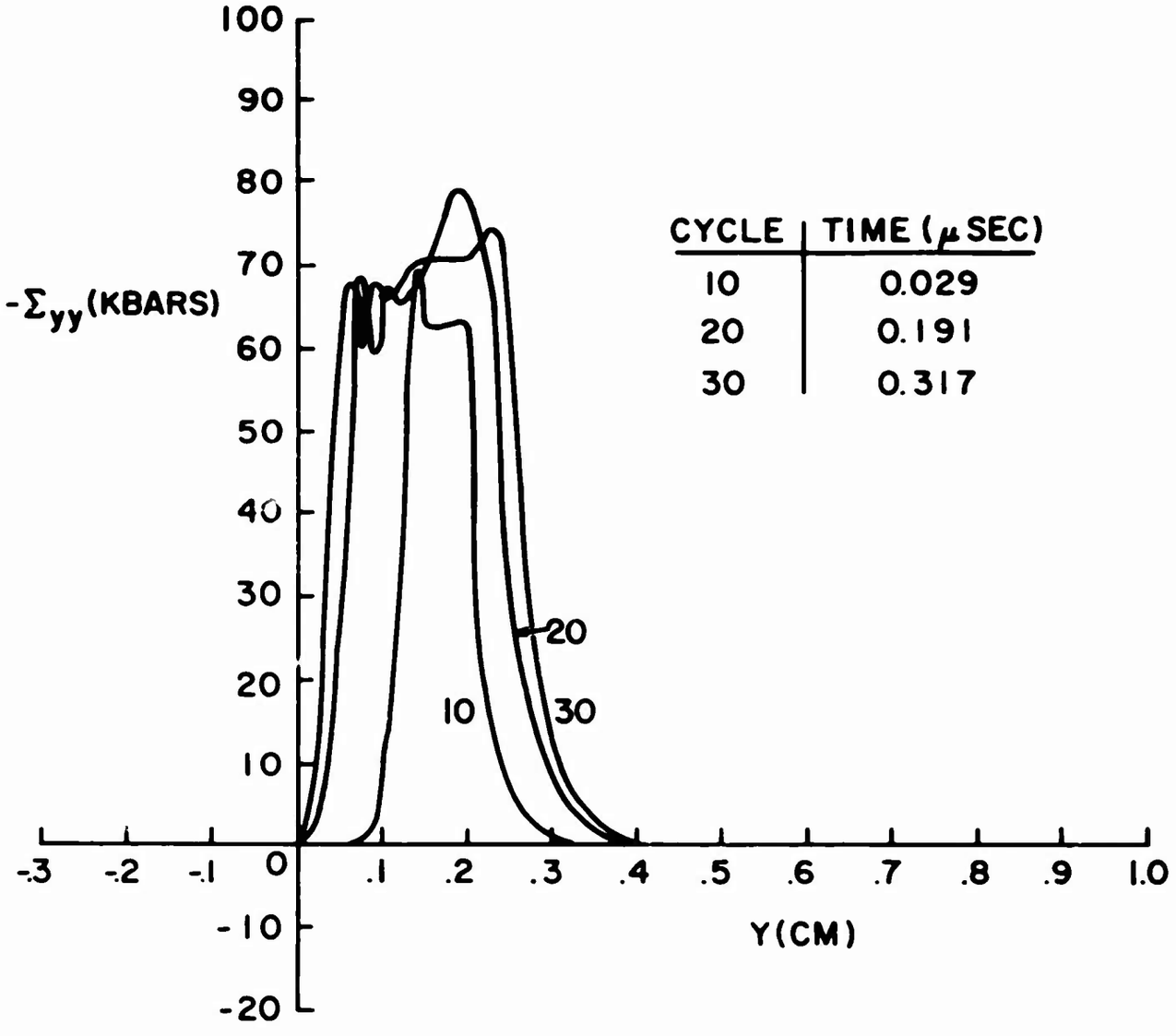

Figure 36. Plots of Axial Stress Versus Axial Distance at Various Times for Problem III-A

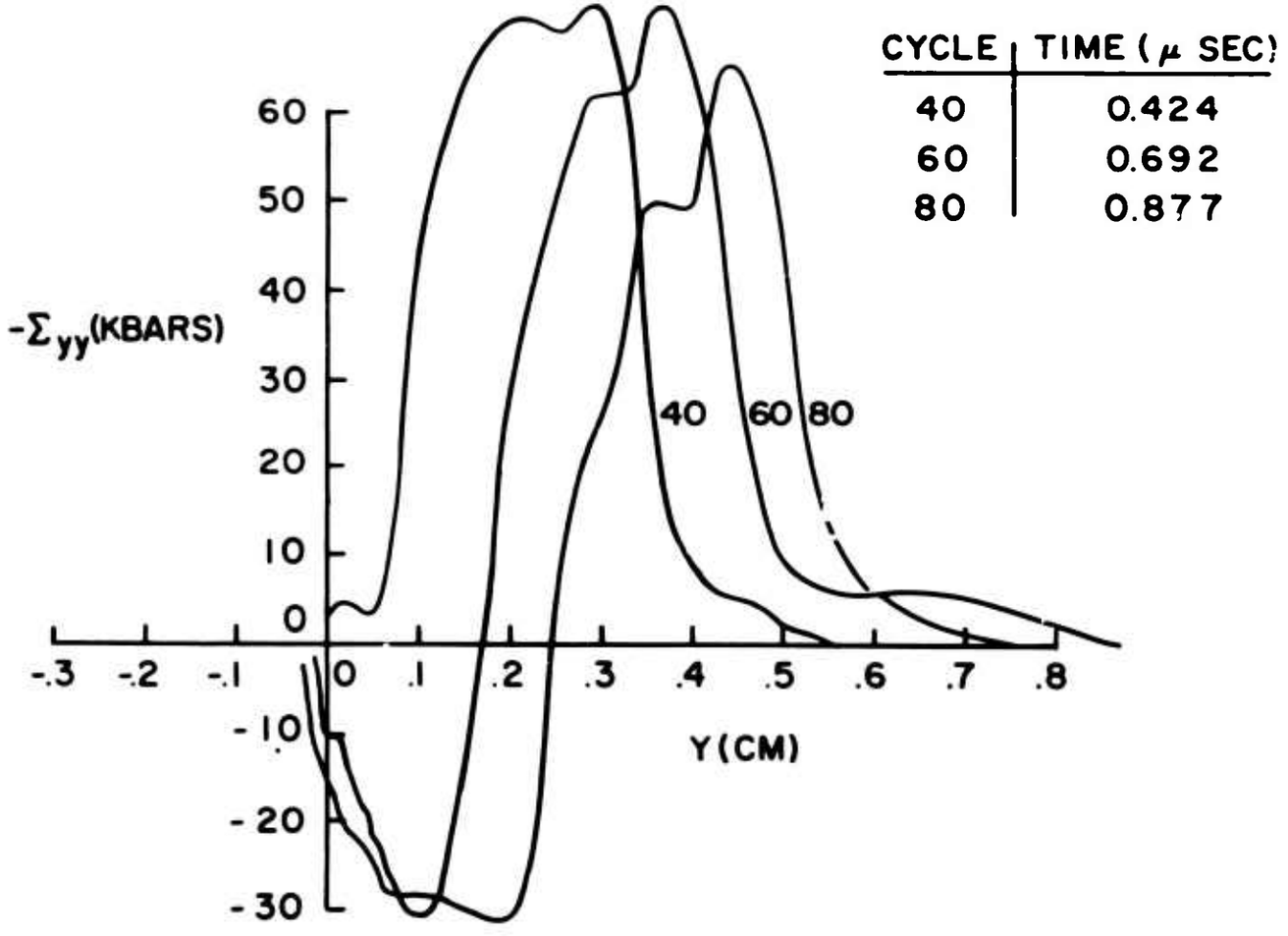

Figure 37. Plots of Axial Stress Versus Axial Distance at Various Times for Problem III-A

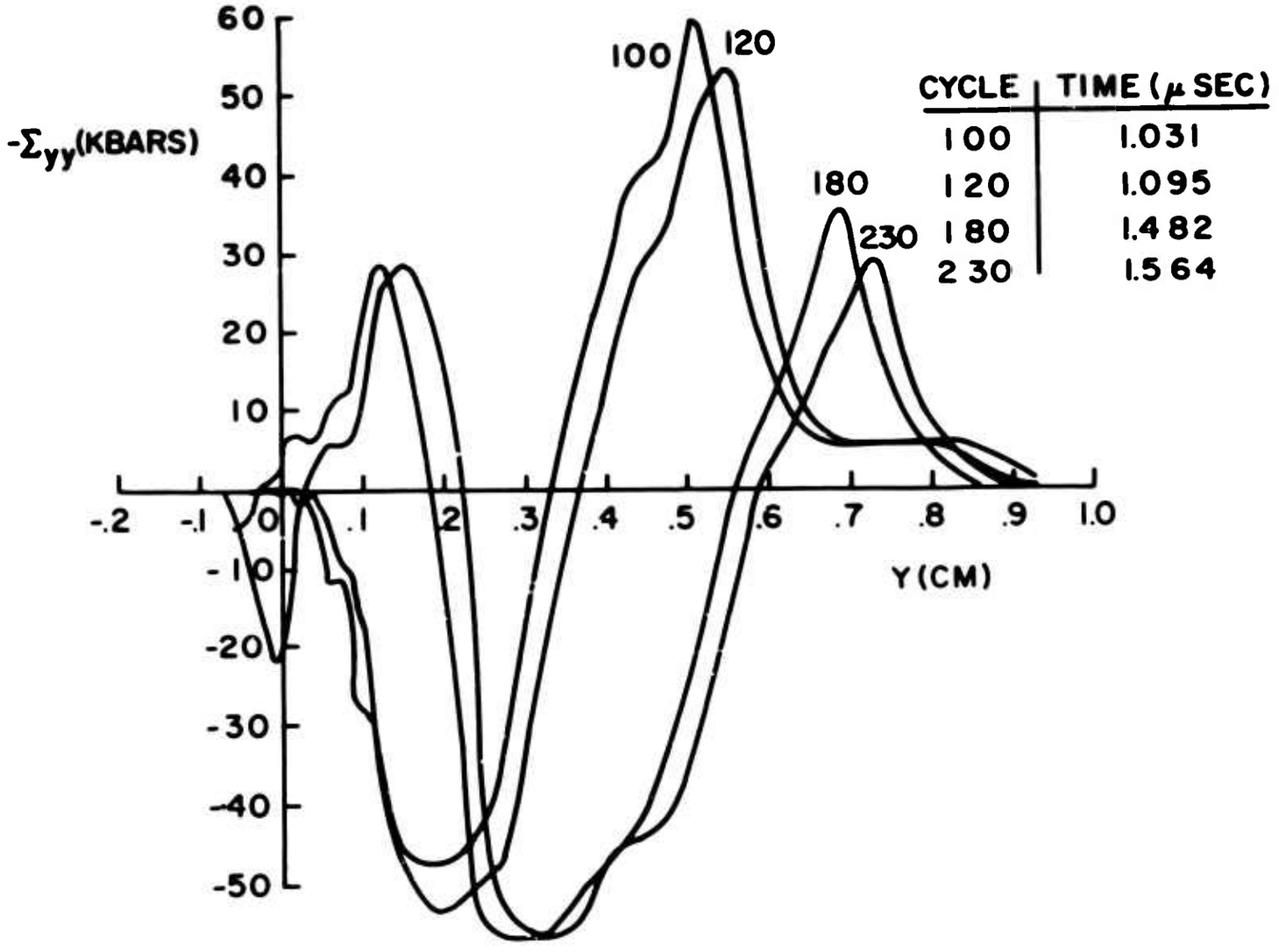

Figure 38. Plots of Axial Stress Versus Axial Distance at Various Times for Problem III-A

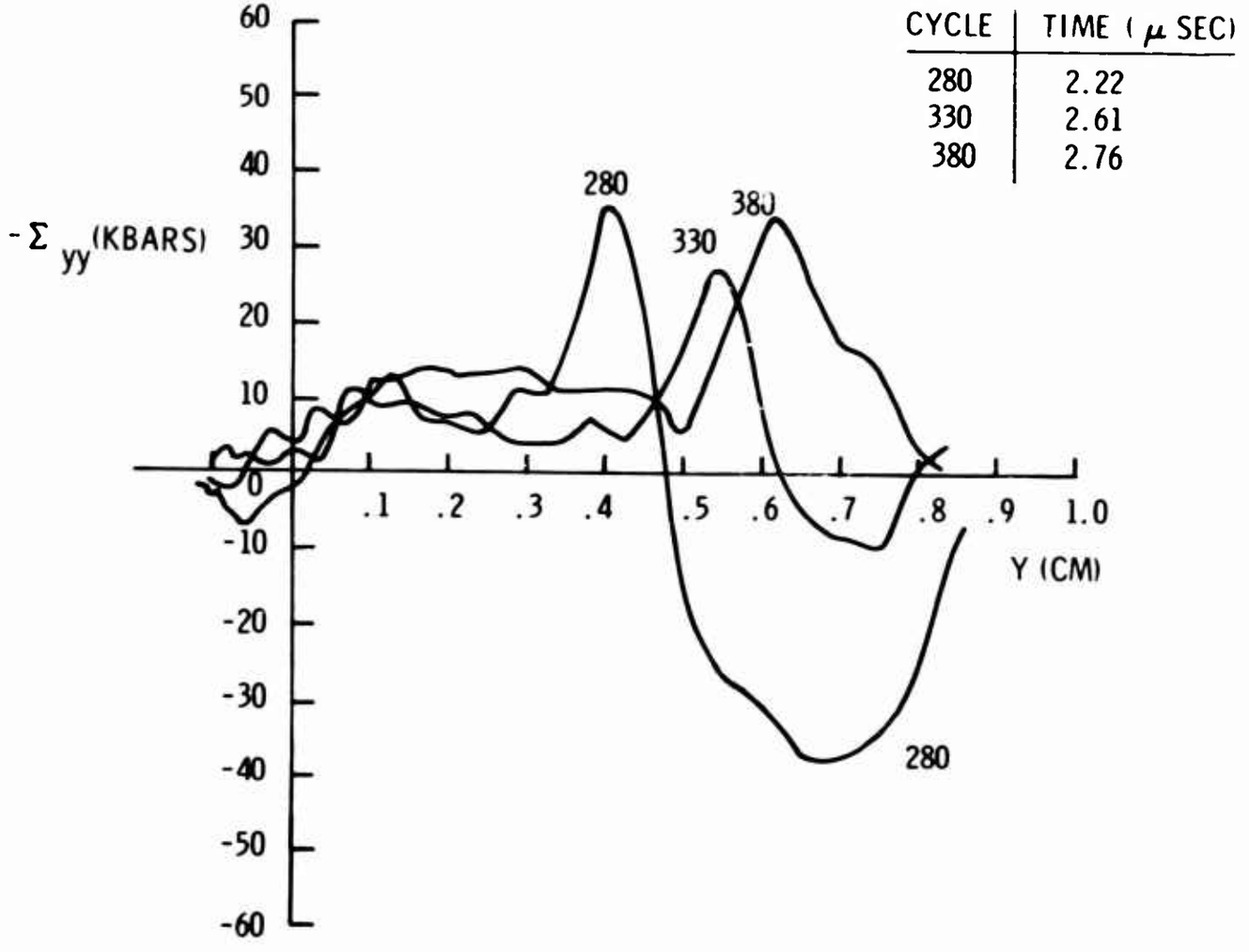

Figure 39. Plots of Axial Stress Versus Axial Distance at Various Times for Problem III-A

These values of time agree reasonably well with prediction of the numerical solution.

By comparing the deformed grid plots for Problem III-A in Appendix V with those for Problem III in Appendix III, it is seen that the target lip formed in the aluminum target is much greater. This is due, of course, to the difference in target materials for the two cases, aluminum being more ductile than steel.

Analysis of the numerical results for the steel-aluminum impact, III-A, indicates that plugging type failure should be expected here also. Figures 40-42 are plots of shear stress versus radial distance at the impacted surface, the center plane and the free surface of the aluminum plate respectively. These plots represent the shear stress distribution at time t = 2.757 μsec which corresponds to the time at which the stresses attain values of approximately 1.5 kbars completely through the plate thickness. It will be assumed that plugging failure occurs at this time and no further numerical calculations will be carried out.

Figures 43 and 44 are plots of generalized plastic strain and plastic work versus radial distance for various planes in the target at the time of failure.

It can be seen from these figures that the major plastic deformation, at least at the center plane (k = 6) and the impacted surface (k = 10), is due to shear stresses which develop beneath the projectile periphery. On the free surface of the plate (k = 2), however, it is seen that maximums occur at the axis as well as beneath the projectile periphery. The maximum at the axis is due in part to the tensile stresses caused by plate bending. The extent of this bending is shown in Figure 45 which is a trace of the free surface of the plate at t = 2.757 μ sec. For comparison, a plot of the free surface of the steel plate of problem III is shown at a comparable time. Because of the difference in material, more bending is observed for the Aluminum plate. However, this bending is not sufficient to create the necessary circumferential stresses for petalling failure at this time. The question is, at the

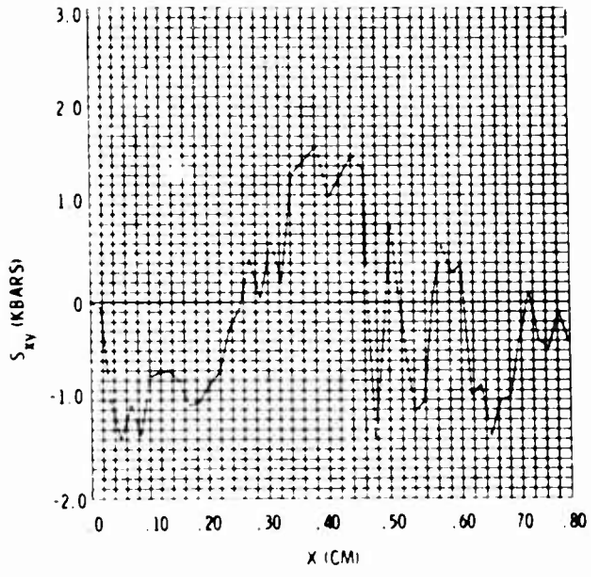

Figure 40. Shear Stress Versus Radial Distance Near the Impacted Surface of the Target at t = 2.756 μ sec for Problem III-A

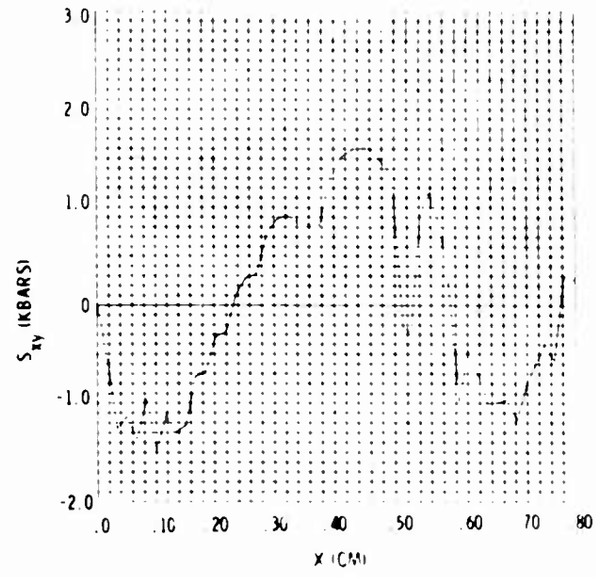

Figure 41. Shear Stress Versus Radial Distance at the Center Plane of the Target at t = 2.756 μ sec for Problem III-A.

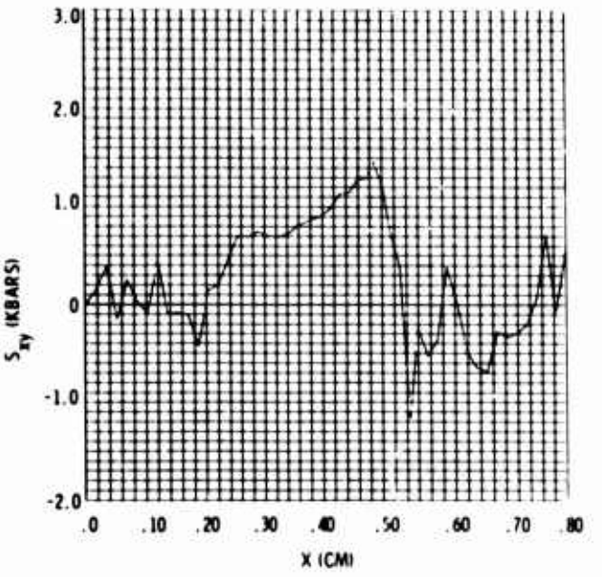

Figure 42. Shear Stress Versus Radial Distance at the Free Surface of the Target at t = 2.756 μsec for Problem III-A

time of failure, which mechanism will be dominant at the rear surface of the plate, shear failure at the projectile periphery or tensile failure near the axis? Since the impact velocity is well above the ballistic limit velocity for this case, it is believed that the former will occur and therefore cause plugging failure. Hence from Equation 16 of the theory of Recht and Ipson the value of residual velocity is found to be

$$V_r = 0.549 \text{ km/sec}$$

This gives the average time to fracture as calculated by Equation (57) as

$$t_{AVG} = 2.76\,\mu \text{ sec}$$

which agrees remarkably well with the predicted failure time.

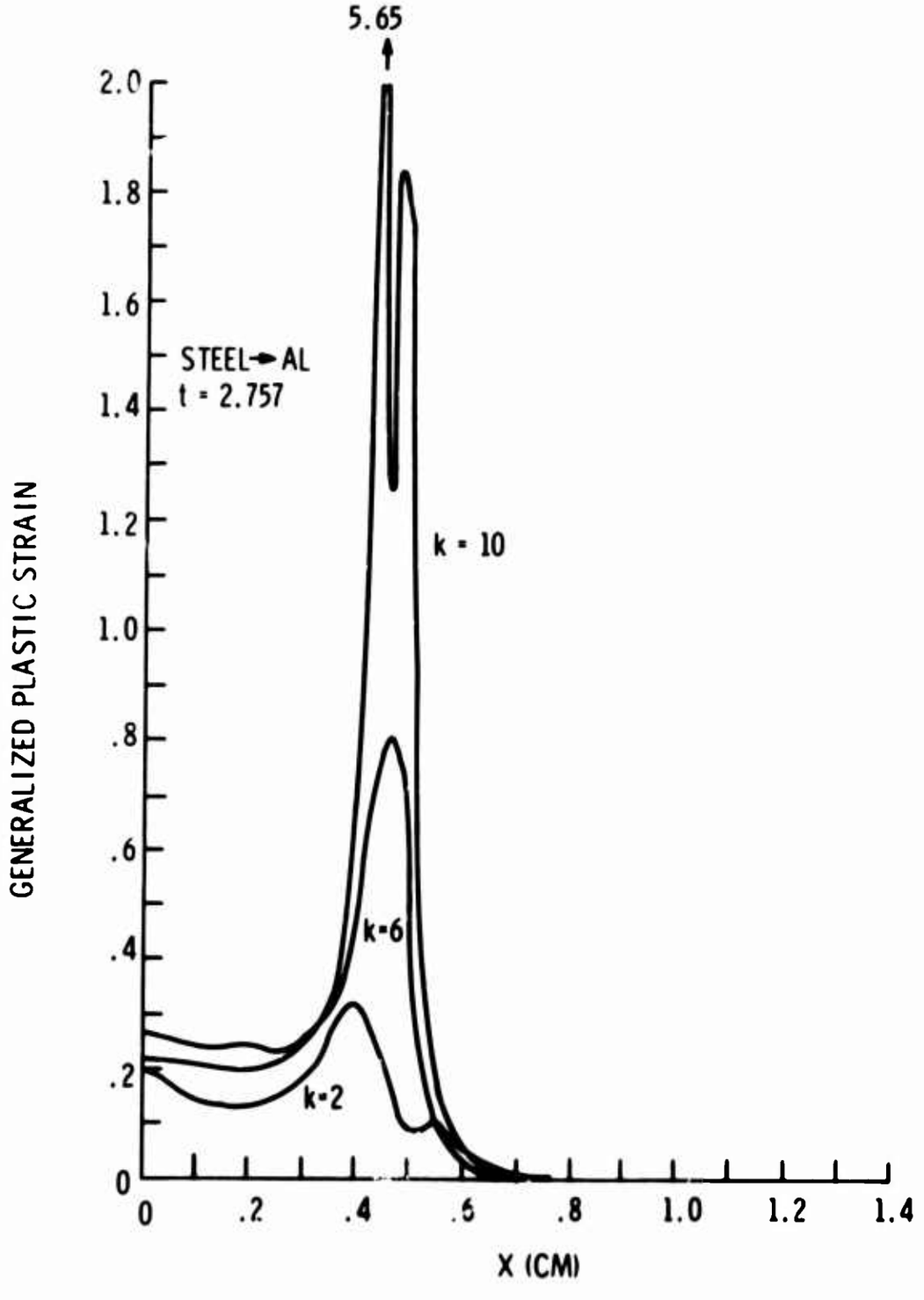

Figure 43. Plots of Generalized Plastic Strain Versus Radial Distance for Problem III-A. The Time is 2.751 μsec and the k-values of 2, 6, and 10 Refer Respectively to the Free Surface, the Center Plane and the Impact Surface of the Plate

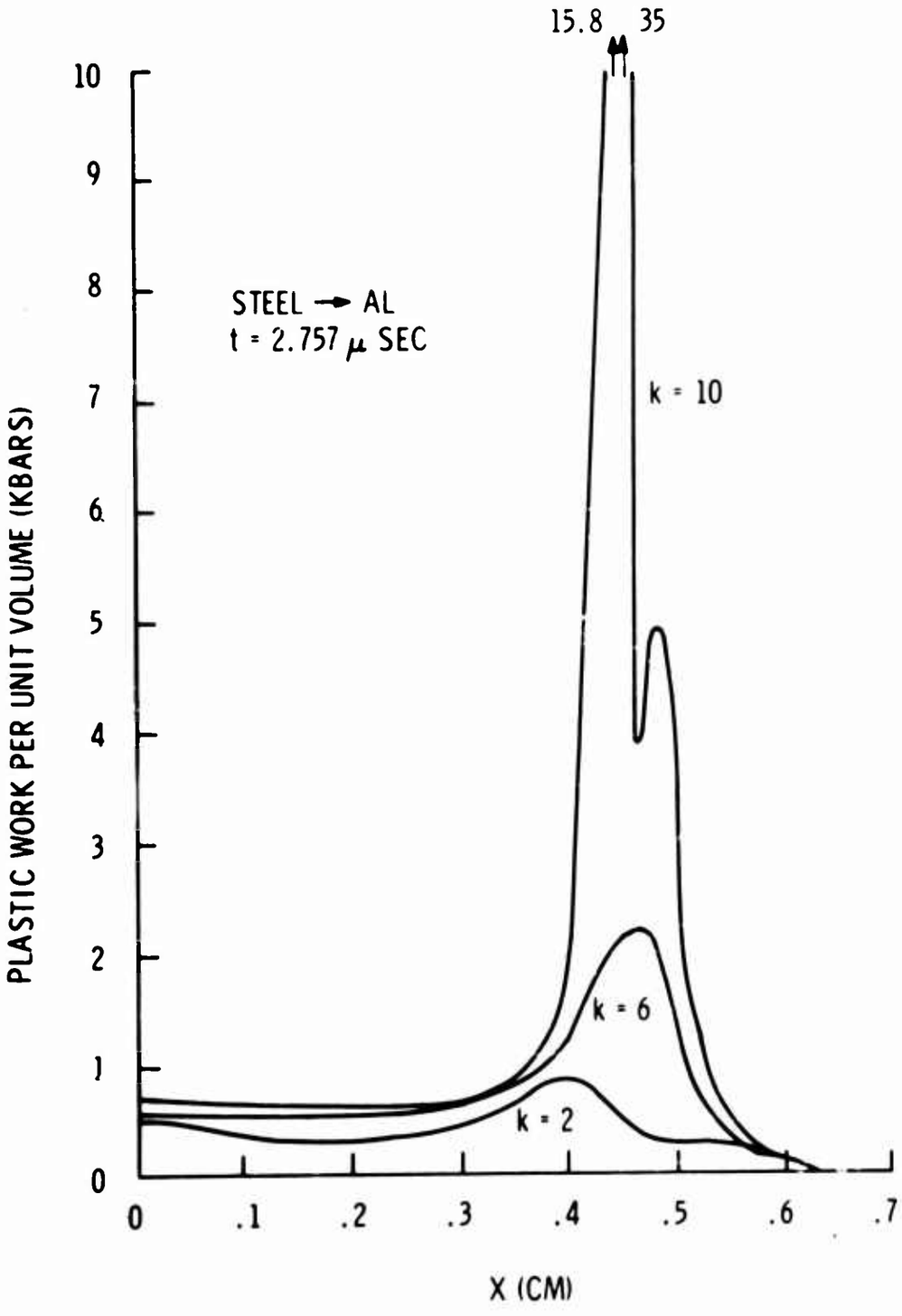

Figure 44. Plots of Plastic Work Versus Radial Distance for Problem III-A. The Time is 2.757 μ sec and the k-values of 2, 6 and 10 refer Respectively to the Free Surface, the Center Plane and the Impact Surface of the Plate

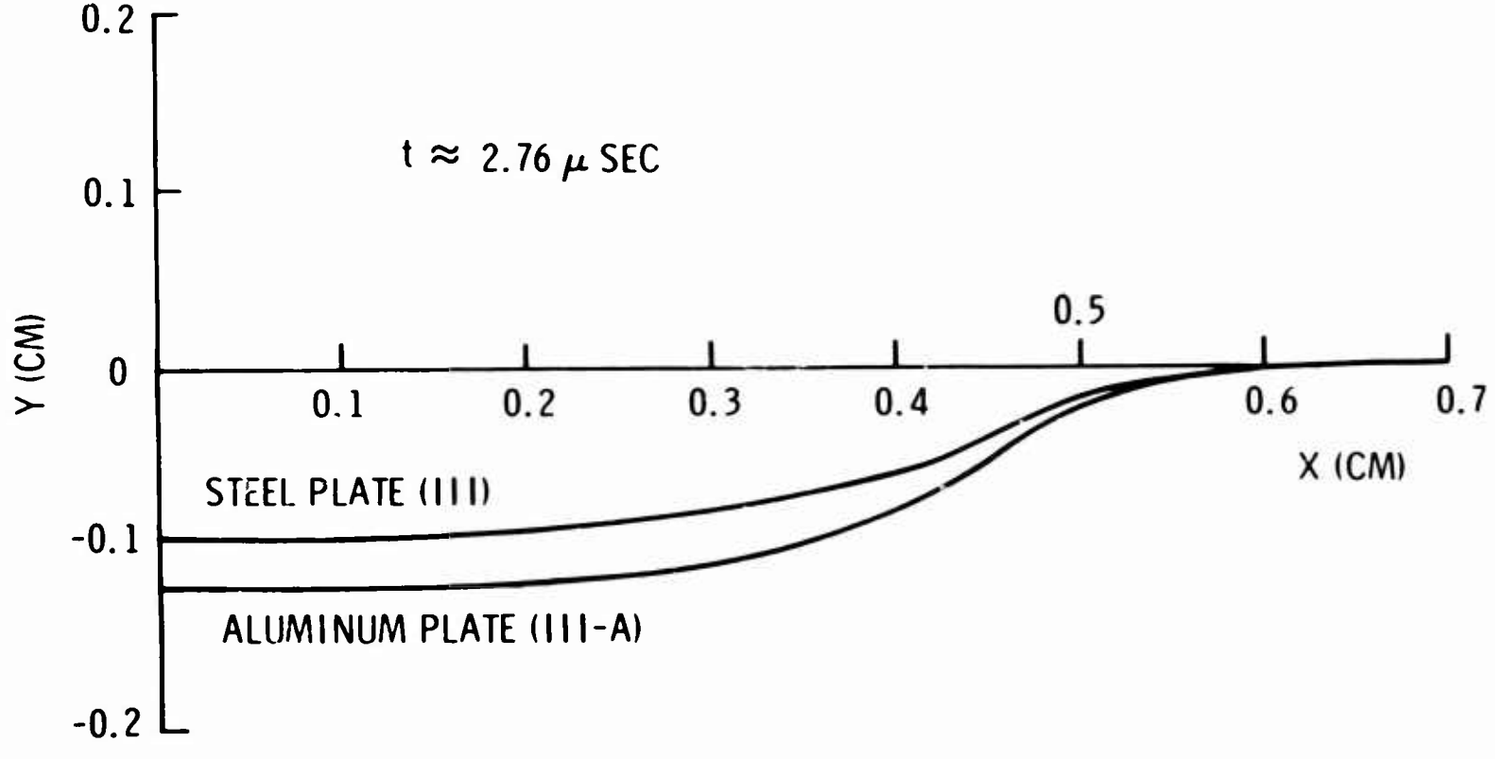

Figure 45. Free Surface Traces of the Plates of Problems III and III-A at 2.757 μsec

The details of the experimental program for duplicating Problem III-A (steel into aluminum) are contained in a report by R. Recht [28]. Some of the results are shown in Appendix VI. Cylinders of 4130 steel, 325 BHN were impacted normally against 2024-T3 aluminum sheets of 0.16 cm thickness at nominal velocities of 0.61 km/sec. The length to diameter ratio for the projectiles were approximately equal to unity. Both plan and elevation view flash radiographs were taken for each test in order to measure impact and residual velocities. Figures VI-1 and VI-2 of Appendix VI show sample radiographs for Test No. 75. The projectile path is from right to left. The plate plug can be clearly seen in these radiographs and its dished nature due to plastic deformation is evident.

The experimental results are given in Table VI-1 and Figure VI-3. In Table VI-1 the measured impact velocities, cylinder and plate plug residual velocities and angle of incidence are given for each shot. In Figure VI-3 residual velocity is plotted versus impact velocity. The dashed line represents the curve predicted by the DRI equation. It is noted that the plate plug velocity is greater than the residual velocity of the projectile. This is due to elastic release after the plug has been sheared through.

The impacted cylinders, plate plugs and perforated plates were received from DRI and are shown in the photographs of Figures VI-4 through E-6. The cylinders have been deformed as expected, having a greater radius at their impacted ends. The plugs were sheared out in one piece and remained in a dished configuration because of plastic deformation. The fractured plugs shown in Figure VI-4 were caused by secondary impact in the collecting medium.

Figure VI-7 shows experimental plots of the ratio of target hole, plate plug head and rear of projectile diameters to the original projectile diameter versus impact velocity. The diameters of the rear of the projectiles have decreased somewhat during penetration. The heads of the

projectiles have increased somewhat as expected and have approximately the same diameters as the plate plugs. It is seen that hole size as well as diameter of projectile head and plate plug increase with impact velocity while the diameter of the rear of tne projectile is rather insensitive to velocity, at least for the cases shown here. The fact that the target hole size is considerably larger than the plug indicates that plastic deformation continues in the plate causing hole widening after perforation.

Figure 46 is a plot of the numerically calculated axial velocity plotted versus radial distance for various planes through the aluminum target at the predicted failure time for Problem III-A. The dashed lines indicate both the experimentally obtained residual velocity measurement and the value calculated by Equation (6) assuming D/d = 1. It is seen that the residual velocity predicted by the CRAM code solution is in good agreement with the theory of Recht and Ipson as well as with experimental results.

Figure 47 is a trace of the numerically predicted final projectile-plug configuration at t = 2.757 μsec. The plug periphery was determined as before by connecting the cells which were subjected to the maximum shearing stresses. Also, indicated in Figure 47 are the actual measured variations of projectile head and plate hole radii for the specimens shown in Appendix VI.

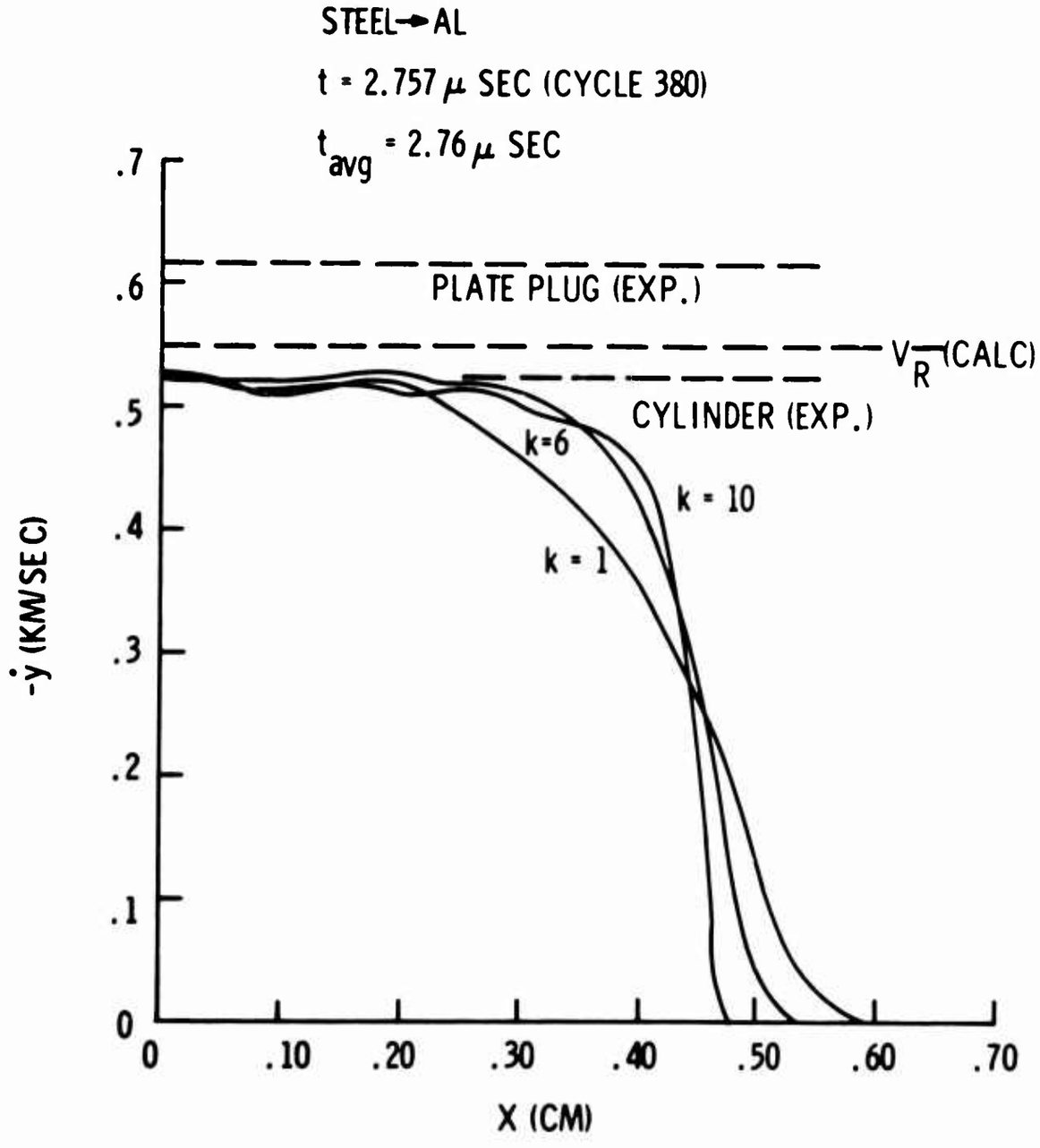

Figure 46. A Plot of Axial Velocity Versus Radial Distance for the Plate of Problem III-A. The Time is 2.757 μsec and the k-values of 1, 6, and 10 Refer Respectively to the Free Surface, the Center Plane and the Impact Surface

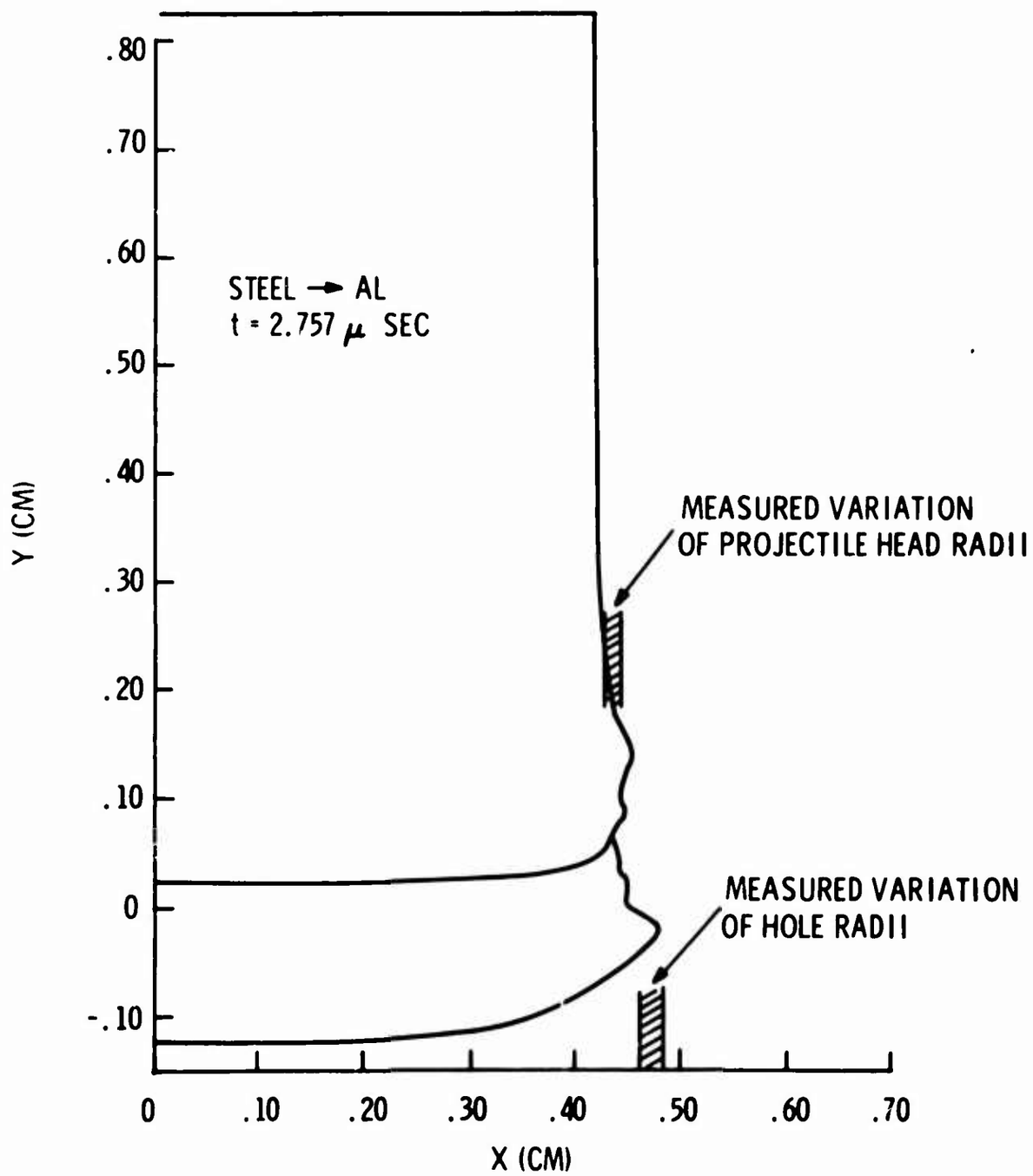

Figure 47. The Final Predicted Projectile-Plug Configuration for Problem III-A

SECTION VIII

CONCLUSIONS

Present penetration formulas governing the ballistic range of velocities are either empirical in nature or are based upon over-simplified models. The insight necessary for developing formulas of a more predictive rather than descriptive nature is obtainable through parametric studies based upon numerical solutions describing the hydrodynamic and elastic-plastic material flow. Such solutions are made available through the use of large scale computer codes such as CRAM.

A computer impact solution must in addition predict the failure mode and describe the residual state. In the absence of a generalized failure criterion special failure criteria must be employed for predicting the onset of the various delineated failure modes. Of these the most important are maximum axial tensile stress for predicting spallation, maximum circumferential stress for predicting petalling and maximum shear beneath the projectile periphery for predicting plugging type failure.

There are several methods for describing post-failure material behavior. It is possible to end the numerical solution at the time of predicted failure and predict post failure behavior on the basis of the dynamic state at the time of failure. It is also possible to artificially describe post failure behavior by continuing the numerical solution with the proper stress and strain alterations in the region of failure. Certain cases exist in which the failed regions can be handled simply by modifying the equation of state. Finally it should be possible to allow voids in the computational mesh. These various possible methods for handling post failure material behavior are listed in increasing orders of difficulty and the first method was employed for the two solutions described in this report.

A complete solution of a steel cylinder impacting a plate of like material is presented. In the initial stages of impact the numerically

predicted stress wave propagation and reflections are in good agreement with one dimensional calculations. By looking at the distribution of shear stress, generalized plastic strain and plastic work as well as the deformation pattern, it became obvious that the failure mode for this problem is plugging so the failure criterion to be used is one of maximum shear. Failure was predicted to occur when the maximum shear stress developed near the impact surface of the plate attained the same value throughout the plate thickness. This occurred at time t = 3.032 μ sec and the stress value was approximately 3 kbars. The residual velocity according to the theory of Recht and Ipson was found to be 0.382 km/sec. This value agreed quite well with velocities attained throughout the portion of the plate beneath the projectile at the predicted time of failure. By assuming that failure occurred along the planes of maximum shear the actual plug shape was predicted. From this the total residual energy of the plate-plug projectile configuration was determined to be 3.1×10^9 ergs. This accounts for 47.4% of the total energy and it was assumed that much of the remaining energy was contained in either the projectile or plug as internal energy. A region of contained failure was predicted near the impact surface of the projectile and verified experimentally. In addition the final configuration of the residual mass particles agreed with measured values.

A second problem, similar in all respects to the first with the exception of target material, which was aluminum in this case, was also solved using CRAM. Plugging failure was predicted to occur at a time of 2.76 μsec. The residual velocity of 0.549 km/sec calculated by the theory of Recht and Ipson was in good agreement with the numerically calculated velocities throughout the plate material in the region beneath the projectile. Plate bending was slightly more significant for the aluminum target than for the steel; however, tensile stresses at the rear

surface were significantly less than values necessary for failure while, at comparable times, the shear stresses developed beneath the projectile periphery were approaching critical values.

An experimental program was set up by R. Recht at the Denver Research Institute for duplicating the steel-aluminum impact problem. Plugging failure was observed and the plate plugs were dish shaped due to bending. The observed residual particle masses and velocities were in good agreement with theory; however, the projectile and plate plug did not remain in contact after fracture because of elastic recovery.

The results of this study indicate that, not only are large computer codes such as CRAM able to predict material flow produced by ballistic impact, but that they provide much more information suitable for performing parametric impact studies and developing penetration formulas than any other presently known method, either theoretical or experimental.

APPENDIX I

BASIC EQUATIONS IN THE CRAM CODE

The Lagrangian form of the equations of motion for axial symmetric and planar symmetric situations are:

$$\frac{\partial \Sigma_{xx}}{\partial x} + \frac{\partial T_{xy}}{\partial y} + \frac{T_{xy}}{y}\Bigg|^{*} = \rho \ddot{x}; \quad \frac{\partial T_{xy}}{\partial x} + \frac{\partial \Sigma_{yy}}{\partial y} + \frac{\Sigma_{xx} - \Sigma_{\theta\theta}}{y}\Bigg|^{*} = \rho \ddot{y} \qquad \text{(I-1)}$$

where: $\Sigma_{xx} = -(p+q) + S_{xx}$, $\Sigma_{yy} = -(p+q) + S_{yy}$

$\Sigma_{\theta\theta} = -(p+q) + S_{\theta\theta}$

Note: the terms marked $\Big|^{*}$ are set equal to zero for planar symmetric problems.

Continuity Equation

$$\frac{\dot{V}}{V} = \frac{\partial \dot{x}}{\partial x} + \frac{\partial \dot{y}}{\partial y} + \frac{\dot{y}}{y}\Bigg|^{*} \qquad \text{(I-2)}$$

Strain-Rates

$$\dot{\epsilon}_{xx} = \frac{\partial \dot{x}}{\partial x}, \quad \dot{\epsilon}_{\theta\theta} = \frac{\dot{y}}{y}\Bigg|^{*}$$

$$\dot{\epsilon}_{yy} = \frac{\partial \dot{y}}{\partial y}, \quad \dot{\epsilon}_{xy} = \frac{\partial \dot{y}}{\partial x} + \frac{\partial \dot{x}}{\partial y} \qquad \text{(I-3)}$$

First Law of Thermodynamics

$$\dot{E} = -(p+q)\,\dot{V} + V\left(S_{xx}\,\dot{\epsilon}_{xx} + S_{yy}\,\dot{\epsilon}_{yy} + S_{\theta\theta}\,\dot{\epsilon}_{\theta\theta} + T_{xy}\,\dot{\epsilon}_{xy}\right) \qquad \text{(I-4)}$$

Artificial Viscosity

$$q = \frac{C_o^2\,\rho_o\left(\dot{V}/V\right)^2 A}{V} \quad \text{for } \dot{V} < o$$

$$q = o, \text{ for } \dot{V} \geq o \qquad \text{(I-5)}$$

C_o = constant ; A = area

The basic geometric element in a typical grid network is a quadrilateral of arbitrary shape. It is therefore convenient to represent the spacial partial derivatives by their integral definitions:

$$\frac{\partial F}{\partial x} = \lim_{A \to 0} \frac{\oint_C F \vec{n} \cdot \vec{i}\, dS}{A}$$

$$\frac{\partial F}{\partial y} = \lim_{A \to 0} \frac{\oint_C F \vec{n} \cdot \vec{j}\, dS}{A}$$

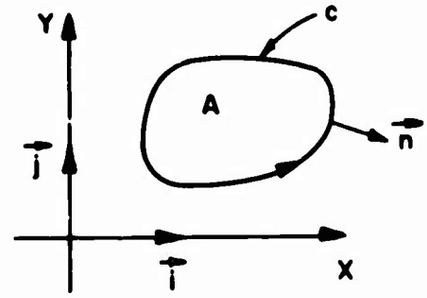

where: A = area

C = boundary of area A

S = arc length

$\vec{n}$ = unit normal vector to C

$\vec{i}$ = unit vector in X-direction

$\vec{j}$ = unit vector in Y-direction

$$\vec{n} = \frac{\partial x}{\partial n}\vec{i} + \frac{\partial y}{\partial n}\vec{j} = \frac{\partial y}{\partial S}\vec{i} - \frac{\partial x}{\partial S}\vec{j}$$

Applying the above to the quadrilateral 1, 2, 3, 4, we obtain, for F defined at the points 1, 2, 3, 4

$$\int_C F \vec{n} \cdot \vec{i}\, dS = \int_C F \frac{\partial y}{\partial S} dS = -\left[F_{23}(y_2 - y_3) + F_{34}(y_3 - y_4) + F_{41}(y_4 - y_1) + F_{12}(y_1 - y_2)\right]$$

$$F_{ij} \equiv \left(F_i + F_j\right)/2$$

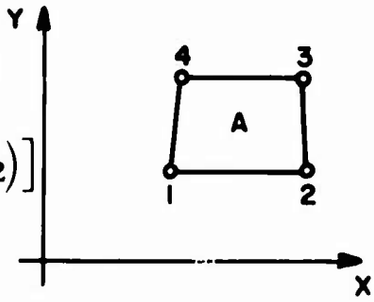

Therefore,

$$\frac{\partial F}{\partial x} = -\frac{1}{A}\left[F_{23}(y_2 - y_3) + F_{34}(y_3 - y_4) + F_{41}(y_4 - y_1) + F_{12}(y_1 - y_2)\right] \qquad \text{(I-6)}$$

$$= \frac{1}{2A}\left[(F_2 - F_4)(y_3 - y_1) - (y_2 - y_4)(F_3 - F_1)\right]$$

Similarly,

$$\frac{\partial F}{\partial y} = -\frac{1}{2A}\left[\left(F_2 - F_4\right)\left(x_3 - x_1\right) - \left(x_2 - x_4\right)\left(F_3 - F_1\right)\right] \qquad \text{(I-7)}$$

The quantities $\frac{\partial F}{\partial x}$, $\frac{\partial F}{\partial y}$, are considered to be defined at the center of the quadrilateral. For the acceleration routines used to move, say, point P, the given quantity F in Equations (A-6) and (A-7) is defined at the center of a quadrilateral. The area enclosed in the integration is the area I, II, III, IV.

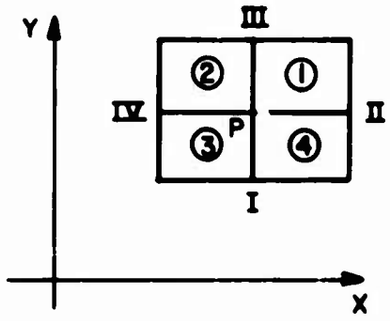

The corresponding difference equation for the x and y components of acceleration become:

$$\int_c F\,\vec{n}\cdot\vec{i}\,dS = -\left[F_{①}\left(y_{II} - y_{III}\right) + F_{②}\left(y_{III} - y_{IV}\right) + F_{③}\left(y_{IV} - y_{I}\right) + F_{④}\left(y_{I} - y_{II}\right)\right] \qquad \text{(I-8)}$$

$$\int_c F\,\vec{n}\cdot\vec{j}\,dS = F_{①}\left(x_{II} - x_{III}\right) + F_{②}\left(x_{III} - x_{IV}\right) + F_{③}\left(x_{IV} - x_{I}\right) + F_{④}\left(x_{I} - x_{II}\right) \qquad \text{(I-9)}$$

For time derivatives, a standard central differencing scheme is employed. See Appendix II for a complete list of the difference equations used.

APPENDIX II

DIFFERENCE EQUATIONS IN THE CRAM CODE

1. Mass Zoning and Indexing

The material is divided into quadrilaterals with a grid indexed j, k that distorts with the material. In the following figures, the centers and vertices of the quadrilaterals will be denoted as follows:

① = j + 1/2, k + 1/2 1 = j, k

② = j - 1/2, k + 1/2 2 = j + 1, k

③ = j - 1/2, k - 1/2 3 = j + 1, k + 1

④ = j + 1/2, k - 1/2 4 = j, k + 1

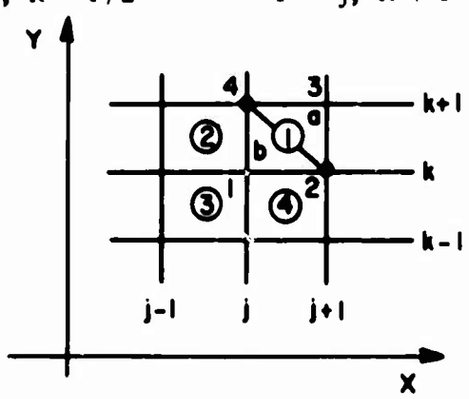

The mass at zero time associated with each quadrilateral is obtained by using the well-known theorem of Pappus for determining the volumes swept out by the quadrilateral cross-sections rotated about the y-axis. For example, the mass at zero time for quadrilateral ① is calculated as follows:

(a)

$$M_{①} = \frac{1}{3}\left(\frac{\rho^o}{V^o}\right)_{①} \left[\left(y_2^o + y_3^o + y_4^o\right) A_a^o + \left(y_1^o + y_2^o + y_4^o\right) A_b^o\right]_{①} \quad \text{(II-1)}$$

masses M_2, M_3 and e calculated similarly.

A_a = area of triangle "a"

A_b = area of triangle "b"

(b)

$$\left(A_a\right)_{①}^{n} = \frac{1}{2}\left[x_2^n\left(y_3^n - y_4^n\right) + x_3^n\left(y_4^n - y_2^n\right) + x_4^n\left(y_2^n - y_3^n\right)\right] \quad \text{(II-2)}$$

$$\left(A_b\right)_{①}^{n} = \frac{1}{2}\left[x_2^n\left(y_4^n - y_1^n\right) + x_4^n\left(y_1^n - y_2^n\right) + x_1^n\left(y_2^n - y_4^n\right)\right] \qquad \text{(II-3)}$$

$$A_{①}^{n} = \left(A_a\right)_{①}^{n} + \left(A_b\right)_{①}^{n}$$

2. Continuity Equation

$$V_{①}^{n} = \frac{1}{3}\left(\frac{\rho^o}{M}\right)_{①}\left[\left(y_2^n + y_3^n + y_4^n\right)A_a^n + \left(y_1^n + y_2^n + y_4^n\right)A_b^n\right]_{①}$$

$$V_{①}^{n} = \left(\frac{\rho^o}{\rho^n}\right)_{①} \qquad \text{(II-4)}$$

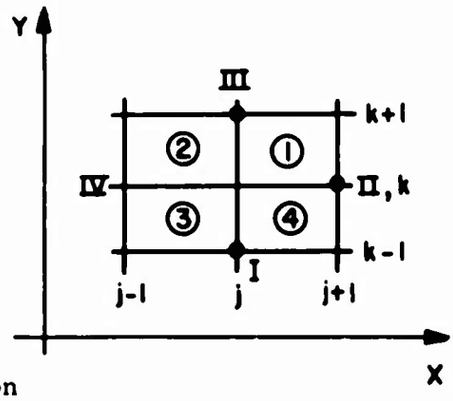

3. Equations of Motion

(a)

$$\dot{x}_{j,k}^{n+1/2} = \dot{x}_{j,k}^{n-1/2} - \frac{\Delta t^n}{2\rho_{j,k}^n}\left[\left(\Sigma_{xx}\right)_{①}^{n}\left(y_{II}^n - y_{III}^n\right)\right.$$

$$+ \left(\Sigma_{xx}\right)_{②}^{n}\left(y_{III}^n - y_{IV}^n\right) + \left(\Sigma_{xx}\right)_{③}^{n}\left(y_{IV}^n - y_I^n\right)$$

$$+ \left(\Sigma_{xx}\right)_{④}^{n}\left(y_I^n - y_{II}^n\right) - \left(T_{xy}\right)_{①}^{n}\left(x_{II}^n - x_{III}^n\right) \qquad \text{(II-5)}$$

$$- \left(T_{xy}\right)_{②}^{n}\left(x_{III}^n - x_{IV}^n\right) - \left(T_{xy}\right)_{③}^{n}\left(x_{IV}^n - x_I^n\right)$$

$$\left. - \left(T_{xy}\right)_{④}^{n}\left(x_I^n - x_{II}^n\right)\right] + \Delta t^n \beta_{j,k}^n$$

(b)

$$\dot{y}^{n+1/2}_{j,k} = \dot{y}^{n-1/2}_{j,k} + \frac{\Delta t^n}{2\varphi^n_{j,k}} \left[(\Sigma_{yy})^n_{①} (x^n_{II} - x^n_{III}) \right.$$

$$+ (\Sigma_{yy})^n_{②} (x^n_{III} - x^n_{IV}) + (\Sigma_{yy})^n_{③} (x^n_{IV} - x^n_{I})$$

$$+ (\Sigma_{yy})^n_{④} (x^n_{I} - x^n_{II}) - (T_{xy})^n_{①} (y^n_{II} - y^n_{III})$$

$$- (T_{xy})^n_{②} (y^n_{III} - y^n_{IV}) - (T_{xy})^n_{③} (y^n_{IV} - y^n_{I})$$

$$\left. - (T_{xy})^n_4 (y^n_{I} - y^n_{II}) \right] + \Delta t^n \alpha^n_{j,k} \qquad \text{(II-6)}$$

(c)

$$\varphi^n_{j,k} = \frac{1}{4}\left[\left(\frac{\rho^o A^n}{V^n}\right)_{①} + \left(\frac{\rho^o A^n}{V^n}\right)_{②} + \left(\frac{\rho^o A^n}{V^n}\right)_{③} + \left(\frac{\rho^o A^n}{V^n}\right)_{④} \right]$$

$$\alpha^n_{j,k} = \frac{1}{4}\left\{ \left[T^n_{xy} \left(\frac{A^n}{M}\right) \right]_{①} + \left[T^n_{xy} \left(\frac{A^n}{M}\right) \right]_{②} + \left[T^n_{xy} \left(\frac{A^n}{M}\right) \right]_{③} \right.$$

$$\left. + \left[T^n_{xy} \left(\frac{A^n}{M}\right) \right]_{④} \right\} \qquad \text{(II-7)}$$

$$\beta^n_{j,k} = \frac{1}{4}\left\{ \left[(\Sigma^n_{yy} - \Sigma^n_{\theta\theta}) \left(\frac{A^n}{M}\right) \right]_{①} + \left[(\Sigma^n_{yy} - \Sigma^n_{\theta\theta}) \left(\frac{A^n}{M}\right) \right]_{②} \right.$$

$$\left. + \left[(\Sigma^n_{yy} - \Sigma^n_{\theta\theta}) \left(\frac{A^n}{M}\right) \right]_{③} + \left[(\Sigma^n_{yy} - \Sigma^n_{\theta\theta}) \left(\frac{A^n}{M}\right) \right]_{④} \right\}$$

(d)

$$x^{n+1}_{j,k} = x^n_{j,k} + \dot{x}^{n+1/2}_{j,k} \Delta t^{n+1/2}$$

$$y^{n+1}_{j,k} = y^n_{j,k} + \dot{y}^{n+1/2}_{j,k} \Delta t^{n+1/2} \qquad \text{(II-8)}$$

4. Stress-Strain Relations

(a) Strains

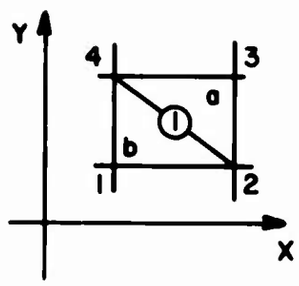

$$A_{①} = (A_a)_{①} + (A_b)_{①}$$

$$A_{①}^{n+1/2} = \frac{1}{2}\left(A_{①}^{n+1} + A_{①}^{n}\right)$$

$$V_{①}^{n+1/2} = \frac{1}{2}\left(V_{①}^{n+1} + V_{①}^{n}\right)$$

$$\left(\dot{\epsilon}_{xx}\right)_{①}^{n+1/2} = \left(\frac{\partial \dot{x}}{\partial x}\right)_{①}^{n+1/2} = \frac{1}{2A_{①}^{n+1/2}}\left[\left(\dot{x}_2 - \dot{x}_3\right)\left(y_3 - y_1\right) - \left(y_2 - y_4\right)\left(\dot{x}_3 - \dot{x}_1\right)\right]^{n+1/2}$$

$$\left(\dot{\epsilon}_{yy}\right)_{①}^{n+1/2} = \left(\frac{\partial \dot{y}}{\partial y}\right)_{①}^{n+1/2} = \frac{-1}{2A_{①}^{n+1/2}}\left[\left(\dot{y}_2 - \dot{y}_4\right)\left(x_3 - x_4\right) - \left(x_2 - x_4\right)\left(\dot{y}_3 - \dot{y}_1\right)\right]^{n+1/2} \qquad \text{(II-9)}$$

$$\left(\dot{\epsilon}_{\theta\theta}\right)_{①}^{n+1/2} = \left(\frac{\dot{y}}{y}\right)_{①}^{n+1/2} = \left[\frac{\dot{V}}{V} - \left(\dot{\epsilon}_{xx} + \dot{\epsilon}_{yy}\right)\right]_{①}^{n+1/2}$$

$$\left(\dot{\epsilon}_{xy}\right)_{①}^{n+1/2} = \left(\frac{\partial \dot{y}}{\partial x} + \frac{\partial \dot{x}}{\partial y}\right) = \frac{1}{2A_{①}^{n+1/2}}\left\{\left[\left(\dot{y}_2 - \dot{y}_4\right)\left(y_3 - y_1\right) - \left(y_2 - y_4\right)\left(\dot{y}_3 - \dot{y}_1\right)\right] - \left[\left(\dot{x}_2 - \dot{x}_4\right)\left(x_3 - x_1\right) - \left(x_2 - x_4\right)\left(\dot{x}_3 - \dot{x}_1\right)\right]\right\}^{n+1/2}$$

$$
\begin{aligned}
(\Delta\epsilon_{xx})^{n+1/2}_{①} &= (\dot{\epsilon}_{xx})^{n+1/2}_{①}\ \Delta t^{n+1/2} \\
(\Delta\epsilon_{yy})^{n+1/2}_{①} &= (\dot{\epsilon}_{yy})^{n+1/2}_{①}\ \Delta t^{n+1/2} \\
(\Delta\epsilon_{\theta\theta})^{n+1/2}_{①} &= (\dot{\epsilon}_{\theta\theta})^{n+1/2}_{①}\ \Delta t^{n+1/2} \\
(\Delta\epsilon_{xy})^{n+1/2}_{①} &= (\dot{\epsilon}_{xy})^{n+1/2}_{①}\ \Delta t^{n+1/2}
\end{aligned}
\qquad \text{(II-10)}
$$

$$
\left(\frac{\Delta V}{V}\right)^{n+1/2}_{①} = \left(\frac{\dot{V}^{n+1/2}}{V^{n+1/2}_{①}}\right)_{①} \Delta t^{n+1/2} = \frac{V_1^{n+1} - V_1^{n}}{V^{n+1/2}_{①}} \qquad \text{(II-11)}
$$

(b) Stress Deviators

$$
\begin{aligned}
(S_{xx})^{n+1}_{①} &= (S_{xx})^{n}_{①} + 2\mu \left[\Delta\epsilon_{xx}^{n+1/2} - \frac{1}{3}\left(\frac{\Delta V}{V}\right)^{n+1/2}\right]_{①} + (\delta_{xx})^{n}_{①} \\
(S_{yy})^{n+1}_{①} &= (S_{yy})^{n}_{①} + 2\mu \left[\Delta\epsilon_{yy}^{n+1/2} - \frac{1}{3}\left(\frac{\Delta V}{V}\right)^{n+1/2}\right]_{①} + (\delta_{yy})^{n}_{①} \\
(S_{\theta\theta})^{n+1}_{①} &= (S_{\theta\theta})^{n}_{①} + 2\mu \left[\Delta\epsilon_{\theta\theta}^{n+1/2} - \frac{1}{3}\left(\frac{\Delta V}{V}\right)^{n+1/2}\right]_{①}
\end{aligned}
$$

$$
(T_{xy})^{n+1}_{①} = (T_{xy})^{n}_{①} + \mu \left[\Delta\epsilon_{xy}^{n+1/2}\right] + (\delta_{xy})^{n}_{①} \qquad \text{(II-12)}
$$

5. Equation of State

$$
p^{n+1}_{①} = A(V^{n+1}_{①}) + B(V^{n+1}_{①}) \cdot E^{n+1}_{①} \qquad \text{(II-13)}
$$

5. Artificial Viscosity

$$
q^{n+1/2}_{①} = \left[\frac{c_o^{\,2}\,\rho^{\,o} A^{n+1/2}}{V^{n+1/2}} \left(\frac{\dot{V}}{V}\right)^{2}\right]_{①} \qquad \text{(II-14)}
$$

$c_o^{\,2} = 4$, calculate for $\dot{V} < 0$

7. Total Stress

$$(\Sigma_{xx})^{n+1}_{①} = (S_{xx})^{n+1}_{①} - \left[p^{n+1} + q^{n+1/2} \right]_{①}$$

$$(\Sigma_{yy})^{n+1}_{①} = (S_{yy})^{n+1}_{①} - \left[p^{n+1} + q^{n+1/2} \right]_{①} \qquad \text{(II-15)}$$

$$(\Sigma_{\theta\theta})^{n+1}_{①} = (S_{\theta\theta})^{n+1}_{①} - \left[p^{n+1} + q^{n+1/2} \right]_{①}$$

8. Energy Equations

(a) First Law of Thermodynamics

$$E^{n+1}_{①} = \left\{ \frac{E^n - \left\{ \frac{1}{2} \left[A(V^{n+1}) + p^n \right] + q^{n+1/2} \right\} \cdot (V^{n+1} - V^n) + \Delta Z^{n+1/2}}{1 + \frac{1}{2} \left[B(V^{n+1}) \right] \quad (V^{n+1} - V^n)} \right\}$$

(II-16)

(b) Energy Dissipation or Energy of Distortion

$$Z^{n+1}_{①} = Z^n_{①} + V^{n+1/2}_{①} \left\{ S_{xx} \epsilon_{xx} + S_{yy} \epsilon_{yy} + S_{\theta\theta} \epsilon_{\theta\theta} + T_{xy} \epsilon_{xy} \right\}^{n+1/2}_{①}$$

(II-17)

$$\Delta Z^{n+1/2} = Z^{n+1} - Z^n; \quad S^{n+1/2}_{ij} = \frac{1}{2} (S^{n+1}_{ij} + S^n_{ij})$$

9. Von Mises Yield Criterion

$$2J^{n+1} = \left[(S_1^{n+1})^2 + (S_2^{n+1})^2 + (S_3^{n+1})^2 \right]$$

$$= \left[(S_{xx}^{n+1})^2 + (S_{yy}^{n+1})^2 + (S_{\theta\theta}^{n+1})^2 \right] + 2(T_{xy}^{n+1})^2 \qquad \text{(II-18)}$$

$$2J^{n+1} - \frac{2}{3}(Y_o)^2 = k^{n+1}$$

If $k^{n+1} > 0$, then multiply each of the stresses S_{xx}^{n+1}, $S_{\theta\theta}^{n+1}$, S_{yy}^{n+1} and T_{xy}^{n+1} by $\sqrt{\frac{2}{3}}\ Y_o / \sqrt{2J^{n+1}}$. If $k^{n+1} \leq 0$, use the stresses as computed by Hooke's law.

APPENDIX III

SC 4020 PLOTS OF THE LAGRANGIAN GRID FOR PROBLEM III

The following grid plots show the predicted deformation of the projectile-target configuration at various times during the impact process. The choice of the grid depends on several factors including the geometrical configuration, degree of resolution desired and computing time. A rectangular grid is best suited for cylindrical projectile impact. To obtain the desired resolution and stress wave definition through a given region, a miminum of ten zones in the direction of propagation is required. In both Problems III and III-A, this requirement created relatively small zones in the targets which were thin in comparison to the projectile length. In the interest of computing economy (10^{-4} min/cycle/cell on IBM 7094) a larger cell size was used for the projectile. This variation in grid size did not adversely affect the results and agreement with both one-dimensional wave propagation calculations and experimental evidence was good.

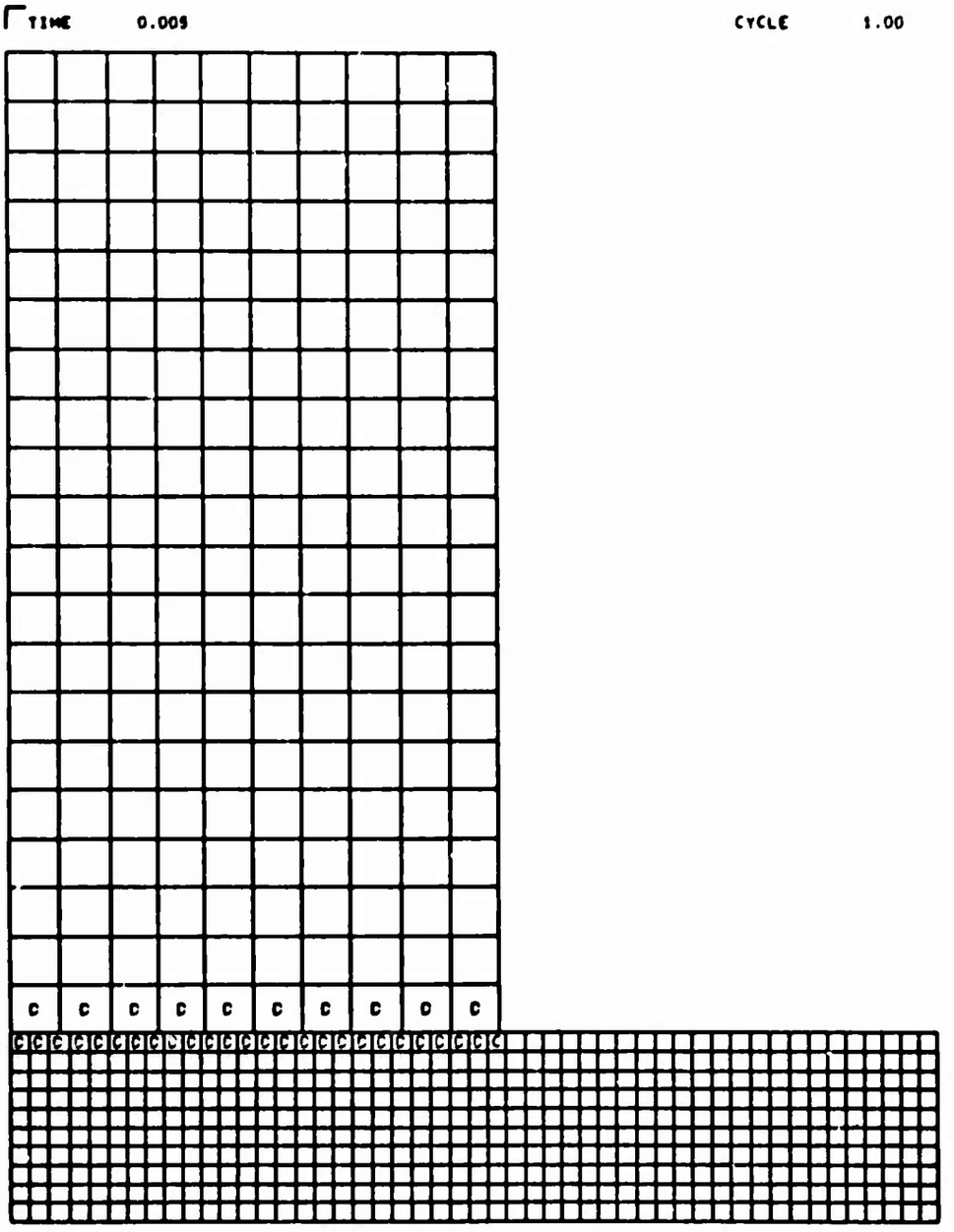

Figure III-1. Problem III, t = 0.00' μsec.

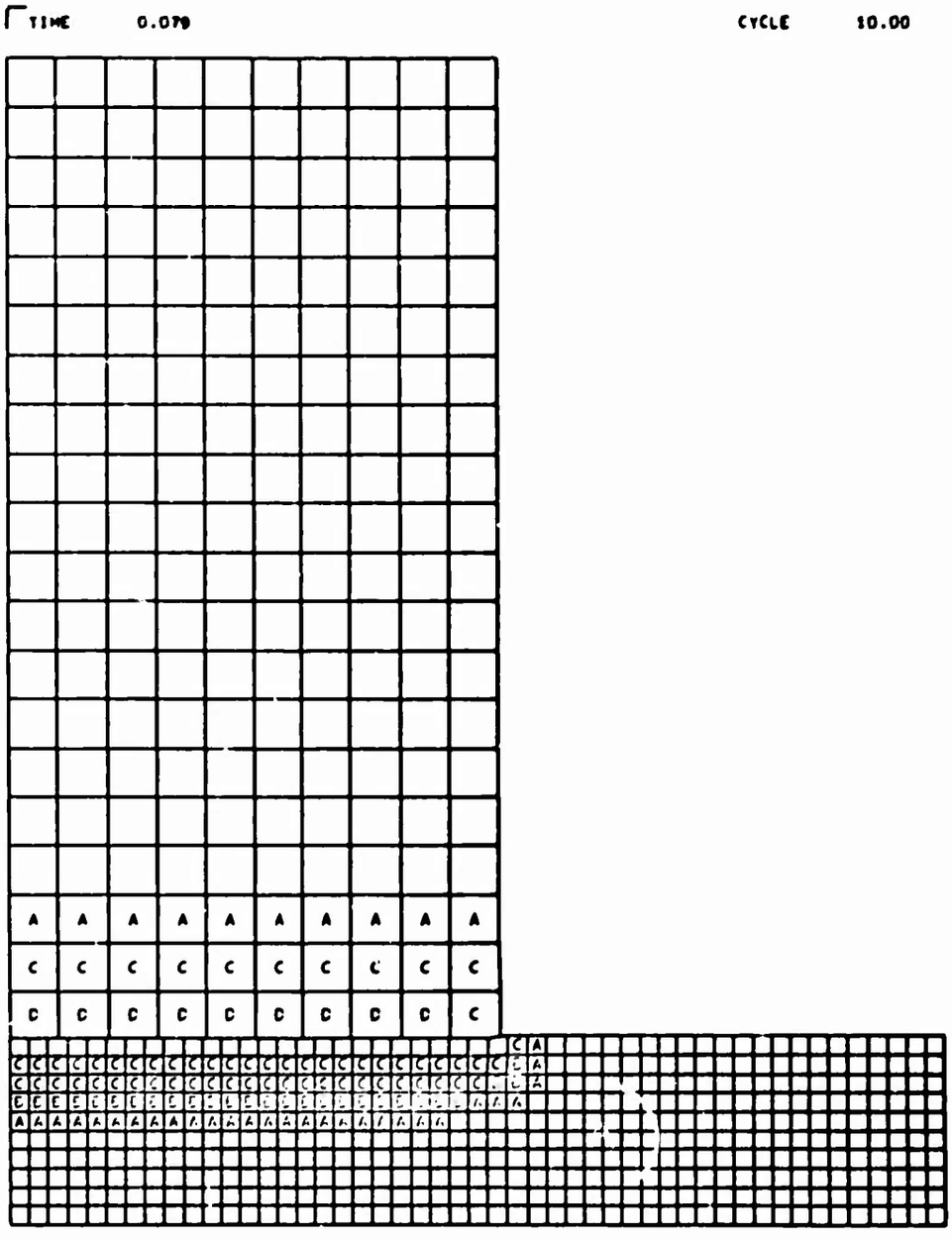

Figure III-2. Problem III. t = 0.079μsec.

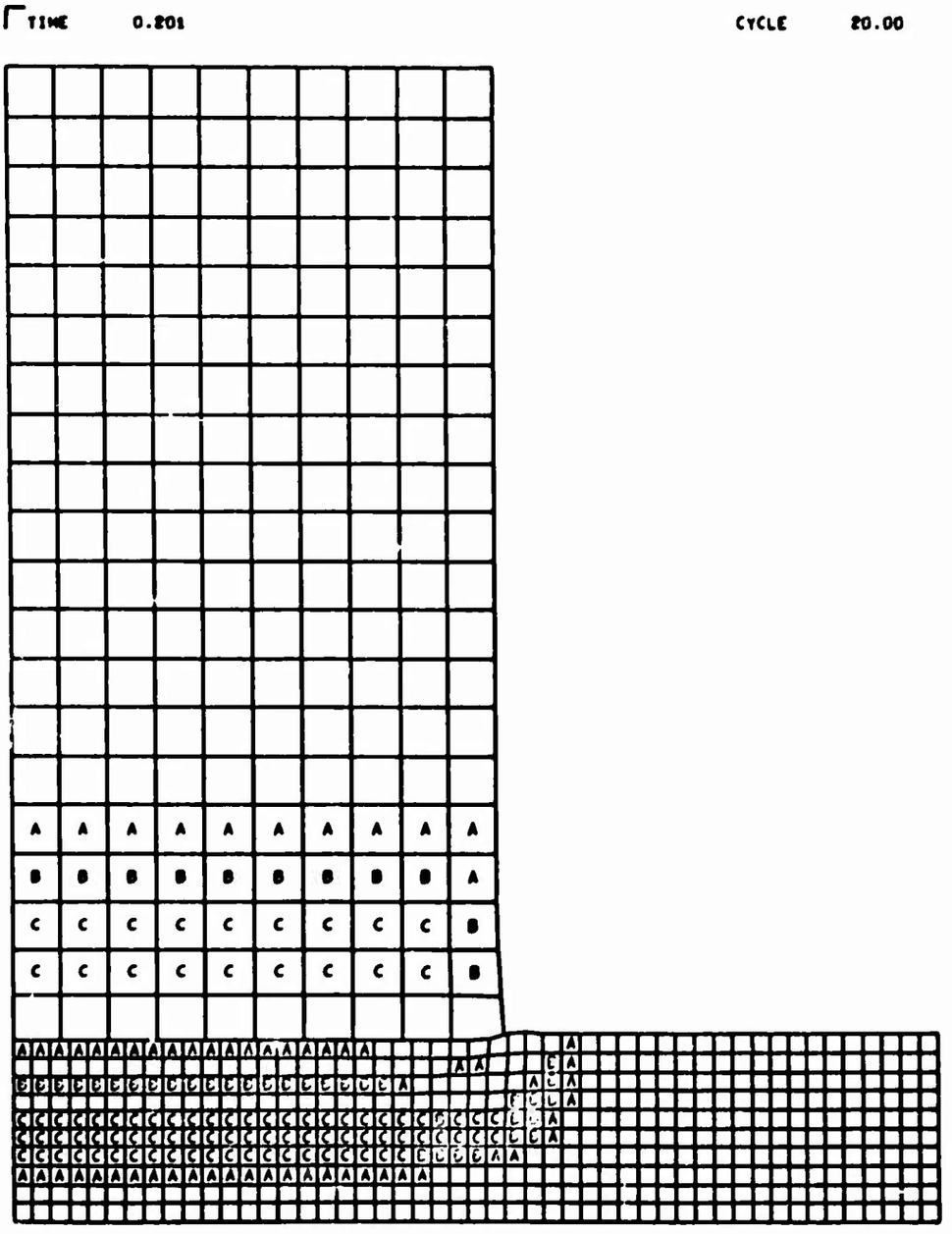

Figure III-3. Problem III, t = 0.201 μ sec

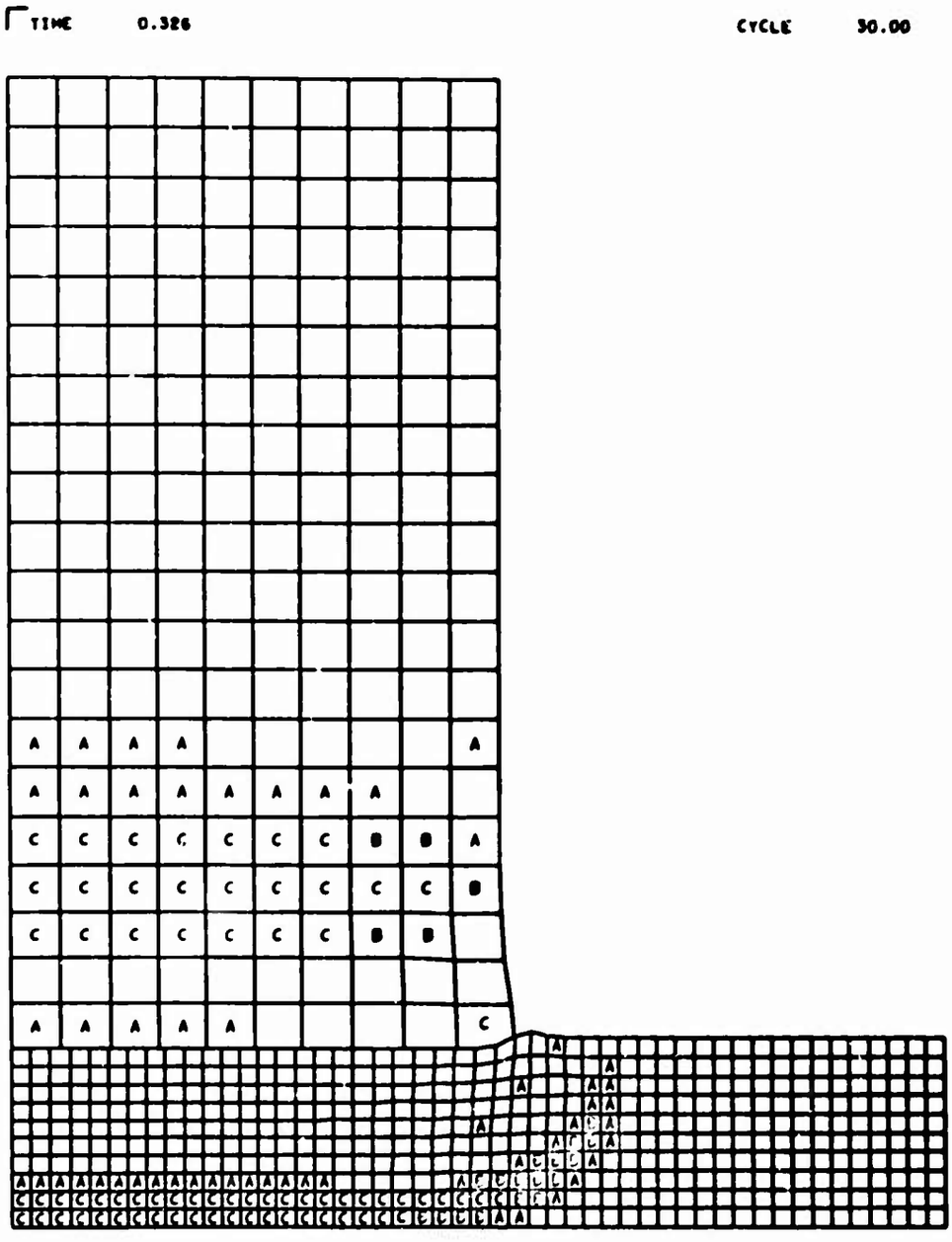

Figure III-4. Problem III, t = 0.326 μsec.

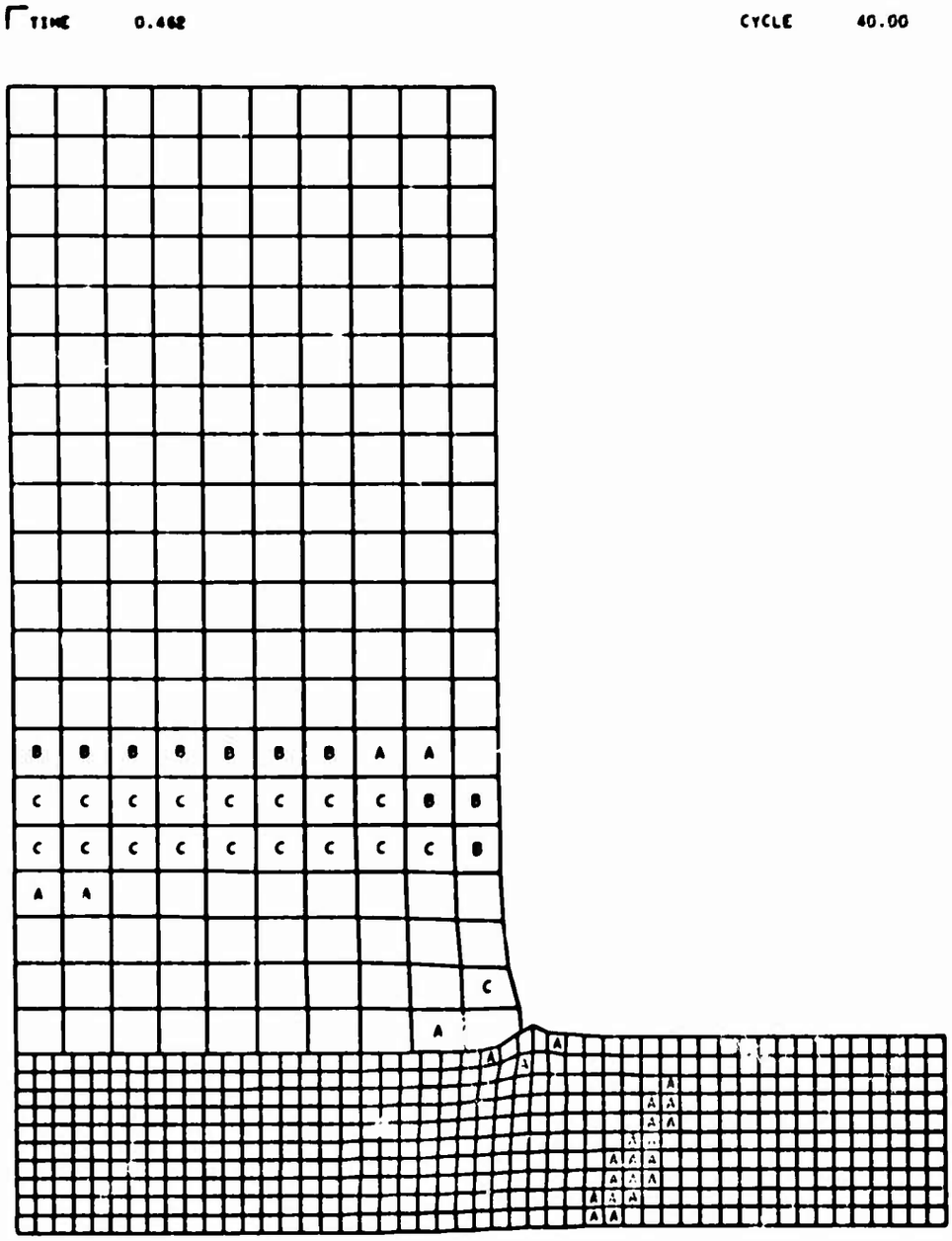

Figure III-5. Problem III, t = 0.462 μsec

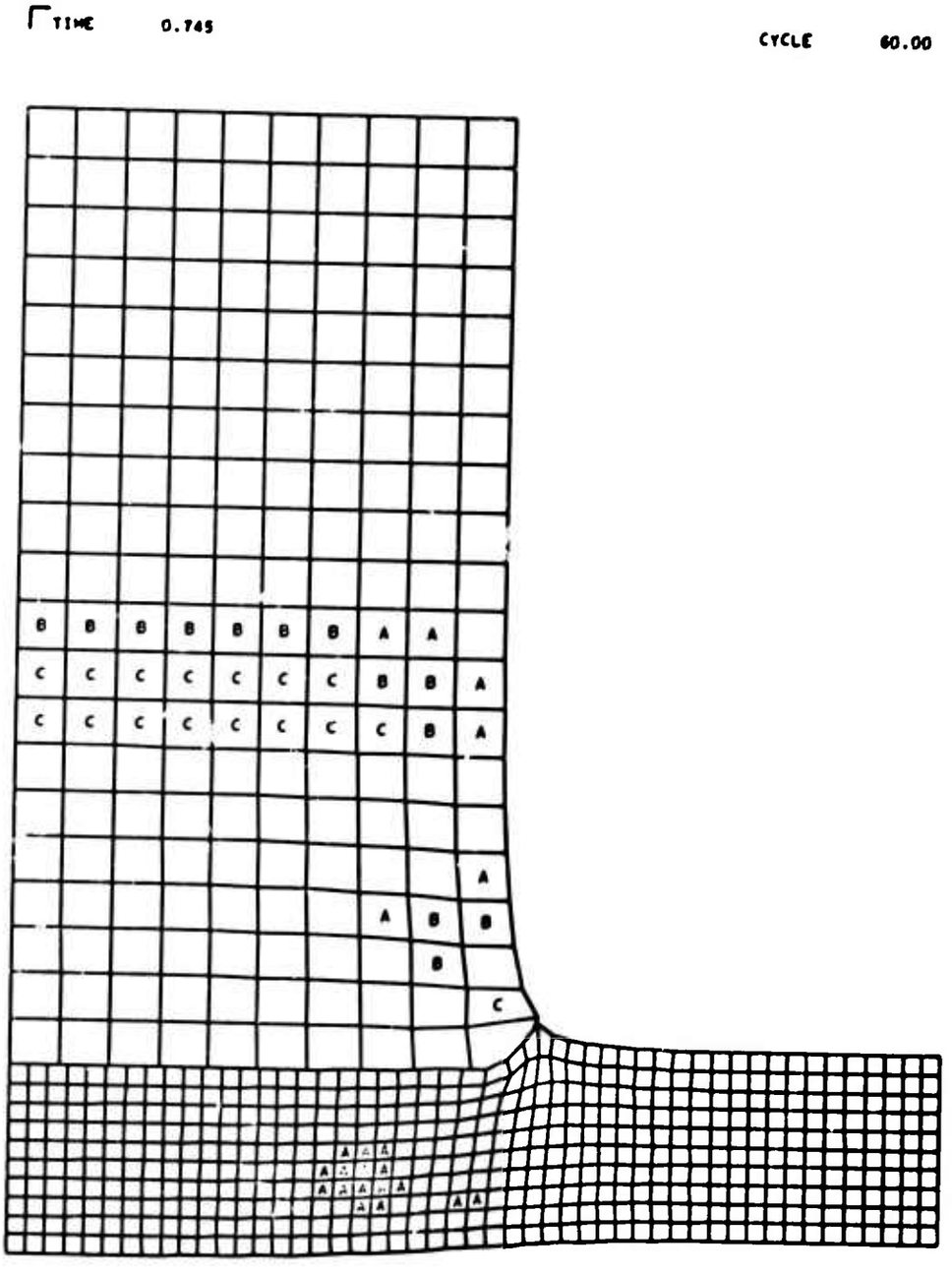

Figure III-6. Problem III, t = 0.745 μsec.

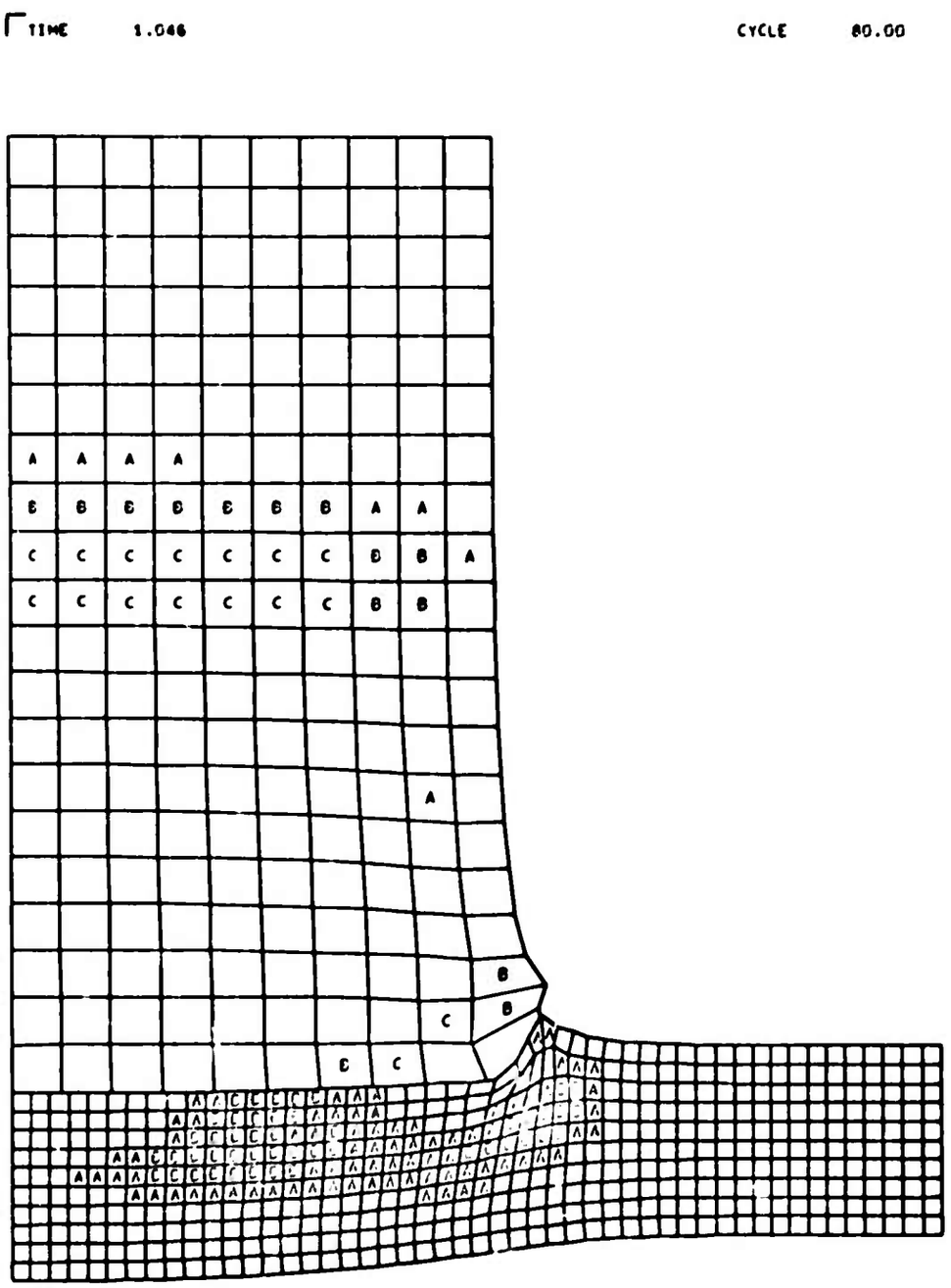

Figure III-7. Problem III, t = 1.046 μsec.

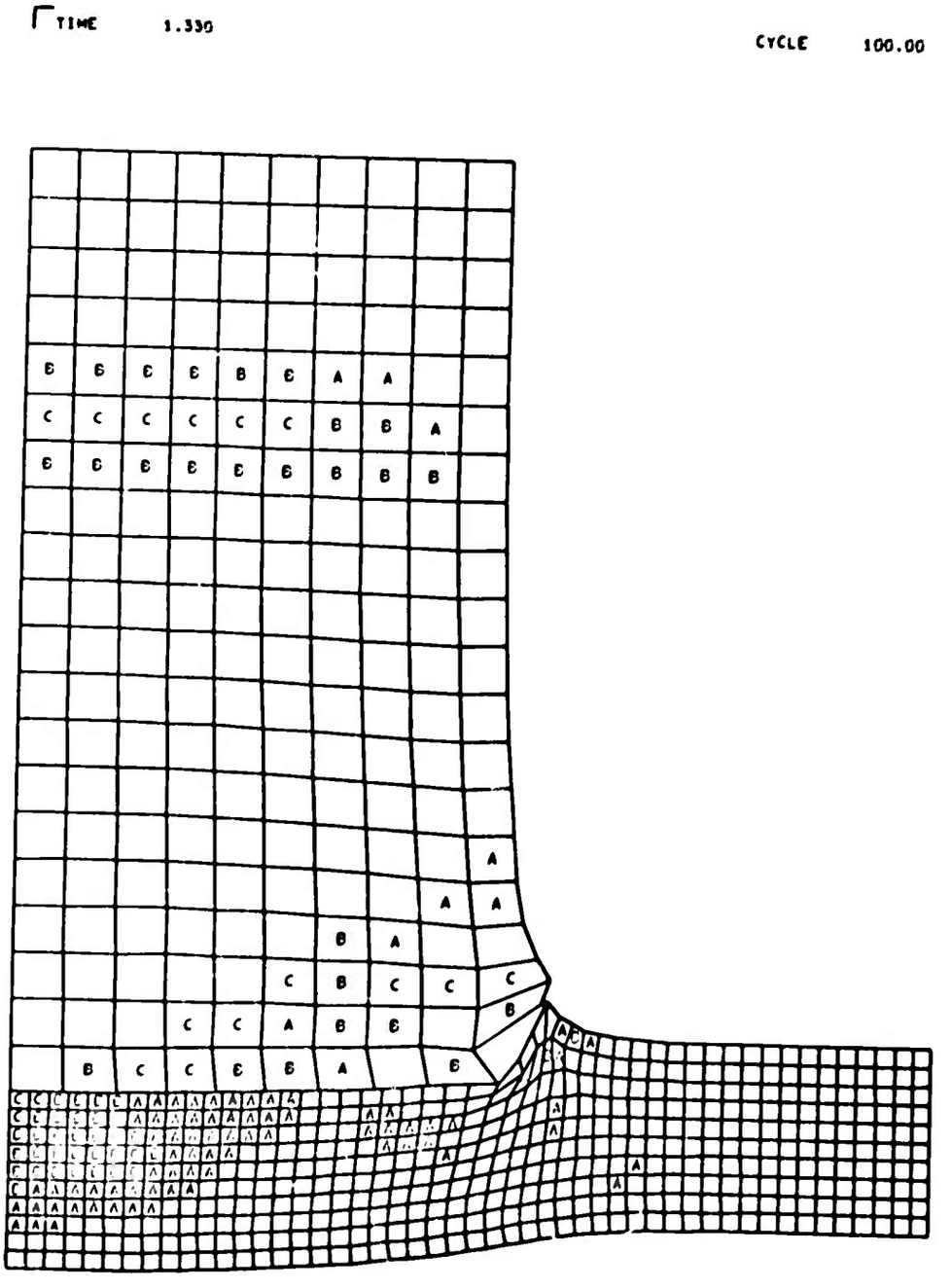

Figure III-8. Problem III, t = 1.330 μ sec.

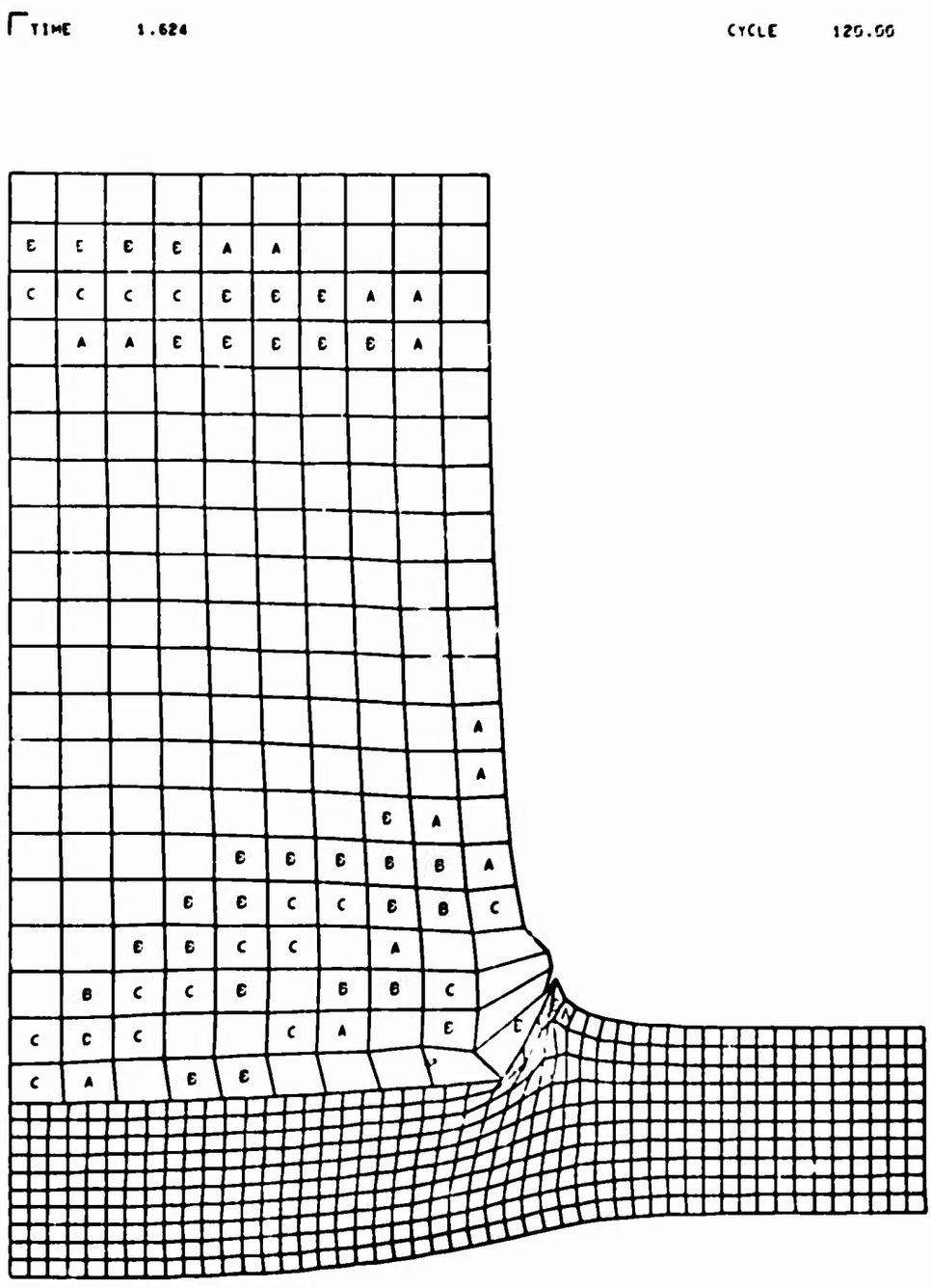

Figure III-9. Problem III, t = 1.624 μsec.

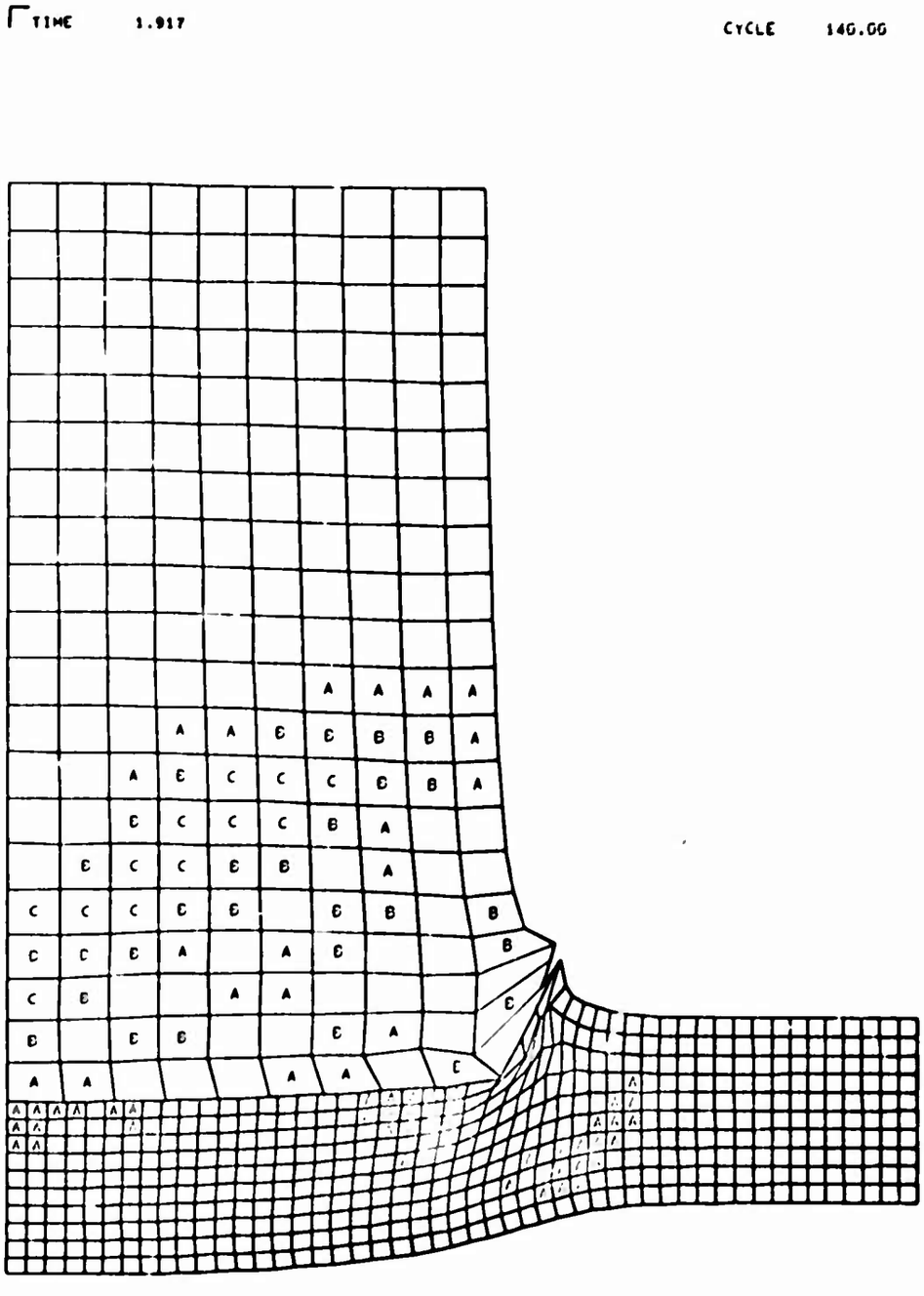

Figure III-10. Problem III, t = 1.917 μsec

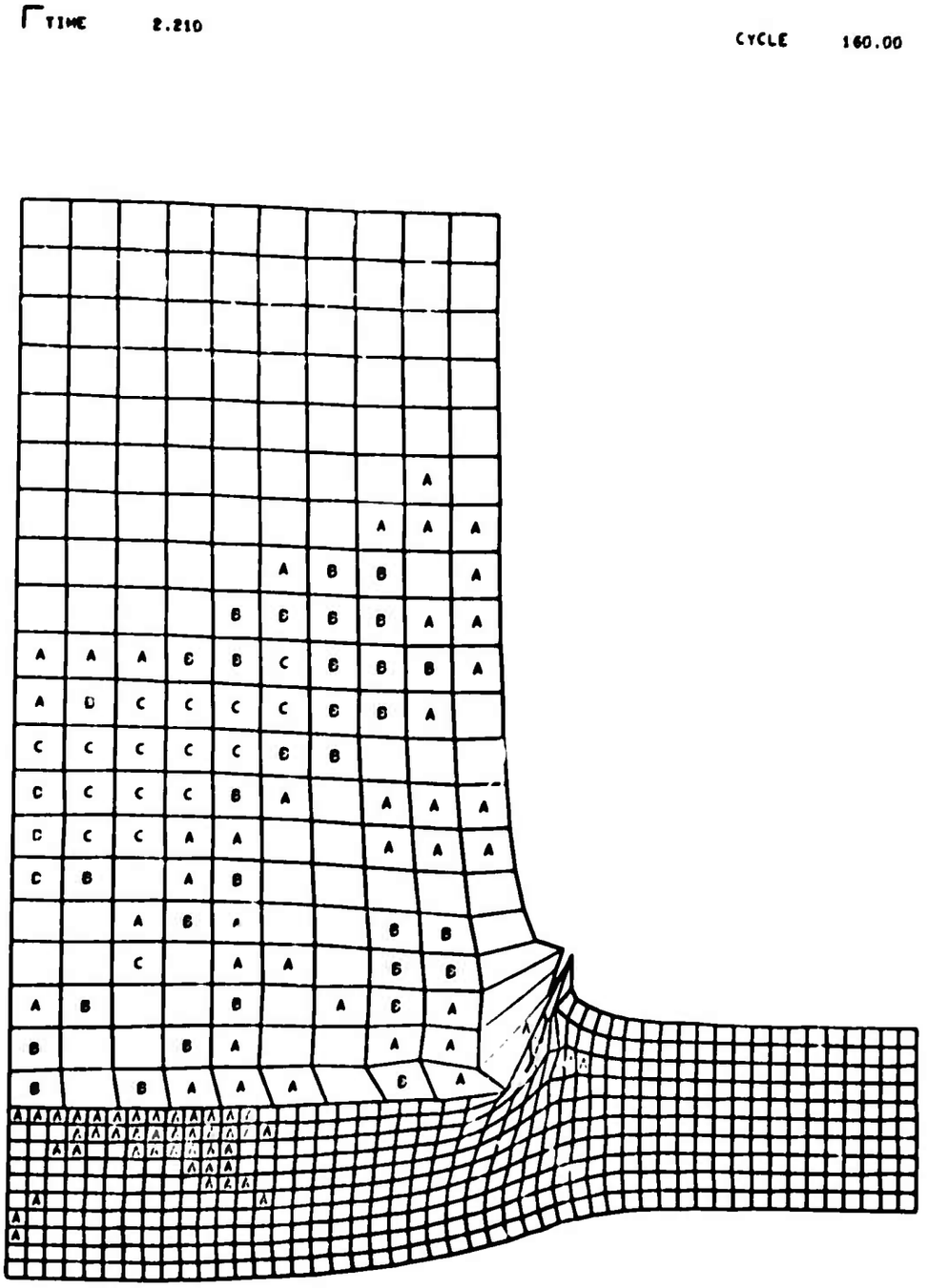

Figure III-11. Problem III, t = 2.210 μsec

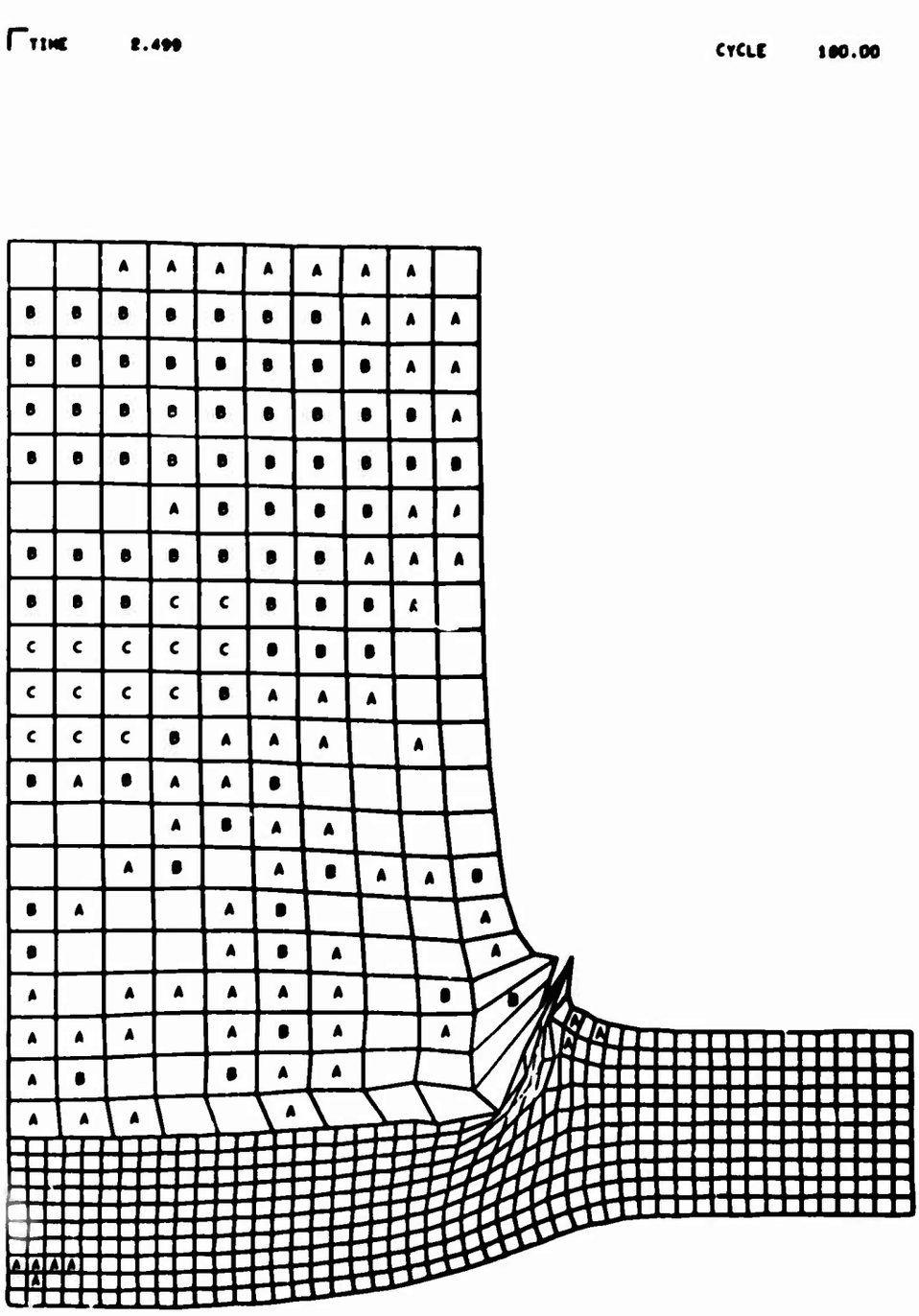

Figure III-12. Problem III, t = 2.449 μ sec

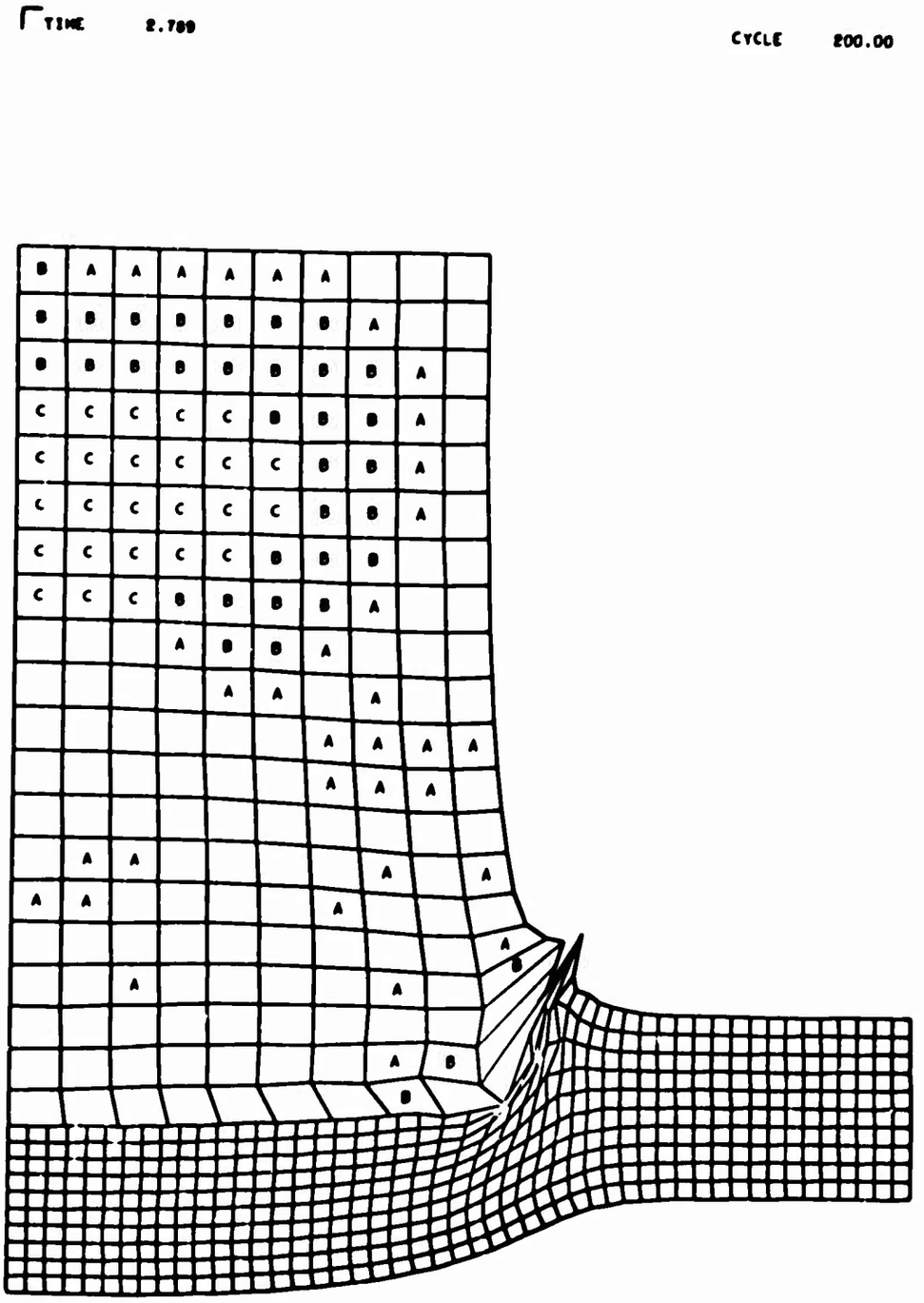

Figure III-13. Problem III, t = 2.789 μsec

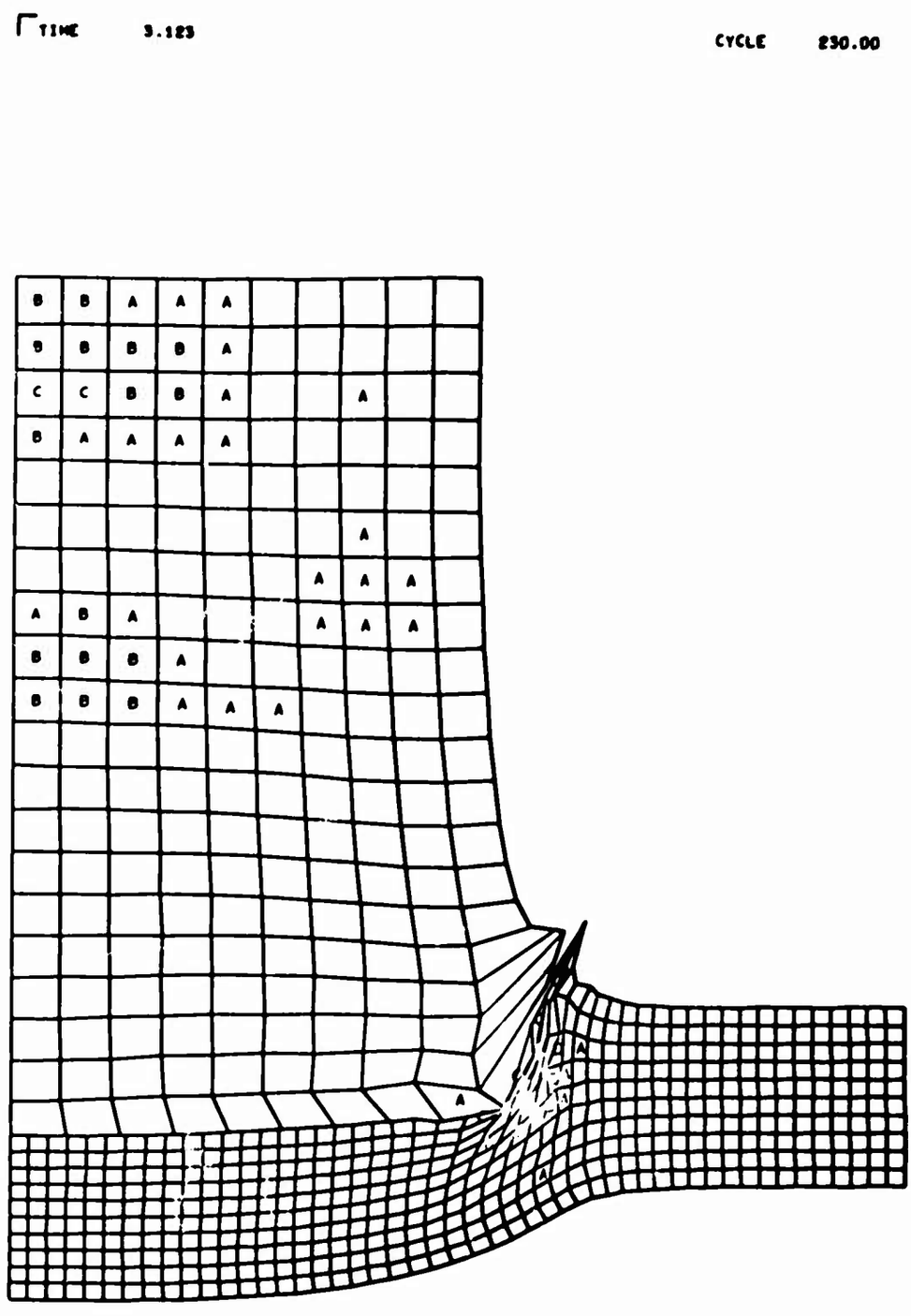

Figure III-14. Problem III, t = 3.123 μ sec.

APPENDIX IV

EXPERIMENTAL DATA FOR PROBLEM III (STEEL INTO STEEL)

TABLE IV-1. EXPERIMENTAL DATA FOR EIGHT IMPACT CASES SET UP TO DUPLICATE PROBLEM III

Shot No.	Projectile Weight (grains)		Plug Weight (grains)	Velocity (km/sec)		
				Projectile		Plug
	Before Impact	After Impact		Before Impact	After Impact	After Impact
1	53.4	53.2	10.7	.61	.507	.547
2	52.8	52.9	12.6	.61	.3655	.376
3	53.5	53.5	12.0	.636	.406	.41
4	53.1	53.0	12.0	.61	.397	.421
5	52.9	52.8	12.8	.61	.418	.434
6	53.3	53.4	11.3	.61	.392	.442
7	52.8	52.8	11.9	.61	.400	.449
8	53.5	53.5	11.85	.636	.400	.449

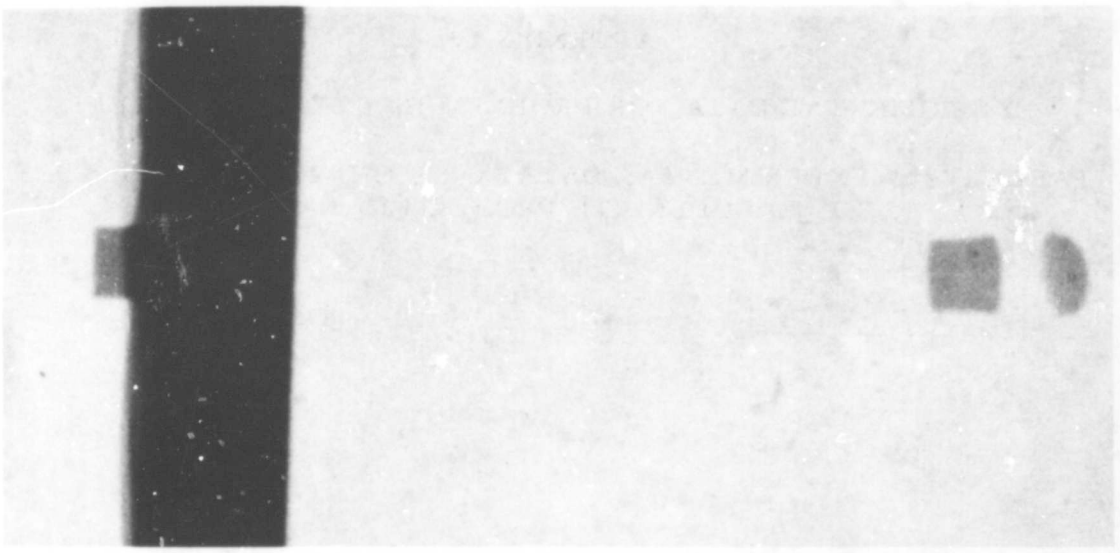

Figure IV-1. X-ray Data Showing the Experimental Pre- and Post-Impact Configurations for Problem III. Impact is from Left to Right

Figure IV-2. X-ray Data Showing the Experimental Pre- and Post-Impact Configurations for Problem III. Impact is from Left to Right and the Projectile Experienced Yaw in This Case

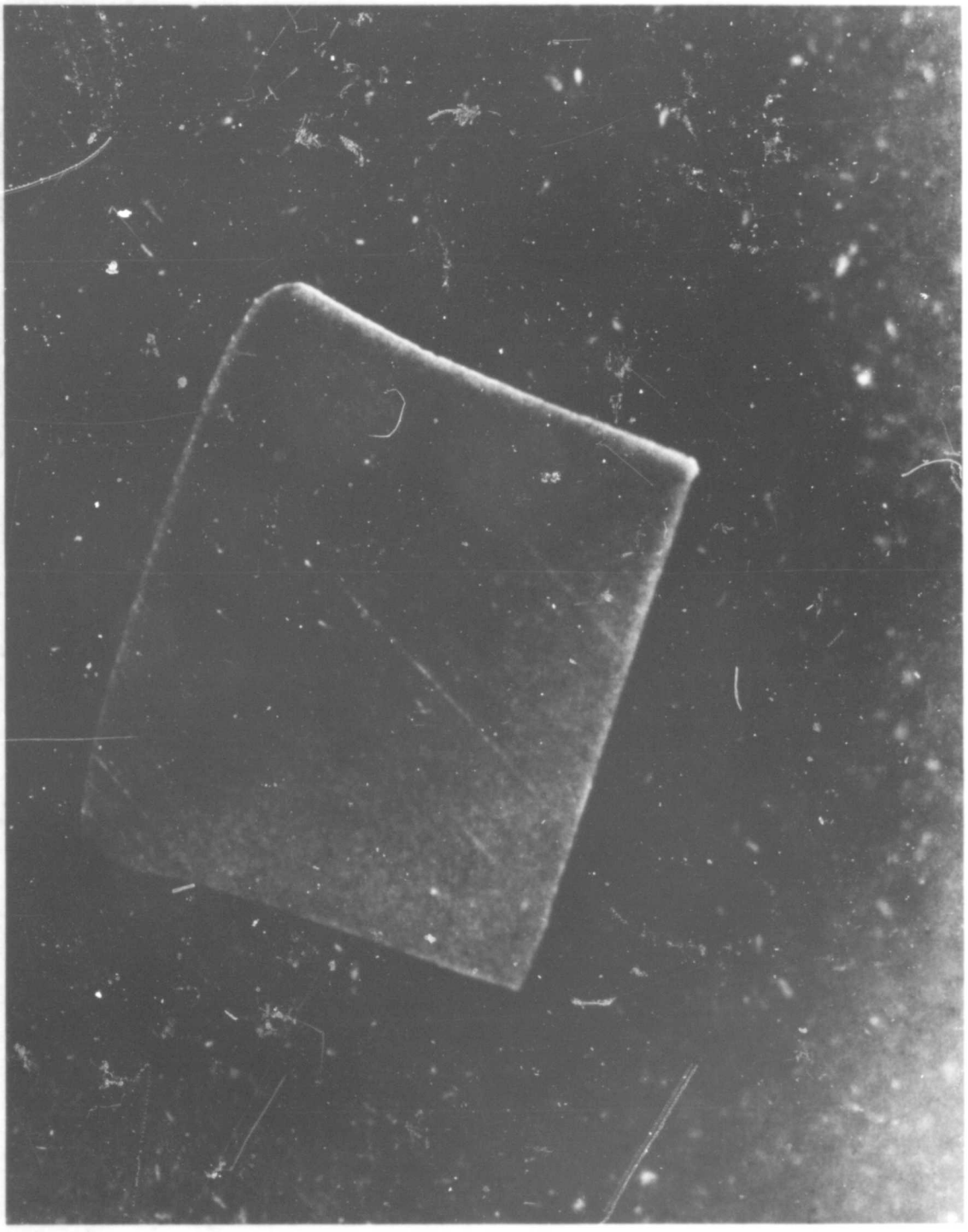

Figure IV-3. Cross Sectional View of the Deformed Projectile Shown in Figure IV-1

NOT REPRODUCIBLE

Figure IV-4. Enlargement of the Cross Sectional View of Figure IV-3 Showing the Fracture Markings in Detail

Figure IV-5. Cross Sectional View of the Deformed Projectile Shown in Figure IV-2

NOT REPRODUCIBLE

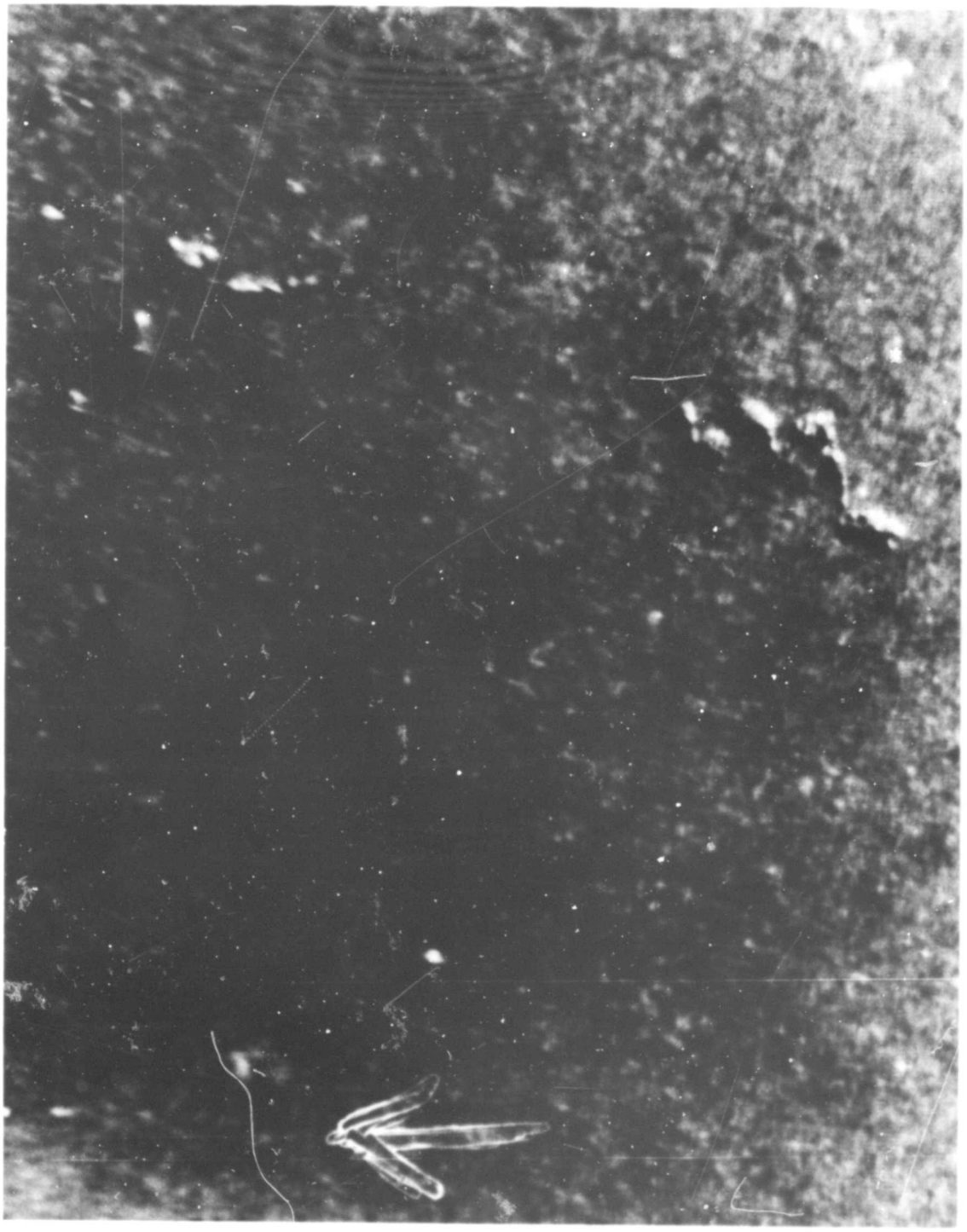

Figure IV-6. Enlargement of the Cross Sectional View of Figure IV-5 Showing the Fracture Markings in Detail

APPENDIX V

SC 4020 PLOTS OF THE LAGRANGIAN GRID FOR PROBLEM III-A

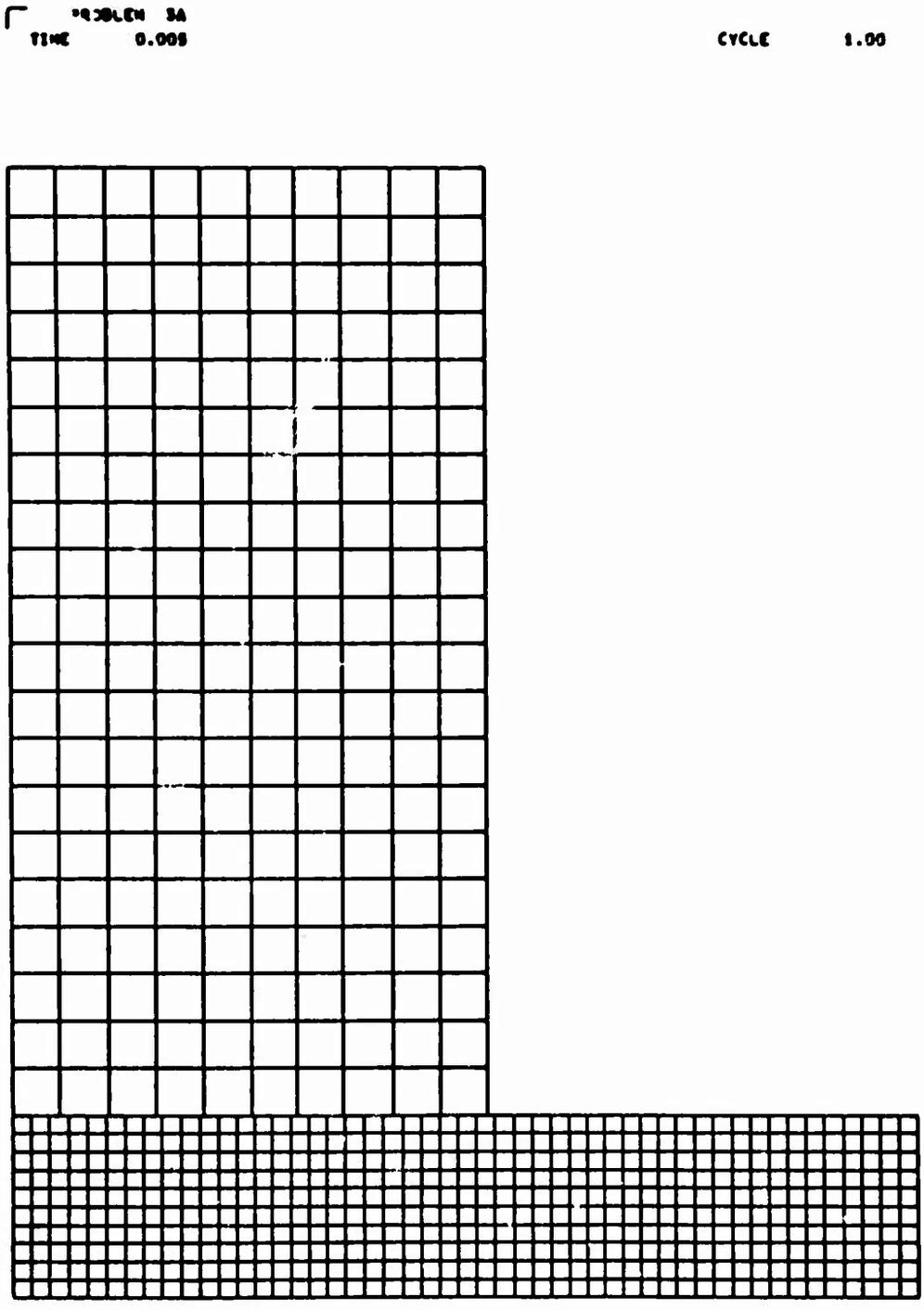

Figure V-1. Problem III-A, t = 0.005 μsec.

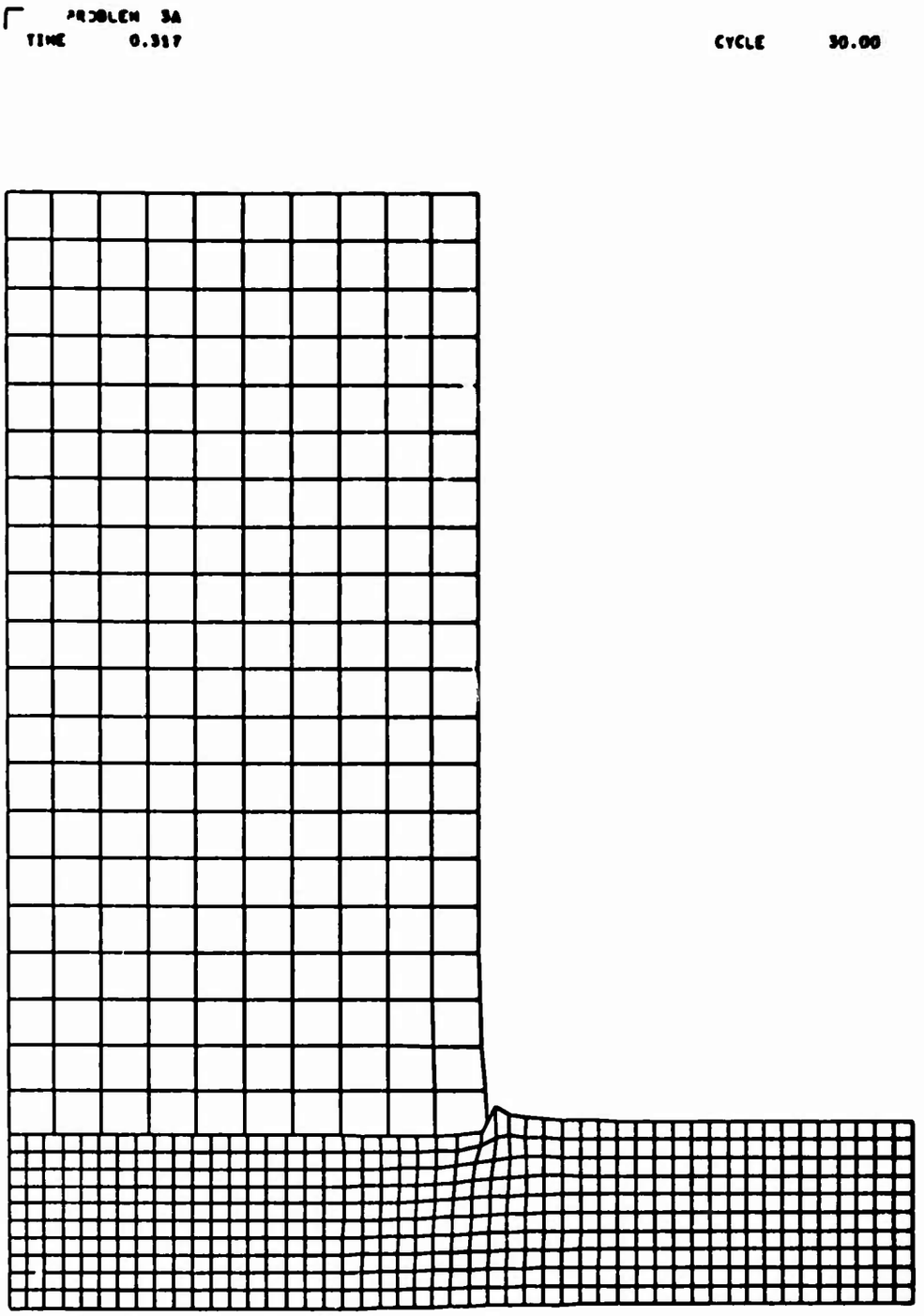

Figure V-2. Problem III-A, t = 0.317 μsec.

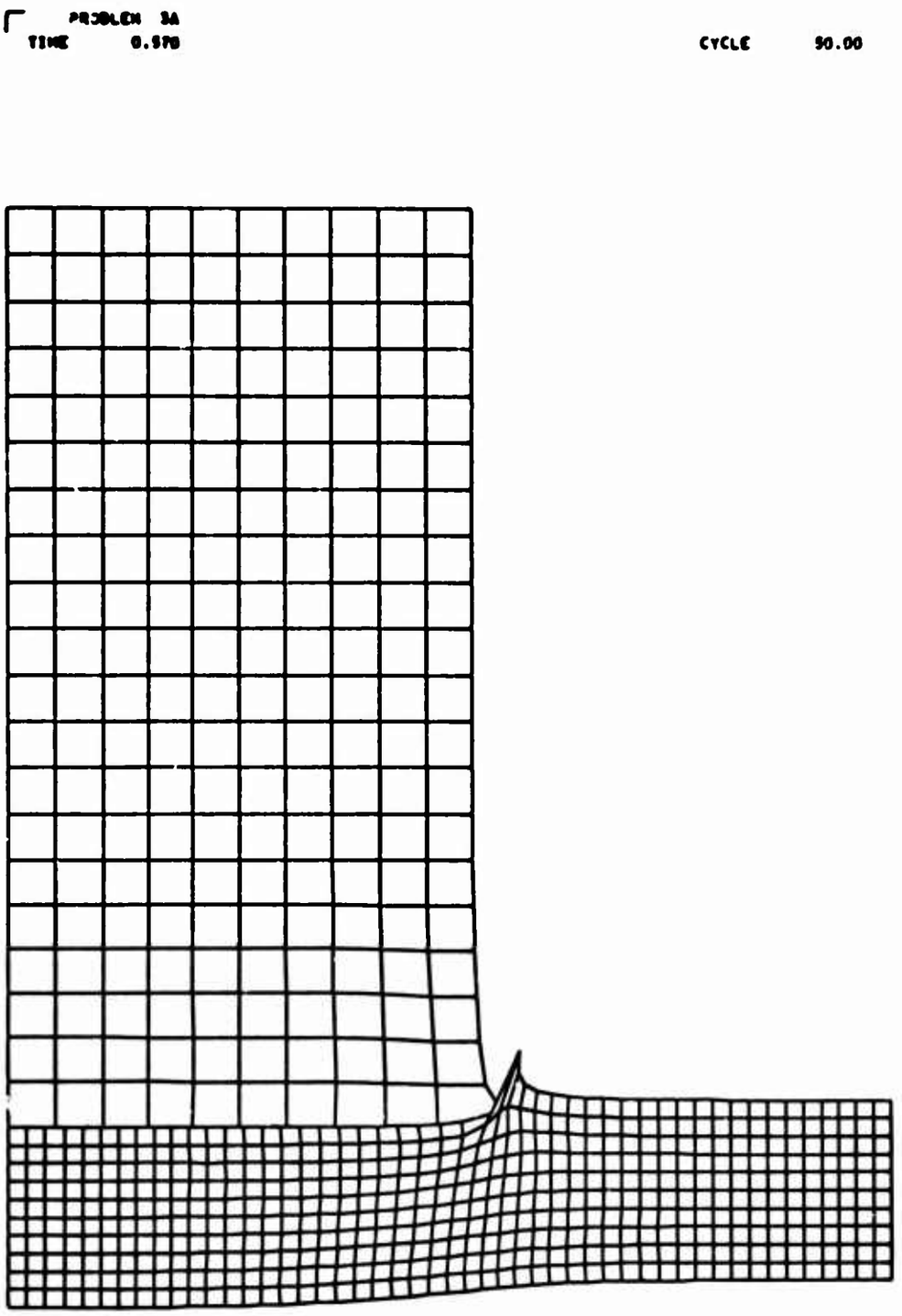

Figure V-3. Problem III-A, t = 0.570 μsec

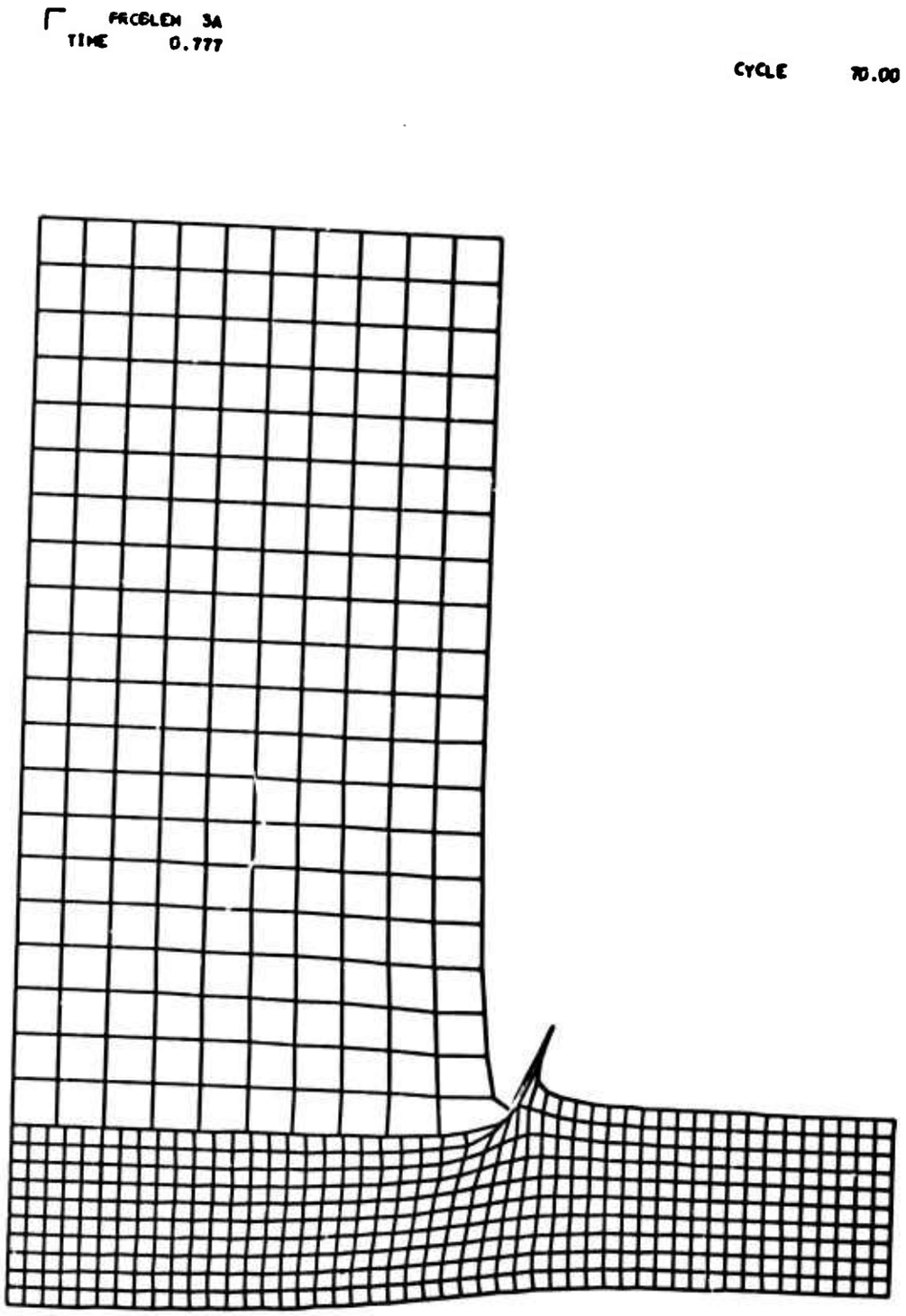

Figure V-4. Problem III-A, t = 0.777 μsec.

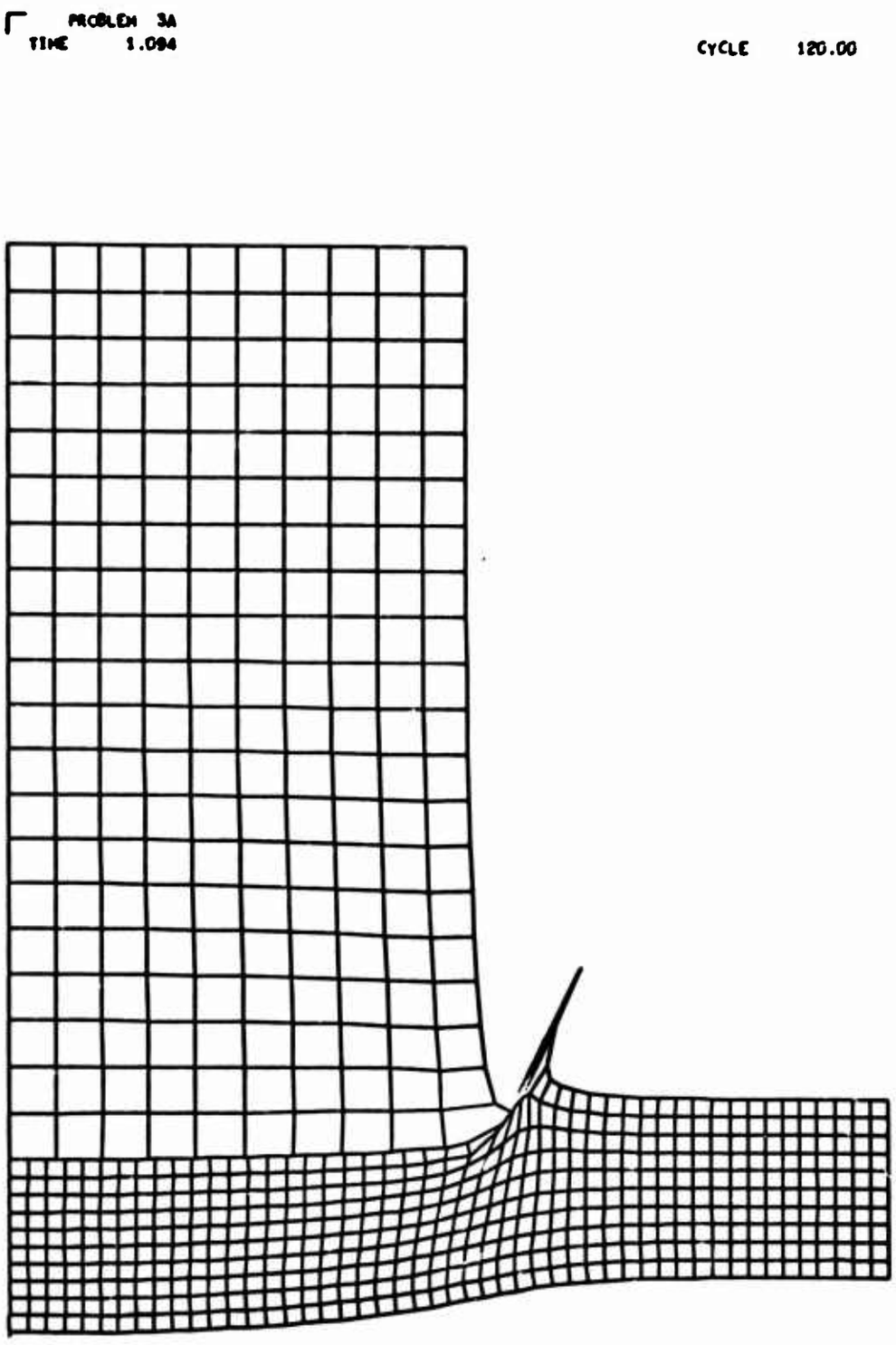

Figure V-5. Problem III-A, t = 1.094 μsec.

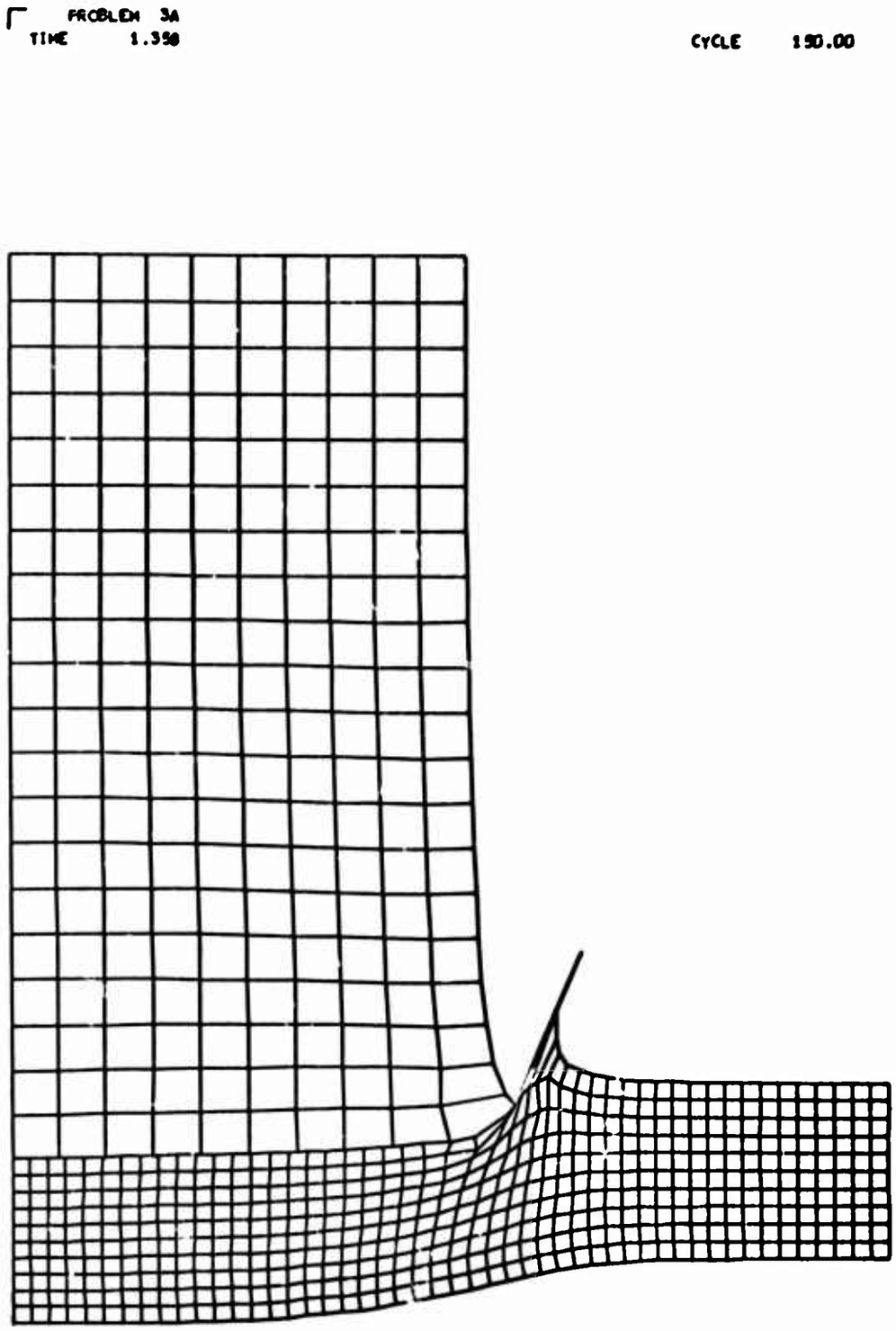

Figure V-6. Problem III-A, t = 1.358 μsec.

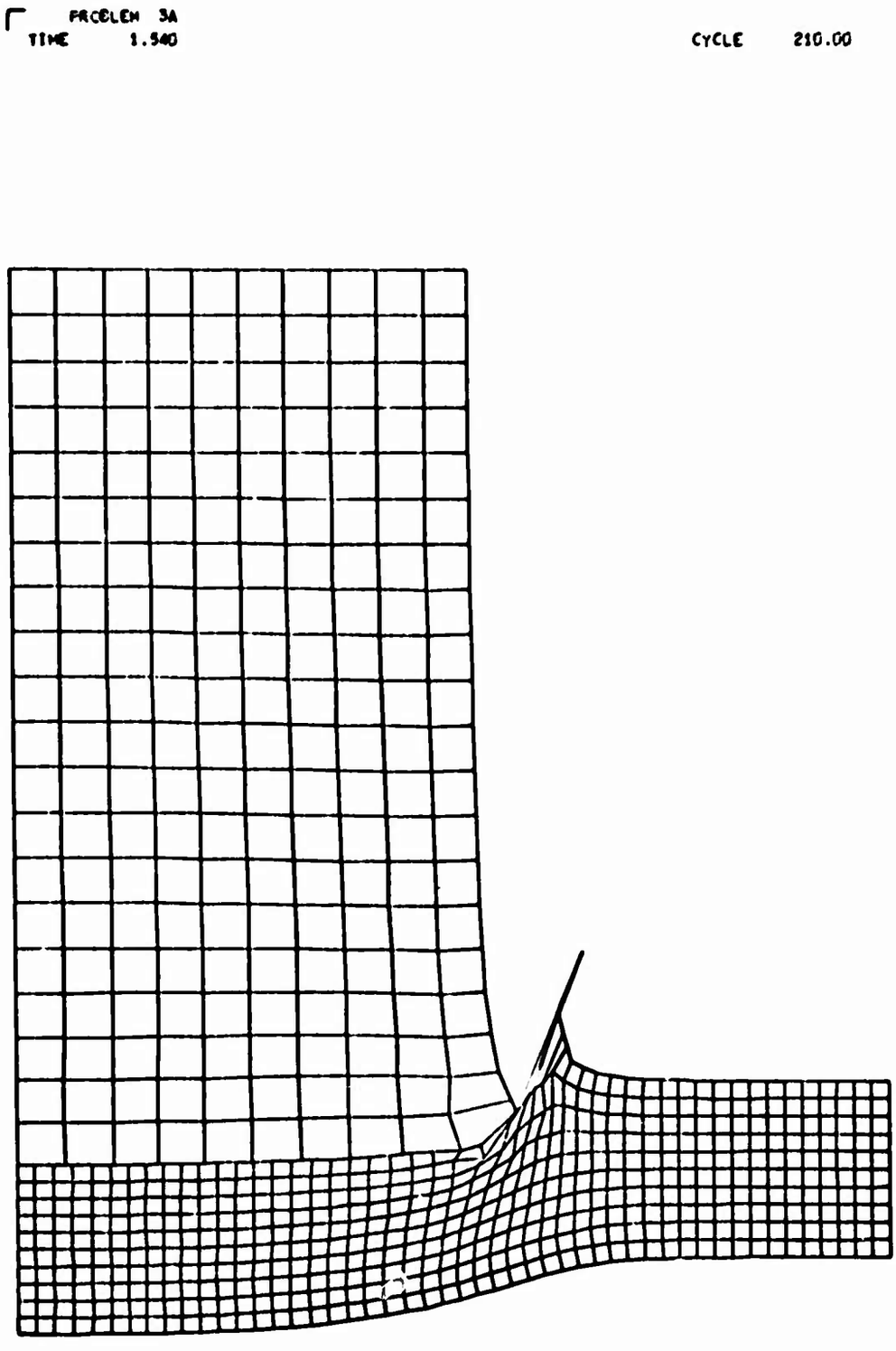

Figure V-7. Problem III-A, t = 1.540 μsec.

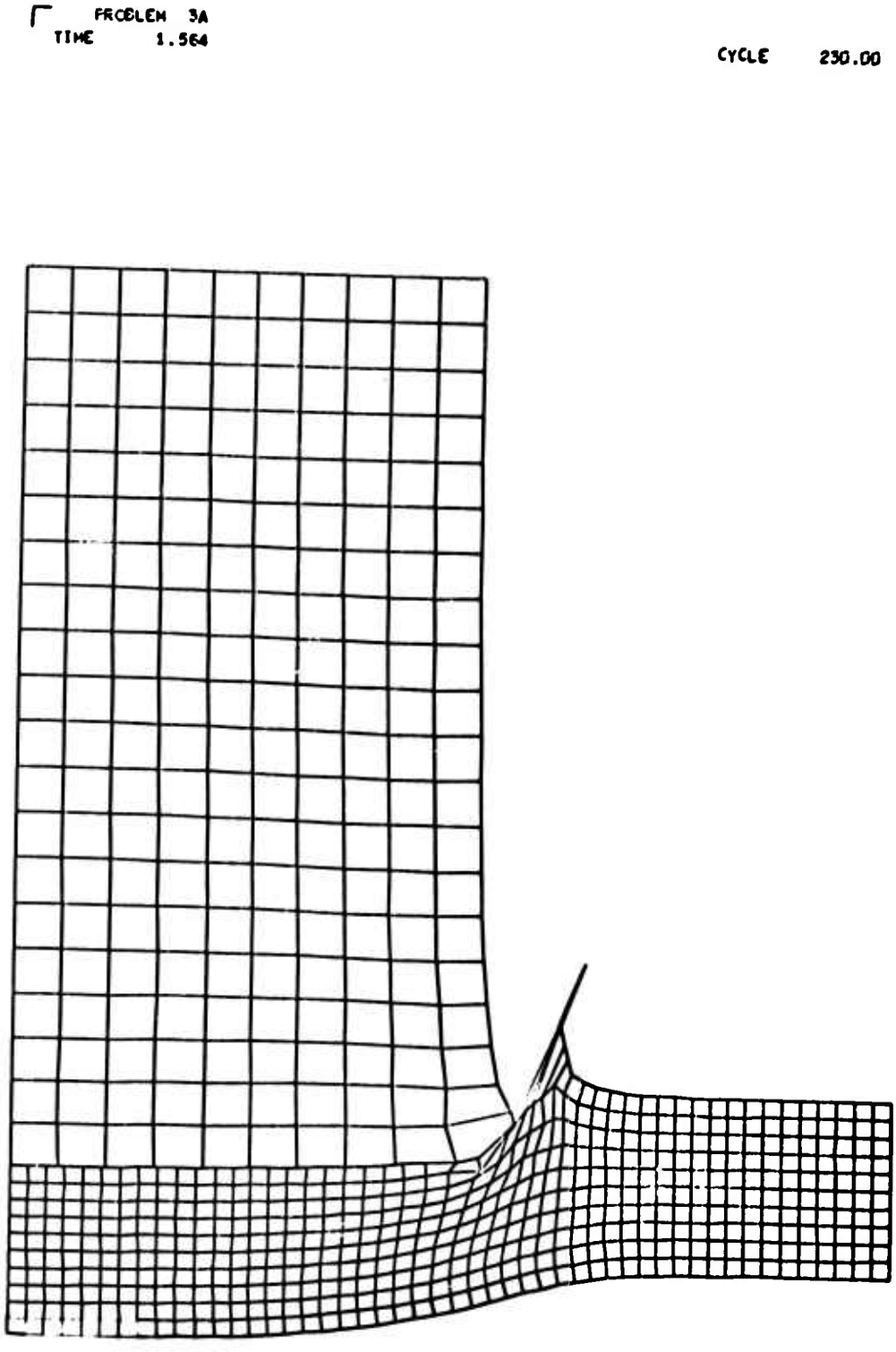

Figure V-8. Problem III-A, t = 1.564 μsec.

APPENDIX VI

EXPERIMENTAL DATA FOR

PROBLEM III-A (STEEL INTO ALUMINUM)

TABLE VI-1. DATA FROM EXPERIMENTS FOR DUPLICATION PROBLEM III-A CARRIED OUT AT D.R.I. BY R. RECHT

TEST NUMBER	69	70	72	73	74	75	76	77
Impact Velocity (km/sec)	0.568	0.642	0.645	0.565	0.652	0.620	0.587	0.600
Residual Velocity of Plate Plug (km/sec)	0.564	0.640	0.667	0.573	0.668	0.635	0.597	0.587
Residual Velocity of Cylinder (km/sec)	0.489	0.555	0.560	0.480	0.556	0.533	0.490	0.509
Angle Between Axis of Cylinder and Line of Fire Just Prior to Impact (Degrees)	0.5	7	2	5.7	0.5	1	1	2.5

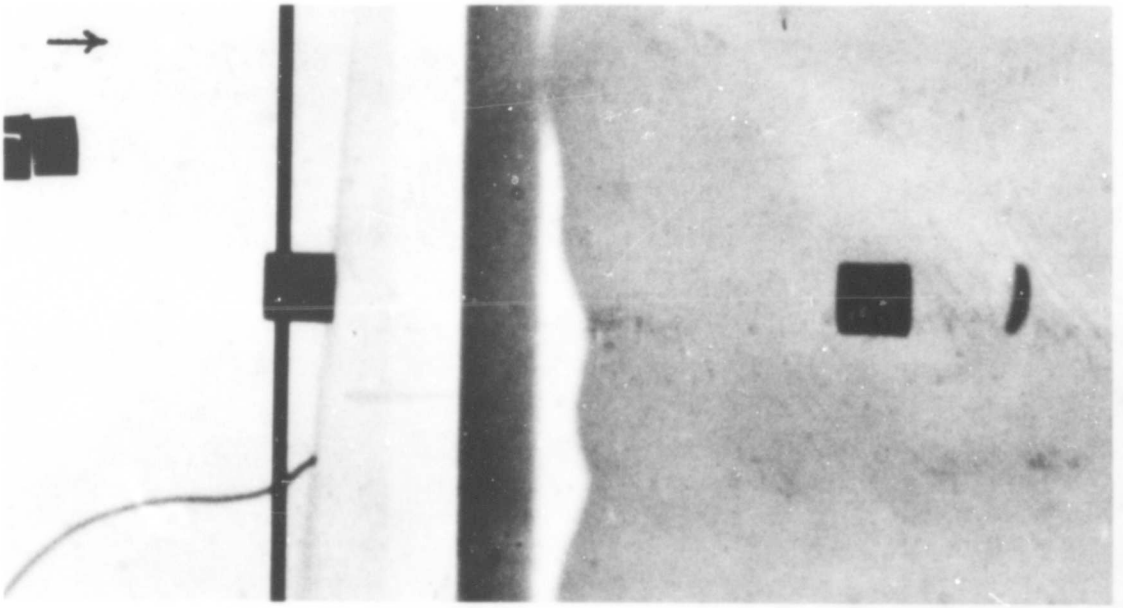

Figure VI-1. Plan View Flash Radiograph for Test No. 75

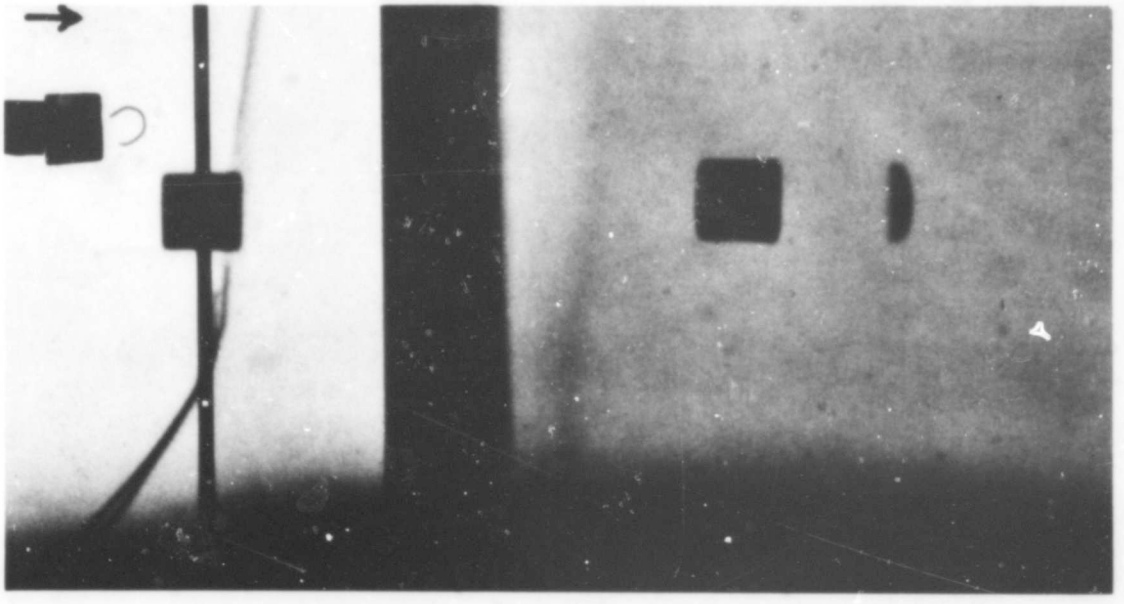

Figure VI-2. Elevation View Flash Radiograph for Test No. 75

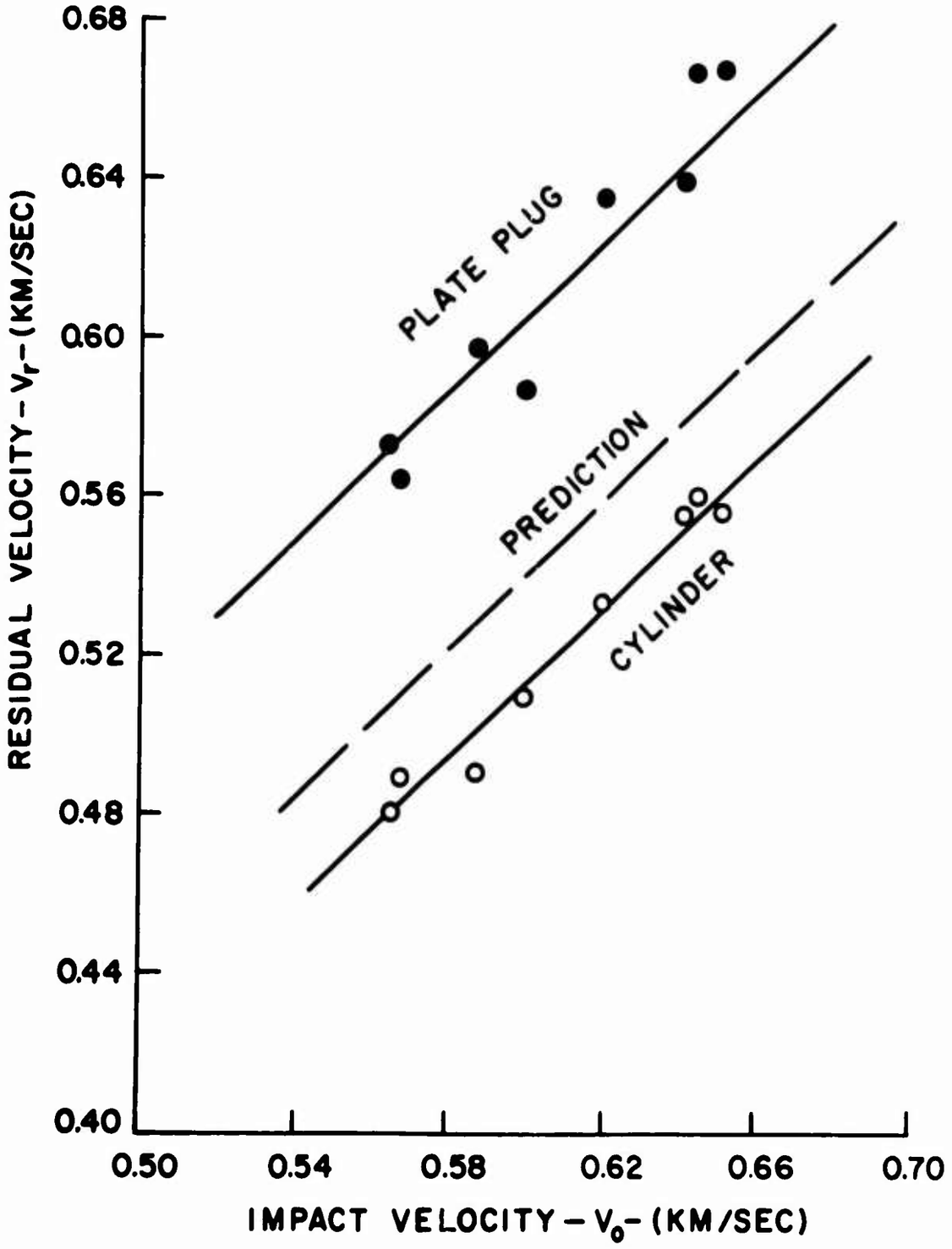

Figure VI-3. Plot of Residual Velocity Versus Impact Velocity for the Set of Experiments Performed at DRI for Duplicating Problem III-A. The Dashed Line is the Prediction from the DRI Equation

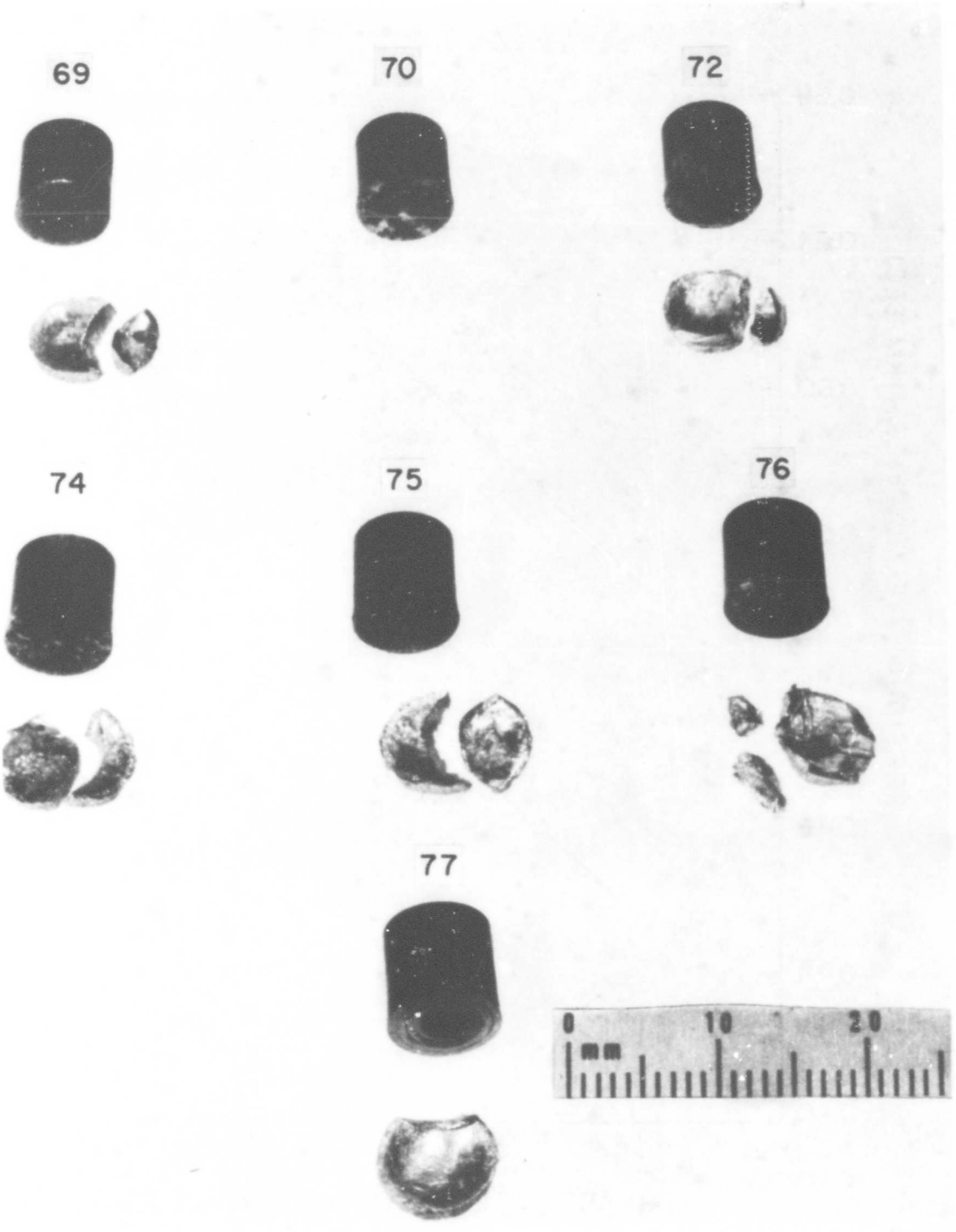

Figure VI-4. Impacted Projectiles and Plate Plugs

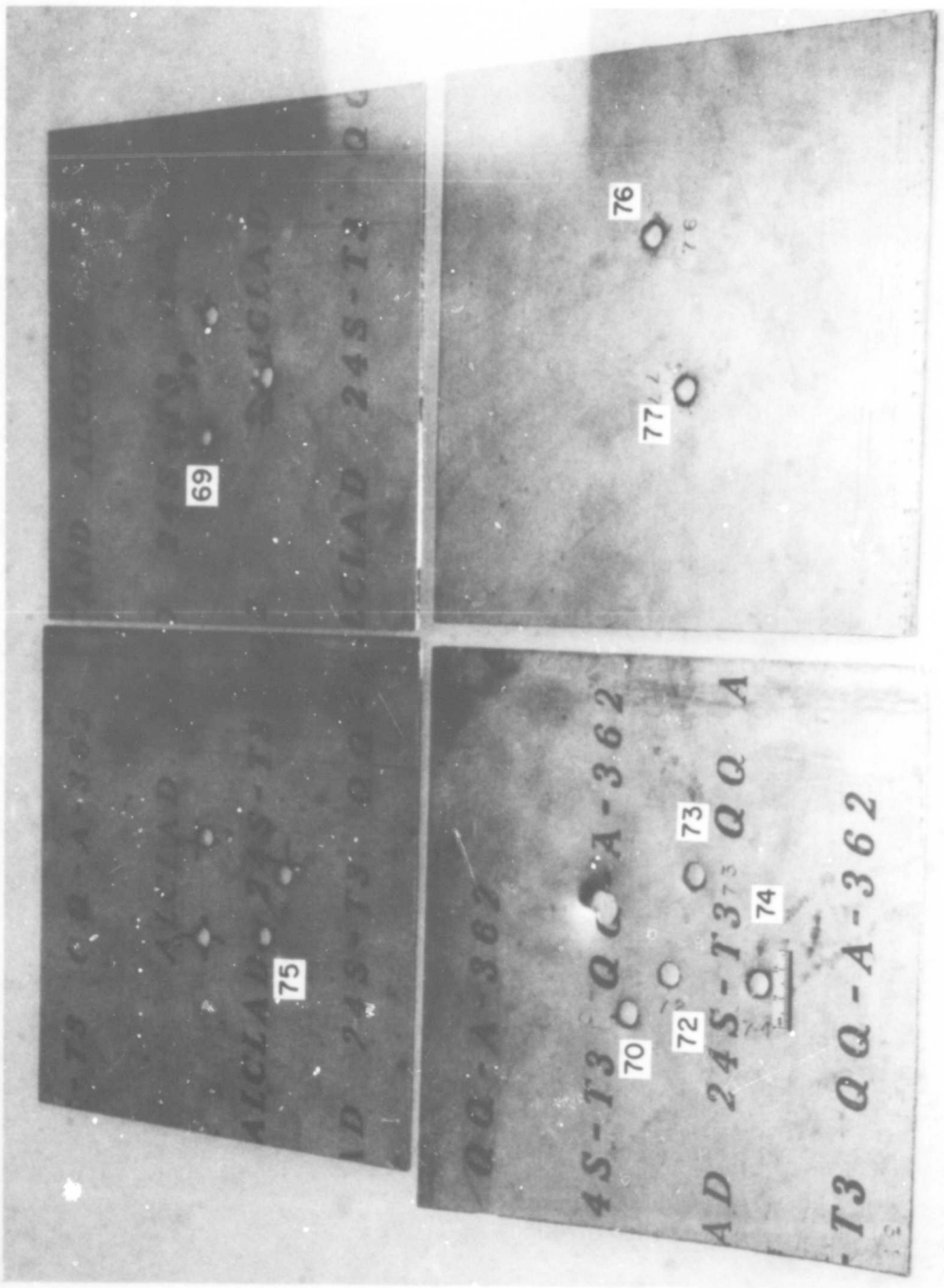

Figure VI-5. Impacted Side of Aluminum Plates Used

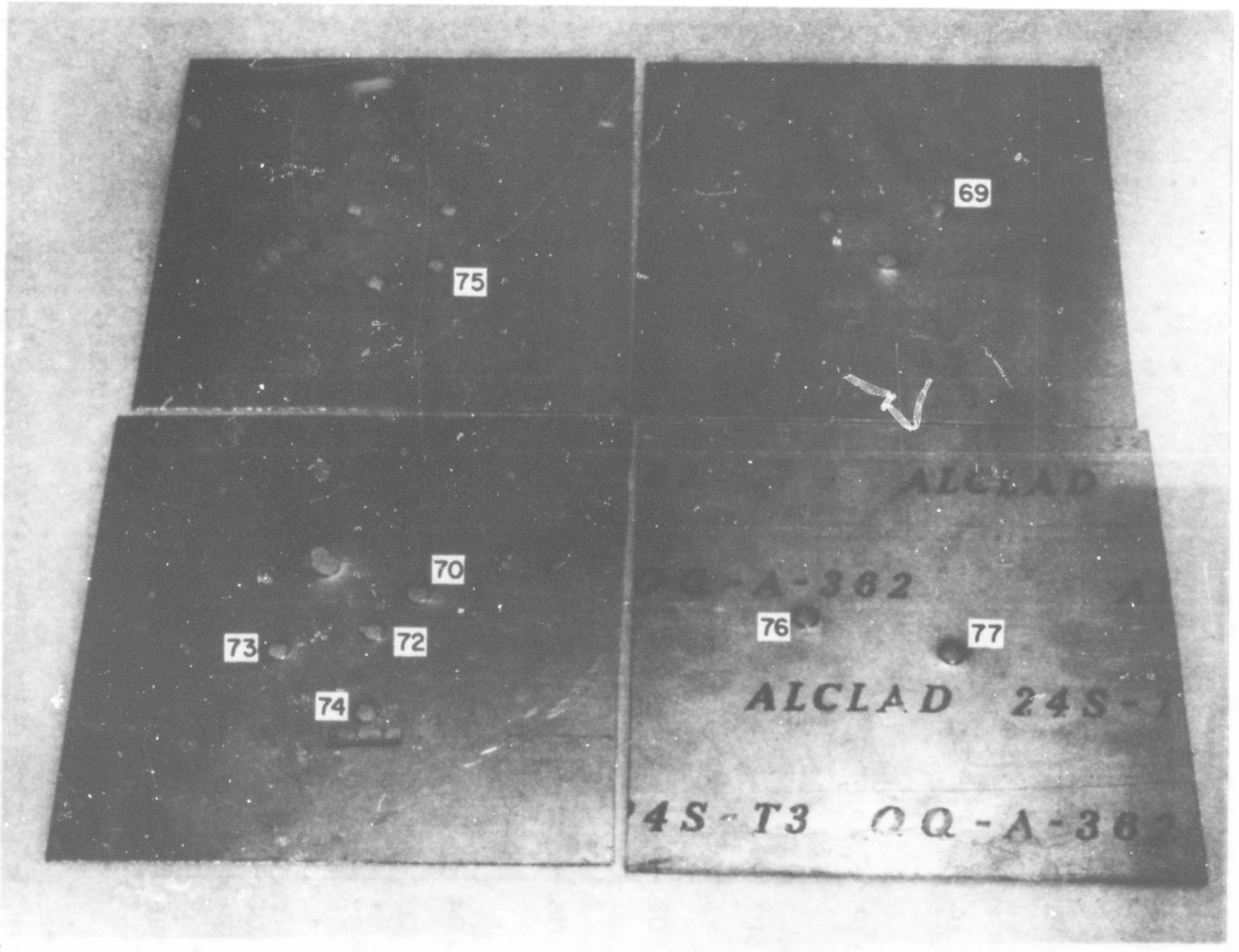

Figure VI-6. Rear Free Surface of Aluminum Plates After Impact

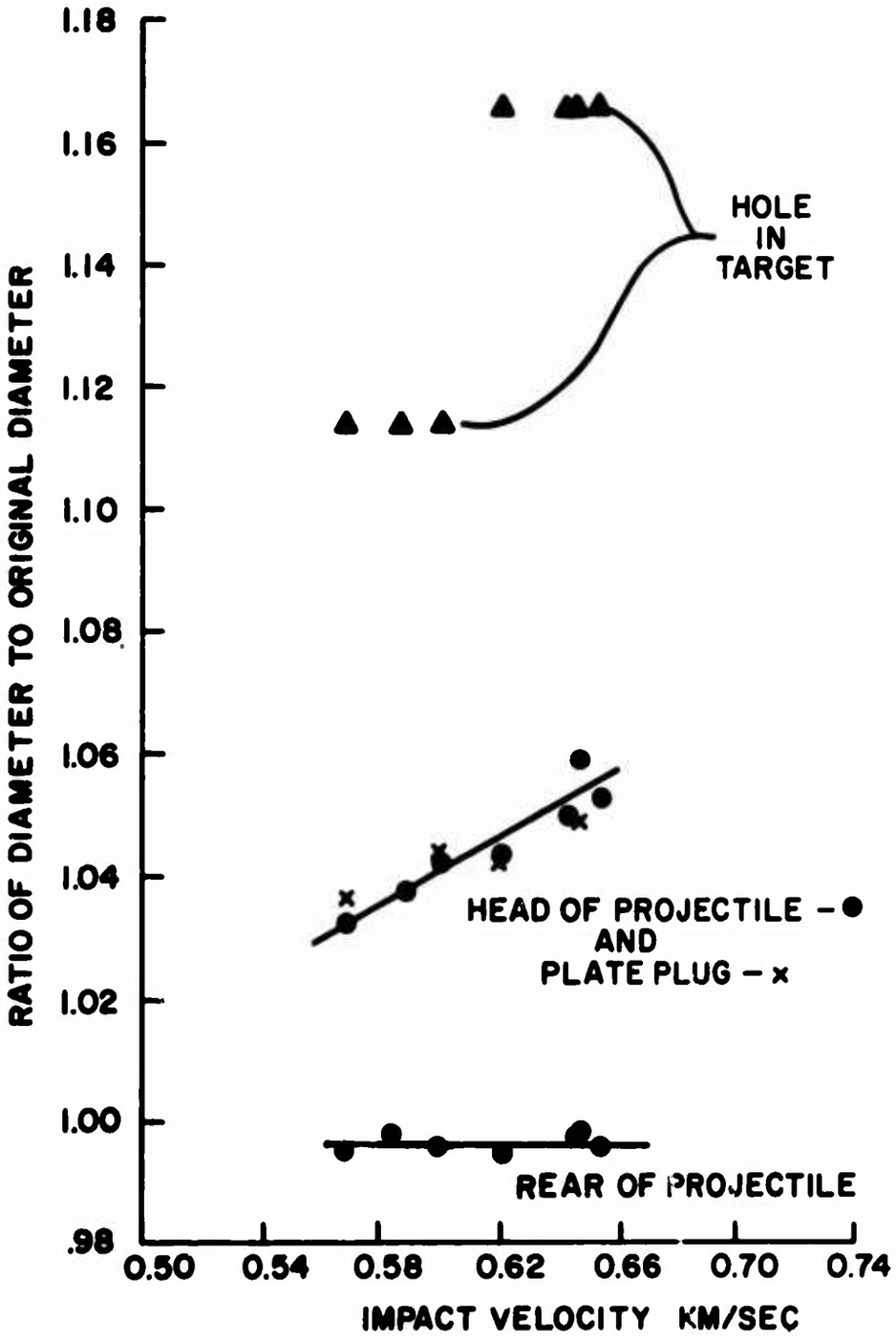

Figure VI-7. Plots of the Ratio of Target Hole, Plate Plug, Head and Rear of Projectile Diameters to the Original Projectile Diameter Versus Impact Velocity

REFERENCES

1. Sedgwick, R. T. and Woodall, S. R.; "Theoretical Terminal Ballistic Investigation and Studies of Impact at Low and Very High Velocities" Interim Report, Contract No. F-08635-67-C-0079, 1 March 1967 - 31 August 1967.
2. Recht, R. F. and Ipson, T. W.; "The Dynamics of Terminal Ballistics", Final Report, Contract No. DA-23-072-ORD-1302, 1 February 1962.
3. Abbott, K. H.; "Metallurgical Observations of High Speed Impact", Watertown Arsenal Report.
4. Curtis, C. W.; "Perforation Limits for Nondeforming Projectiles", Frankford Arsenal Report No. R-903, February 1951.
5. Fugelso, L. E. and Bloedow, F. H.; "Studies in the Perforation of Thin Metallic Plates by Projectile Impact: I. Normal Impact of Circular Cylinders", Contract No. DA 19-129-AMC-247(N), June 1966.
6. Goldsmith, W.; Impact, Edward Arnold Ltd., London, 1960.
7. Cristescu, N.; Plasticity, in "Proceedings of the Second Symposium on Naval Structural Mechanics" Ed. by E. H. Lee and P. S. Symonds, Pergamon Press, New York, 1960.
8. Bakhsigan, F. A.; "Visco-Plastic Flow in a Plate Produced by a Shock with a Cylinder", Prikl Mat. Mekh., 12, No. 1, 1948 (in Russian). English Translation by E. Rosicky, BRL, Aberdeen Proving Ground, March 1964.
9. Pytel, A. and Davids, N.; "A Viscous Model for Plug Formation in Plates", J. Franklin Inst., Vol. 276, No. 5, November 1963.
10. Kochetkov, A. M.; "On the Propagation of Elastic-visco-plastic Shear Waves in Plates", Prikl Mat. Mekh. Vol. 14, No. 2, 1950. (in Russian) (cited by Cristescu [7]).

11. Chou, P. C.; "Perforation of Plates by High-Speed Projectiles", Developments in Mechanics, Vol. 1 (Proc. of the Seventh Midwestern Mechanics Conference), Ed. by J. E. Lay and L. E. Malvern, Plenum Press, New York, 1961.

12. Minnich, H. R. and Davids, N.; "Plug Formation in Plates", Interim Tech. Report No. 3, Contract No. DA-31-124-ARO(D)-67, September 1, 1964.

13. Kukudjanov, V. N.; "The Propagation of Cylindrical Stress Shock Waves in a Plate Beyond the Yield Point", Trudi MFTI, Vol. 3, pp 108-120 (in Russian) (cited by Cristescu [7]).

14. Taylor, G. I.; "The Formation and Enlargement of a Circular Hole in a Thin Plastic Sheet", Quart. J. Mech. Appl. Math., Vol. 1, pp 103-124 (1948).

15. Bethe, H. A.; "Attempt of a Theory of Armor Penetration", Frankford Arsenal Report, 1941.

16. Thomson, W. T.; "An Approximate Theory of Armor Penetration", J. Appl. Phys. Vol. 26 pp 80-82, 1955.

17. Zener, C. and Peterson, R. E.; "Mechanics of Armor Penetration", Watertown Arsenal Laboratory, Second Partial Report, No. 710/492, May 1943.

18. Masket, A. V.; "The Measurement of Forces Resisting Armor Penetration", J. Appl. Phys., Vol. 20, 1949.

19. Bluhm, J. I.; "Stresses on Projectiles During Penetration", Proc. Soc. Exp. Stress Anal., Vol. 13, No. 3, 1952.

20. Recht, R. F. and Ipson, T. W.; "Ballistic Perforation Dynamics", J. Appl. Mech. Vol. 30, pp 384-390, 1963.

21. Zaid, M. and Paul, B.; "Mechanics of High Speed Projectile Perforation", J. Franklin Inst., pp 117-126, 1957.

22. Riney, T. D.; "Theoretical Hypervelocity Impact Calculations Using the PICWICK Code", General Electric TIS No. R64SD13, 1964.

23. Halda, E.J. and Riney, T. D.; "VISTA - A Two-Dimensional Particle-in-Cell Code for Three Materials", Document No. 66SD409, Advanced Re-Entry Technology Programs, Missile and Space Division, General Electric Company, Philadelphia, Pennsylvania.

24. Balmer, H. A.; "Improved Computer Programs - DEPROSS 1, 2, and 3 - To Calculate the Dynamic Elastic-Plastic Two-Dimensional Responses of Impulsively-Loaded Beams, Rings, Plates, and Shells of Revolution", ASRL TR 128-3, Aeroelastic and Structures Research Laboratory, Department of Aeronautics and Astronautics, Massachusetts Institute of Technology, August 1965.

25. Balmer, H. A. and Witmer, E. A.; "Theoretical-Experimental Correlation of Large Dynamic and Permanent Deformations of Impulsively-Loaded Simple Structures", FDL-TDR-64-108, Air Force Flight Dynamics Laboratory, Wright-Patterson Air Force Base, Ohio, July 1964.

26. Wilkins, J. L. and Giroux, R.; "Calculations of Elastic-Plastic Flow," UCRL-7322, April 1963.

27. Heyda, J. F. and Riney, T. D.; "Peak Axial Pressures in Semi-infinite Media under Hypervelocity Impact", GE TIS R64SD87, November 1964.

28. Recht, R.; "Experimental Definition of the Perforation of a Thin Aluminum Sheet by a Cylinder", AFAL Report, March 1968.

(The reverse of this page is blank)

UNCLASSIFIED

Security Classification

DOCUMENT CONTROL DATA - R & D

(Security classification of title, body of abstract and indexing annotation must be entered when the overall report is classified)

1 ORIGINATING ACTIVITY (Corporate author) Space Sciences Laboratory General Electric Company King of Prussia, Pennsylvania	2a. REPORT SECURITY CLASSIFICATION Unclassified 2b. GROUP

3 REPORT TITLE

THEORETICAL TERMINAL BALLISTIC INVESTIGATION AND STUDIES OF IMPACT AT LOW AND VERY HIGH VELOCITIES

4 DESCRIPTIVE NOTES (Type of report and inclusive dates)

Interim - 1 March 1967 to 29 February 1968

5 AUTHOR(S) (First name, middle initial, last name)

R. J. Sedgwick

6 REPORT DATE	7a. TOTAL NO OF PAGES	7b. NO OF REFS
May 1968	153	29

8a. CONTRACT OR GRANT NO	9a. ORIGINATOR'S REPORT NUMBER(S)
F08635-67-C-0079 b. PROJECT NO 5841 c. d.	9b. OTHER REPORT NO(S) (Any other numbers that may be assigned this report) AFATL-TR-68-61

10 DISTRIBUTION STATEMENT

This document is subject to special export controls and each transmittal to foreign governments or foreign nationals may be made only with prior approval of the Air Fore Armament Laboratory (ATBT), Eglin AFB, Florida 32542.

11 SUPPLEMENTARY NOTES	12 SPONSORING MILITARY ACTIVITY
Available in DDC	Air Force Armament Laboratory Air Force Systems Command Eglin Air Force Base, Florida

13 ABSTRACT The important parameters and failure modes pertinent to ballistic impact are discussed in detail and a review of available theoretical penetration formulas is presented. A method for a complete solution to the ballistic impact problem is outlined including the material model, numerical techniques, application of failure criteria and description of both post-failure material behavior as well as the residual state. Parametric studies based on this outline should reveal the necessary insight for developing predicitive relationships between the pre-impact and post-impact parameters.

A complete solution is presented for the case of a steel cylinder impacting normally into a thin plate of like material. It is shown that predictions of stress wave propagation and reflections in the early stages of impact are in good agreement with one-dimensional theory. The shear stress, generalized plastic strain and plastic work distributions as well as the material flow pattern indicate that failure will be due to plugging, hence the employment of a maximum shear theory of failure. The final shape of both the projectile and the plate plug are given and the velocity of the plate material beneath the projectile at the predicted time of failure is in good agreement with the value of 0.382 km/sec predicted by the theory of Recht and Ipson. This gives a residual kinetic energy for the projectile plate-plug configuration of 3.1×10^9 ergs or 47.4% of the total initial energy. It is believed that much of the remaining energy is retained in the projectile and plate-plug as internal energy. It is predicted that both the projectile and plate-plug will remain intact but a region of contained failure in the projectile near the impacted surface is defined.

DD FORM 1 NOV 65 1473

UNCLASSIFIED

Security Classification

14 KEY WORDS	LINK A		LINK B		LINK C	
	ROLE	WT	ROLE	WT	ROLE	WT
Ballistic Impact						
Pre-impact Parameters						
Post-impact Parameters						
Stress Wave Propagation						
Maximum Shear Theory of Failure						